

SEARCH FOR A SCALAR PARTNER OF THE TOP QUARK IN THE  
JETS+ $E_T^{\text{miss}}$  FINAL STATE IN PROTON-PROTON COLLISIONS AT  $\sqrt{S} = 13$   
TEV WITH THE ATLAS DETECTOR

by

IAN SNYDER

A DISSERTATION

Presented to the Department of Physics  
and the Graduate School of the University of Oregon  
in partial fulfillment of the requirements  
for the degree of  
Doctor of Philosophy

June 2018

## DISSERTATION APPROVAL PAGE

Student: Ian Snyder

Title: Search for a Scalar Partner of the Top Quark in the Jets+ $E_T^{\text{miss}}$  Final State in Proton-Proton Collisions at  $\sqrt{s} = 13$  TeV with the ATLAS Detector

This dissertation has been accepted and approved in partial fulfillment of the requirements for the Doctor of Philosophy degree in the Department of Physics by:

James Brau	Chair
Stephanie Majewski	Advisor
Spencer Chang	Core Member
Boyana Norris	Institutional Representative

and

Sara D. Hodges	Interim Vice Provost and Dean of the Graduate School
----------------	--

Original approval signatures are on file with the University of Oregon Graduate School.

Degree awarded June 2018

© 2018 Ian Snyder

This work is licensed under a Creative Commons  
**Attribution-NonCommercial-NoDerivs (United States) License.**

## DISSERTATION ABSTRACT

Ian Snyder

Doctor of Philosophy

Department of Physics

June 2018

Title: Search for a Scalar Partner of the Top Quark in the Jets+ $E_T^{\text{miss}}$  Final State in Proton-Proton Collisions at  $\sqrt{s} = 13$  TeV with the ATLAS Detector

This dissertation presents a search for pair production of a scalar partner to the top quark in proton-proton collisions at the ATLAS detector at the Large Hadron Collider (LHC). The LHC is a particle accelerator located in Geneva, Switzerland that collides two beams of protons. ATLAS is a general purpose detector and is one of four detectors at the LHC. The data used in this analysis was recorded during Run 2 with a total of  $36.1 \text{ fb}^{-1}$  at a center-of-mass energy of  $\sqrt{s} = 13$  TeV. In supersymmetry, the scalar partner to the top quark is the stop, which decays to a top quark and neutralino or to a bottom quark and chargino. The experimental signature considered is four or more jets plus missing transverse momentum. The data yielded no significant excess over the Standard Model background expectation, and exclusion limits are reported in terms of the stop and neutralino masses. Assuming a branching fraction of 100% to a top quark and neutralino, stop masses in the range 450-1000 GeV are excluded for neutralino masses below 160 GeV. In the case where the stop mass is close to the top mass plus the neutralino mass, masses between 235-590 GeV are excluded. The results are also interpreted in terms of the phenomenological Minimal Supersymmetric

Standard Model.

Additionally, work on an upgrade to the ATLAS trigger system, the Global Feature Extractor (gFEX), is presented. This upgrade will have the unique ability to scan over the entire calorimeter to trigger on global variables and large radius jets. A scheme was developed to calibrate the gFEX that also reduces pileup noise.

This dissertation includes previously published coauthored material.

## CURRICULUM VITAE

NAME OF AUTHOR: Ian Snyder

### GRADUATE AND UNDERGRADUATE SCHOOLS ATTENDED:

University of Oregon, Eugene, Oregon  
Vanderbilt University, Nashville, Tennessee

### DEGREES AWARDED:

Doctor of Philosophy, Physics, 2018, University of Oregon  
Bachelor of Engineering, Chemical Engineering and Mathematics, 2006,  
Vanderbilt University

### PROFESSIONAL EXPERIENCE:

Graduate Research Assistant, University Of Oregon: ATLAS Collaboration,  
2014-Present

Graduate Teaching Assistant, University Of Oregon: Department of Physics,  
2012-2014

Associate Engineer, Frontage Laboratories, Inc. 2009-2012

### GRANTS, AWARDS AND HONORS:

U.S. Department of Energy (DOE) Office of Science Graduate Student Research  
(SCGSR) Award, 2016

Cum Laude in Chemical Engineering, 2006

PUBLICATIONS:

List of publications with significant contributions:

ATLAS Collaboration. “Search for a scalar partner of the top quark in the jets plus missing transverse momentum final state at  $\sqrt{s}=13$  TeV with the ATLAS detector”. In: *JHEP* (2017), p. 57. DOI: [10.1007/JHEP12\(2017\)085](https://doi.org/10.1007/JHEP12(2017)085). arXiv: [1709.04183 \[hep-ex\]](https://arxiv.org/abs/1709.04183)

Co-authored on 153 publications with minor contributions. These can be found at Inspire (search parameters: exactauthor:I.M.Snyder.1)

## ACKNOWLEDGEMENTS

I would like to thank my advisor Stephanie Majewski for giving me this opportunity and guiding me through it, as well for the years of both professional and personal advice. I would also like to thank the rest of my committee for the education and instruction they provided, especially the head of my committee, Jim Brau. I would also like to thank Michael Begel for his patience and instruction during the year I worked with him at Brookhaven National Laboratory and the Department of Energy that provided the opportunity to work there with the SCGSR program. I'm also thankful to Walter Hopkins, who provided a lot of advice and showed me some slick coding tricks, and to the other students and postdocs who helped me along the way, including but not limited to Ben Allen, Jason Barkaloo, John Myers, Chaowaroj 'Max' Wanotayaroj, Kate Whalen, Aparajita Dattagupta, Giordon Stark, et cetera.

This work would also not have been possible without the constant patience and support of my wife, Amanda Tumminelli, and our families, especially my Mom who always believed in me.

## TABLE OF CONTENTS

Chapter	Page
I. INTRODUCTION . . . . .	1
1.1. The Standard Model . . . . .	2
1.2. Beyond the Standard Model . . . . .	11
II. MOTIVATION FOR TOP PARTNER SEARCHES . . . . .	17
2.1. Hierarchy Problem . . . . .	18
2.2. Dark Matter . . . . .	18
2.3. Gauge Coupling Unification . . . . .	20
2.4. Particle Contents . . . . .	20
2.5. Supersymmetry Breaking . . . . .	23
2.6. Minimal Supersymmetric Standard Model . . . . .	24
2.7. Phenomenological MSSM . . . . .	25
III. EXPERIMENTAL SETUP . . . . .	26
3.1. Proton-proton Collisions at the Large Hadron Collider . . . . .	26
3.2. Overview of the ATLAS Detector . . . . .	32
3.3. Liquid Argon Calorimetry at ATLAS . . . . .	39
3.4. The ATLAS Trigger System . . . . .	46

Chapter		Page
3.5.	Calorimeter Trigger Phase I Upgrades . . . . .	48
3.6.	Calorimeter Trigger Phase II Upgrades . . . . .	52
IV.	OVERVIEW OF THE GLOBAL FEATURE EXTRACTOR . . . . .	55
4.1.	Global Feature Extractor Phase I Upgrade . . . . .	55
4.2.	Pileup Suppression . . . . .	59
4.3.	Calibration . . . . .	60
4.4.	Effects of Calibration on $p_T$ and $E_T^{\text{miss}}$ . . . . .	62
4.5.	Trigger Efficiencies and Rate . . . . .	63
4.6.	Outlook . . . . .	65
V.	ANALYSIS OVERVIEW . . . . .	67
VI.	EVENT RECONSTRUCTION . . . . .	79
6.1.	Particle Identification . . . . .	79
6.2.	Jets . . . . .	80
6.3.	Electrons . . . . .	86
6.4.	Photons . . . . .	87
6.5.	Muons . . . . .	87
6.6.	Taus . . . . .	89
6.7.	Missing Transverse Momentum . . . . .	89
6.8.	Monte Carlo Simulations . . . . .	90

Chapter	Page
VII. ANALYSIS . . . . .	95
7.1. Signal Region Definitions . . . . .	95
7.2. Background Estimation . . . . .	106
7.3. Systematic Uncertainties . . . . .	119
7.4. Fitting Procedure . . . . .	123
7.5. Results . . . . .	128
7.6. Interpretations . . . . .	133
7.7. Outlook . . . . .	139
VIII. CONCLUSIONS . . . . .	143
APPENDICES	
A. STANDARD MC AND DATA CHECKS . . . . .	145
B. SIGNAL CONTAMINATION . . . . .	153
REFERENCES CITED . . . . .	160

## LIST OF FIGURES

Figure	Page
1.1. $Z$ with jets production mechanism . . . . .	7
1.2. Diboson production . . . . .	7
1.3. Branching fractions of the decay channels of the top quark . . . . .	9
1.4. Top-antitop pair production . . . . .	9
1.5. $t\bar{t} + Z$ production . . . . .	10
1.6. Higgs boson decay modes . . . . .	12
1.7. Make it, break it, shake it . . . . .	14
1.8. Coupling evolution . . . . .	15
2.1. Gauge coupling unification . . . . .	20
2.2. Illustration of the pMSSM as a subset of SUSY theories . . . . .	25
3.1. The LHC accelerator complex . . . . .	28
3.2. Integrated luminosity for individual years of running . . . . .	30
3.3. Pileup during data taking in 2015-2017 . . . . .	31
3.4. Cut-away view of ATLAS showing where particles deposit tracks and energy . . . . .	33
3.5. Cut-away view of the ATLAS detector and its subsystems . . . . .	34
3.6. Layout of the ATLAS toroid magnets . . . . .	35
3.7. Cut-away view of the ATLAS inner detector . . . . .	37
3.8. Cut-away view of the ATLAS calorimeters . . . . .	38
3.9. Number of radiation lengths ( $\chi_0$ ) as a function of $\eta$ . . . . .	39
3.10. Number of interaction lengths as a function of $\eta$ . . . . .	40

Figure	Page
3.11. An illustration of a LAr calorimeter module in the barrel region . . . . .	41
3.12. Signal shape before and after shaping . . . . .	42
3.13. Signal propagation through the LAr electronics . . . . .	43
3.14. Electron uncertainty as a function of $p_T$ and $\eta$ . . . . .	45
3.15. Cut-away view of ATLAS Muon System . . . . .	47
3.16. Trigger Towers vs. Super Cells . . . . .	50
3.17. Schematic diagram of the LAr trigger readout architecture after the Phase I upgrade . . . . .	51
3.18. L1Calo system after the Phase I upgrade . . . . .	52
3.19. Schematic diagram of the LAr trigger readout architecture after the Phase II upgrade . . . . .	54
4.1. L1Calo system after the Phase I upgrade . . . . .	56
4.2. Layout of the gFEX . . . . .	58
4.3. Distribution of pileup across all events . . . . .	60
4.4. Energy response of gTowers . . . . .	61
4.5. Energy response of the gTowers after a noise cut as a function of $\eta$ for various energies of truth jets. . . . .	61
4.6. Energy response of gBlocks . . . . .	62
4.7. Distributions of gBlock $p_T$ . . . . .	63
4.8. Distributions of gTower $E_T^{\text{miss}}$ . . . . .	64
4.9. gBlock trigger efficiencies . . . . .	65
4.10. gBlock Trigger Rates . . . . .	66
5.1. Cross section for direct stop pair production and selected backgrounds. . .	68
5.2. Top quark decay topologies. . . . .	69
5.3. Illustration of signal regions. . . . .	70

Figure	Page
5.4. Top quark mass categories. . . . .	71
5.5. SM fiducial production cross sections. . . . .	73
5.6. Backgrounds in SRB. . . . .	73
5.7. Checks on the dependence of pileup of $m_{\text{jet},R=1.2}^0$ , $E_{\text{T}}^{\text{miss}}$ , and jet multiplicity. . . . .	76
5.8. Exclusion contours in as a function of $\tilde{t}_1$ and $\tilde{\chi}_1^0$ masses in the scenario where both top squarks decay via $\tilde{t}_1 \rightarrow t^{(*)}\tilde{\chi}_1^0$ . . . . .	78
6.1. Infrared sensitivity and collinear sensitivity . . . . .	81
6.2. Jet finder algorithms . . . . .	82
6.3. Jet calibration steps at ATLAS . . . . .	83
6.4. Simplified diagram of an event . . . . .	92
6.5. Representation of different stages of simulation . . . . .	94
7.1. Distributions of the discriminating variables $m_{\text{jet},R=1.2}^0$ and $m_{\text{T}}^{b,\text{min}}$ after common preselection. . . . .	98
7.2. $\Delta R$ between the $W$ and the $b$ -quark vs. the top $p_{\text{T}}$ . . . . .	106
7.3. Postfit distributions of several discriminating variables in CRT . . . . .	113
7.4. Distribution of kinematic variables in CRZ, CRTC, CRW, CRST, and CRTTGamma. . . . .	120
7.5. Final yields for all the validation and signal regions . . . . .	129
7.6. Distribution of several kinematic variables in the signal regions . . . . .	130
7.7. Exclusion contours as a function of $\tilde{t}_1$ and $\tilde{\chi}_1^0$ masses in the scenario where both top squarks decay via $\tilde{t}_1 \rightarrow t^{(*)}\tilde{\chi}_1^0$ . . . . .	134
7.8. Exclusion contours for the Natural SUSY-inspired mixed grid scenario . .	135
7.9. Exclusion contours for the scenario where both gluinos decay via $\tilde{g} \rightarrow t\tilde{t}_1 \rightarrow t\tilde{\chi}_1^0$ . . . . .	136
7.10. Exclusion contours for the pMSSM-inspired non-asymptotic higgsino simplified model. . . . .	138

Figure	Page
7.11. Exclusion contours for the Wino NLSP pMSSM model. . . . .	139
7.12. Exclusion contour for the well-tempered pMSSM model. . . . .	140
7.13. Significance as a function of integrated luminosity for a 1000 GeV stop . . . . .	141
A.1. Distribution of various variables in Data and Monte Carlo used as a function of number of vertices. . . . .	146
A.2. Lumi-normalized distribution of run numbers in 2015 and 2016 in $t\bar{t}$ control regions. . . . .	147
A.3. Lumi-normalized distribution of run numbers in 2015 and 2016 in $t\bar{t}$ control regions. . . . .	148
A.4. Lumi-normalized distribution of run numbers in 2015 and 2016 in $Z$ and $t\bar{t} + \gamma$ control regions. . . . .	149
A.5. Lumi-normalized distribution of run numbers in 2015 and 2016 in validation regions. . . . .	150
A.6. Lumi-normalized distribution of run numbers in 2015 and 2016 in validation regions. . . . .	151
A.7. Distribution of n vtx before reweighting (blue) and after reweighting (red) compared to data (black). . . . .	152
B.1. Signal contamination for stop production as a function of stop and neutralino masses for CRTop. . . . .	153
B.2. Signal contamination for stop production as a function of stop and neutralino masses for CRZ, CRST, and CRW. . . . .	154
B.3. Signal contamination for SRD for CRTop. . . . .	155
B.4. Signal contamination for SRD for CRZ, CRST, and CRW. . . . .	155
B.5. Signal contamination for SRE for CRTop. . . . .	156
B.6. Signal contamination for SRE for CRZ, CRST, and CRW. . . . .	156
B.7. Signal contamination for stop production as a function of stop and neutralino masses for VRTop. . . . .	157
B.8. Signal contamination for stop production as a function of stop and neutralino masses for VRZ, and VRW. . . . .	157

Figure	Page
B.9. Signal contamination for stop production as a function of stop and neutralino masses for VRTop. . . . .	158
B.10. Signal contamination for stop production as a function of stop and neutralino masses for VRZ, and VRW. . . . .	158
B.11. Signal contamination for stop production as a function of stop and neutralino masses for VRTop. . . . .	159
B.12. Signal contamination for stop production as a function of stop and neutralino masses for VRZ, and VRW. . . . .	159

## LIST OF TABLES

Table	Page
1.1. Particles of the Standard Model[2] . . . . .	3
1.2. Generations of the Standard Model. . . . .	8
2.1. Standard Model particles and their associated superpartners. . . . .	22
6.1. Overview of the nominal simulated samples. . . . .	93
7.1. Signal region selection criteria. . . . .	99
7.2. Selection criteria for SRA and SRB. . . . .	101
7.3. Selection criteria for SRC . . . . .	103
7.4. Selection criteria for SRD . . . . .	104
7.5. Selection criteria for SRE . . . . .	105
7.6. Selection criteria for the $Z + \text{jets}$ control regions used to estimate the $Z + \text{jets}$ background contributions in the signal regions. . . . .	107
7.7. Lepton triggers . . . . .	108
7.8. Selection criteria for the $Z$ validation regions . . . . .	109
7.9. Selection criteria for the $t\bar{t}$ control regions used to estimate the $t\bar{t}$ background contributions in the signal regions. . . . .	112
7.10. One-lepton $t\bar{t}+\text{ISR}$ control region definitions. The same $E_{\text{T}}^{\text{miss}}$ triggers as mentioned in Table 7.1 are used. . . . .	114
7.11. VRTA and VRTB region definitions. . . . .	115
7.12. VRTC, VRTD and VRTE Selection criteria. . . . .	116
7.13. Selection criteria for the common $W + \text{jets}$ , single-top, and $t\bar{t}+\gamma$ control-region definitions. . . . .	117
7.14. Fitted scale factors for the MC background samples based on $36.07 \text{ fb}^{-1}$ of data. . . . .	124

Table	Page
7.15. Observed and expected yields, before and after the fit, for SRA and SRB . . . . .	125
7.16. Observed and expected yields, before and after the fit, for SRC . . . . .	126
7.17. Observed and expected yields, before and after the fit, for SRD and SRE . . . . .	127
7.18. 95% CL upper limits . . . . .	132

## CHAPTER I

### INTRODUCTION

Ever since the ancient Greeks philosophized on the smallest bit of materials, people have wondered what are the basic building blocks of matter. With the development of science, the search for answers changed from philosophizing to experimentation and in the last several centuries atoms were discovered. Of course, the atom is not the most fundamental building block of matter; its nucleus is made up of protons and neutrons, with electrons orbiting it. Protons and neutrons are in turn made up of quarks, and whether these are fundamental and point-like is still being investigated.

Additional quarks and leptons that do not exist in ordinary matter have also been discovered, along with other fundamental particles. These particles and the forces that determine their interactions make up the Standard Model of Particle Physics (SM) and are shown in Table 1.1. These particles are heavier than those found in ordinary matter and are highly unstable. In order to create these particles experimentally physicists need to reach higher and higher energies. To achieve these energies, colliders accelerate particles such as protons to a very high momentum and then impact them with other particles. Experimental particle physicists develop and use these colliders, which are among the largest experiments in history.

Particle physics is not just useful for the very small; while particle physicists were probing the building blocks of matter, astronomers and cosmologists were looking to the skies to understand the origin and fate of our universe. The particles and

interactions in the SM also govern the life cycle of stars and the creation of heavy elements. Dark matter, which is known to exist but not predicted by the SM, determines the large-scale structure of the universe. Thus particle physics attempts to describe both the very small and very large.

This chapter will introduce the Standard Model and discuss SM processes relevant to the topic of this thesis, as well as present physics that the SM fails to explain, and Chapter II discusses a possible solution to a few of the most glaring issues. Chapter III presents the experimental apparatus used in this search, and Chapter IV discusses one of the upgrades to the detector, the Global Feature Extractor. Chapter V gives an overview of the stop search and Chapter VI describes how events are reconstructed. Chapter VII describes the analysis in detail and Chapter VIII concludes the dissertation and presents the outlooks for the future of the analysis. Chapters V and VII include material coauthored with the ATLAS Collaboration.

## 1.1. The Standard Model

The Standard Model of Particle Physics has been developed and tested by many experiments and stands as our most accurate theory describing the microscopic world. In the SM all matter is made up of fermions (spin- $\frac{1}{2}$  particles). Fermions are composed of quarks and leptons.

Ordinary matter is made up of the first generation; protons ( $uud$ ), neutrons ( $udd$ ), and electrons make up atoms. The remaining quarks make up more exotic and short-lived hadrons we see in collider experiments and in cosmic radiation. The

remaining leptons, with the exception of neutrinos, can be thought of as heavy versions of the electron and are unstable. A summary of all particles in the SM can be found in Table 1.1.

TABLE 1.1. Particles of the Standard Model[2].

	Particle	Spin	Charge	Mass
<b>Quarks</b>				
u family	$u$	$\frac{1}{2}$	$\frac{2}{3}$	$2.2^{+0.6}_{-0.4}$ MeV
	$c$			$1.28 \pm 0.03$ GeV
	$t$			$173.1 \pm 0.6$ GeV
d family	$d$	$\frac{1}{2}$	$-\frac{1}{3}$	$4.7^{+0.5}_{-0.4}$ MeV
	$s$			$96^{+8}_{-4}$ MeV
	$b$			$4.18^{+0.04}_{-0.03}$ GeV
<b>Leptons</b>				
e family	$e$	$\frac{1}{2}$	-1	$0.5109989461 \pm 0.000000003$ MeV
	$v_e$		0	$< 2$ eV
$\mu$ family	$\mu$	$\frac{1}{2}$	-1	$105.6583745 \pm 0.0000024$ MeV
	$v_\mu$		0	$< 2$ eV
$\tau$ family	$\tau$	$\frac{1}{2}$	-1	$1776.86 \pm 0.12$ GeV
	$v_\tau$		0	$< 2$ eV
<b>Bosons</b>				
Vector	$\gamma$	1	0	$< 10^{-18}$ eV
	$g$	1	0	0
	$W$	1	$\pm 1$	$80.385 \pm 0.015$ GeV
	$Z$	1	0	$91.1876 \pm 0.0021$ GeV
Scalar	Higgs	0	0	$125.09 \pm 0.21 \pm 0.11$ GeV

### 1.1.1. Force Carriers

Vector bosons (integer spin) act as force carriers in the SM. Force carriers are quanta of energy of a particular field and transfer forces between particles.

#### 1.1.1.1. Photons

Photons ( $\gamma$ ) are massless, chargeless, and are the force-carriers in Quantum Electrodynamics (QED). QED governs the interactions of charged matter and describes how photons and matter interact. The coupling constant, which indicates coupling strength, is of order  $10^{-2}$ .

In addition to being important in production and decays of particles, QED interactions are used in detectors. For example, calorimeters take advantage of the following processes:

- Photoelectric effect: photons are absorbed by a material and charge carriers, usually electrons, are emitted by the material
- Compton scattering: a particle absorbs a photon, recoils and emits a photon with less energy
- Pair production: a photon of sufficient energy decays into an electron and positron
- Bremsstrahlung: a charged particle loses energy by emitting a photon when deflected by an electric or magnetic field

These interactions cause a cascade, or shower, of particles whose energy can be measured. This is further discussed in Section 3.2.4.

### 1.1.1.2. Gluons

Gluons are also massless and chargeless and are the force-carriers in Quantum Chromodynamics (QCD), which describes strong interactions between quarks in the SM. Gluons carry color, the analog to electric charge in the strong force (although photons do not carry charge while gluons carry color). The coupling constant is for the strong force is of order 1 but is limited to short distances.

Gluons also play a main role in particle production in hadron colliders. Since both beams of particles in the collision at the LHC are protons, compared to protons and antiprotons at the Tevatron, there are very few antiquarks to annihilate with quarks to produce particles. Instead, most production is from gluon fusion, in which two gluons fuse into a single high energy gluon which in turn can decay into other particles.

Unlike the other forces, the strong force increases as two quarks are pulled apart, and a quark-antiquark pair will be created from input energy before quarks can be free. Quarks therefore exist in bound states, hadrons, with either a quark-antiquark pair, called mesons, or sets of three quarks (antiquarks) called baryons (antibaryons).

In a collision a highly energetic quark or gluon can fragment into a collimated spray of hadrons, called jets. Production of two back-to-back jets, called a dijet event, are very common at the LHC, as are multijet events. By measuring the energy and direction of a jet, one can measure properties of the original parton. Jets are discussed more in Section 6.2.

It is possible for a particle to emit radiation prior to annihilating with the oncoming beam of particles; this is called initial-state radiation (ISR). When a final state particle emits radiation it is referred to as final-state radiation (FSR). ISR can change the momentum of the particles produced as the interacting particles recoil against the ISR particles.

#### 1.1.1.3. $W$ and $Z$ Bosons

The  $W$  and  $Z$  bosons are the force carriers for the weak force. Unlike the other force carriers, these are very massive and the  $W$  bosons are also charged. Because the vector bosons have a large mass, they are short-lived with a lifetime under  $10^{-24}$ s and a coupling constant on the order of  $10^{-6}$  at low energies, although at high energy colliders this coupling can be similar to that of the strong force. The weak force is the only force that affects every fermion in the SM and weak interactions are the only interactions that allow for a particle to change its flavor.

The vector bosons are primarily produced at the LHC in Drell-Yan processes, where the vector boson is a product of quark-antiquark annihilation. Processes that can produce a  $Z$  boson can also occur with heavy flavor jets, such as  $b$ -jets as shown in Figure 1.1.  $Z$  bosons can also be emitted from an off-shell quark, as shown in Figure 1.5 where a  $Z$  is emitted from an off-shell top quark.  $Z$  bosons decay to leptons or quarks about  $\sim 80\%$  of the time and to a neutrino-antineutrino pair  $\sim 20\%$  of the time[2].

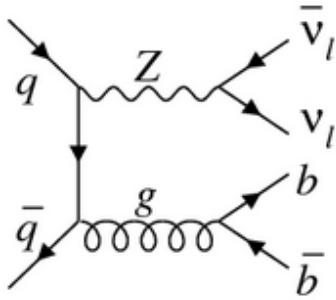


FIGURE 1.1. One possible mechanism for creation of  $Z$  with jets.

Similarly  $W$  bosons can be produced in association with heavy flavor quarks.  $W$  bosons decay leptonically, to a lepton and lepton neutrino,  $\sim 33\%$  of the time and decay hadronically, to a quark-antiquark pair, the remainder of the time. It is possible for a pair of  $W$  bosons to be produced as well; these are called diboson events and are shown in Figure 1.2.

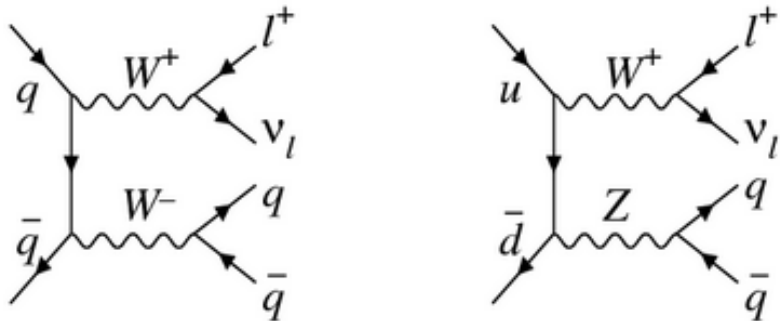


FIGURE 1.2. Examples of bosons produced in pairs in an event.

### 1.1.2. Quarks and Leptons

The quarks and leptons are comprised of three generations as shown in Table 1.2. The first generation of fermions include up ( $u$ ) quarks, down ( $d$ ) quarks, electrons ( $e^-$ ) and electron neutrinos ( $\nu_e$ ). The second and third families, with exception of

the neutrinos, are heavier and will decay to stable particles. There also exists for each matter particle an antimatter particle having that same masses and quantum numbers as the corresponding matter particle except with opposite charge.

TABLE 1.2. Generations of the Standard Model.

	First	Second	Third
up-type quarks	$u$	$c$	$t$
down-type quarks	$d$	$s$	$b$
charged leptons	$e$	$\mu$	$\tau$
neutral leptons	$\nu_e$	$\nu_\mu$	$\nu_\tau$

### 1.1.2.1. The Top Quark

The top quark was discovered in 1995 at the Tevatron[3]. Its distinguishing feature is its extremely heavy mass at 173.1 GeV, compared to the next heaviest quark, the bottom quark, with a mass of 4.5 GeV or the proton with a mass of about 1 GeV. The lightest quark is the up quark and has a mass of 2.4 MeV which is 0.0001% the mass of the top quark.. Due to its heavy mass, the top quark is extremely unstable and have a lifetime of  $5 \times 10^{-25}$  seconds. This is shorter than the time to hadronize and so there are no top hadrons. Because they couple strongly to bottom quarks, they nearly always decay immediately to a bottom quark and a  $W$  boson<sup>1</sup>. Bottom quarks in turn have a longer lifetime because of the small decay rates to up and charm quarks, and so we can detect bottom quarks in detectors by finding a secondary vertex which is displaced from the primary vertex. See Section 6.2.4 for more details.

---

<sup>1</sup> The theoretical rate of top to bottom is 0.999 and the experimentally measured rate is  $1.021 \pm 0.032$ [2].

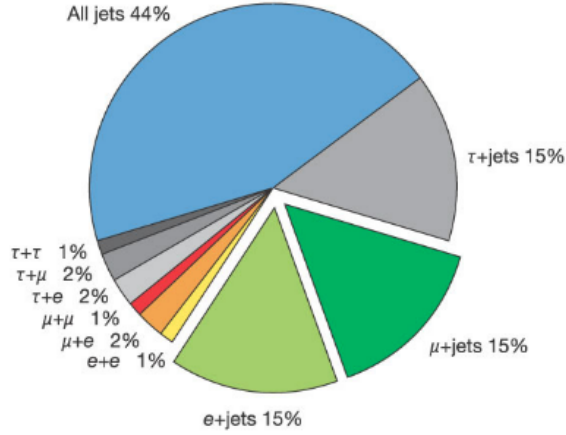


FIGURE 1.3. Branching fractions of the decay channels of the top quark (figure from [4]).

Top quarks can be produced either in pairs, as in Figure 1.4 or as a single top with another quark, such as a bottom quark. After production top quarks decay to a bottom quark and a  $W$  boson.  $W$  bosons decay to either a lepton and neutrino or a quark-antiquark pair the conserves charge (such as a  $u\bar{d}$ ). In the case of the quark-antiquark pair, each of these quarks will hadronize and the final result of the top decay is three jets including a bottom jet.

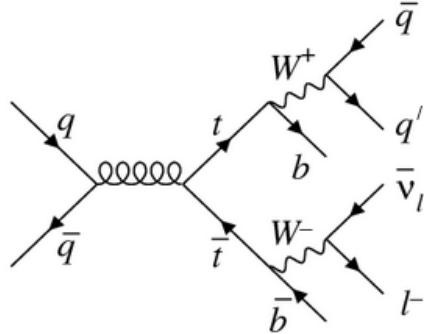


FIGURE 1.4. Top-antitop pair production with one  $W$  boson decaying leptonically and one decaying hadronically.

Top quarks, if off their mass shell, can also emit a  $Z$  boson, as shown in Figure 1.5.

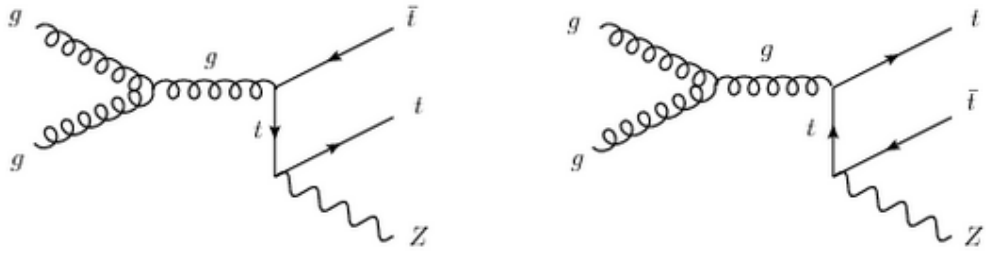


FIGURE 1.5. Two possible production modes for a top-antitop pair and a  $Z$  boson.

### 1.1.3. Electroweak Physics and Higgs Boson

Above about  $10^{15}$  GeV the weak and electromagnetic forces are unified to a single force. At this scale the massless gauge bosons are the  $W_1$ ,  $W_2$ ,  $W_3$ , and the  $B$  bosons. After electroweak symmetry breaking the  $W_1$  and  $W_2$  mix to form the  $W^\pm$  bosons and the  $B$  and  $W_3$  mix to form the  $Z$  boson and the photon. Therefore the electromagnetic and weak forces can be thought of as two aspects of one unified force.

The process by which the vector bosons gain mass is called the *Higgs mechanism*. The Higgs mechanism occurs whenever a field has a nonzero vacuum expectation value (vev). In the SM this only occurs with the field of the Higgs boson since the Higgs field has a nonzero value everywhere. This breaks the symmetry of the electroweak interaction and gives mass to the gauge bosons.

Fermions and vector bosons acquire mass by interacting with the Higgs boson, and the coupling to the Higgs is proportional to the mass of the particle. This coupling is referred to as Yukawa coupling and the top quark, being the most massive particle

in the SM, also has the largest Yukawa coupling with a value of about 1.

The Higgs boson was discovered in 2012 at ATLAS[5] (and CMS[6]) with a mass of  $126.0 \pm 0.4(\text{stat}) \pm 0.4(\text{sys})$  GeV[5]. This was the results of four decades of searches at the Tevatron, LEP, and finally the LHC, and is the first and only fundamental scalar that has discovered. Figure 1.6 shows the branching fractions of the Higgs boson. The Higgs was discovered by a combination of searches in the  $H \rightarrow ZZ^{(*)} \rightarrow 4l$ ,  $H \rightarrow \gamma\gamma$ ,  $H \rightarrow WW^{(*)} \rightarrow e\nu e\nu$ ,  $H \rightarrow b\bar{b}$ , and  $H \rightarrow \tau^+\tau^-$  channels.

## 1.2. Beyond the Standard Model

The Standard Model is an astoundingly accurate theory describing nature. However it is still an incomplete theory; for example it is unable to account for massive neutrinos.

Neutrinos are unique in that they are composed of combinations of mass states. Because of this fact neutrinos will oscillate from one flavor to another[7], for example electron neutrino to muon neutrino. This also means that there are mass differences between the neutrino families, and thus that neutrinos have mass, and the sum of the masses are currently constrained to less than 0.17 eV.[2]. This is not predicted by the SM, which predicts massless neutrinos.

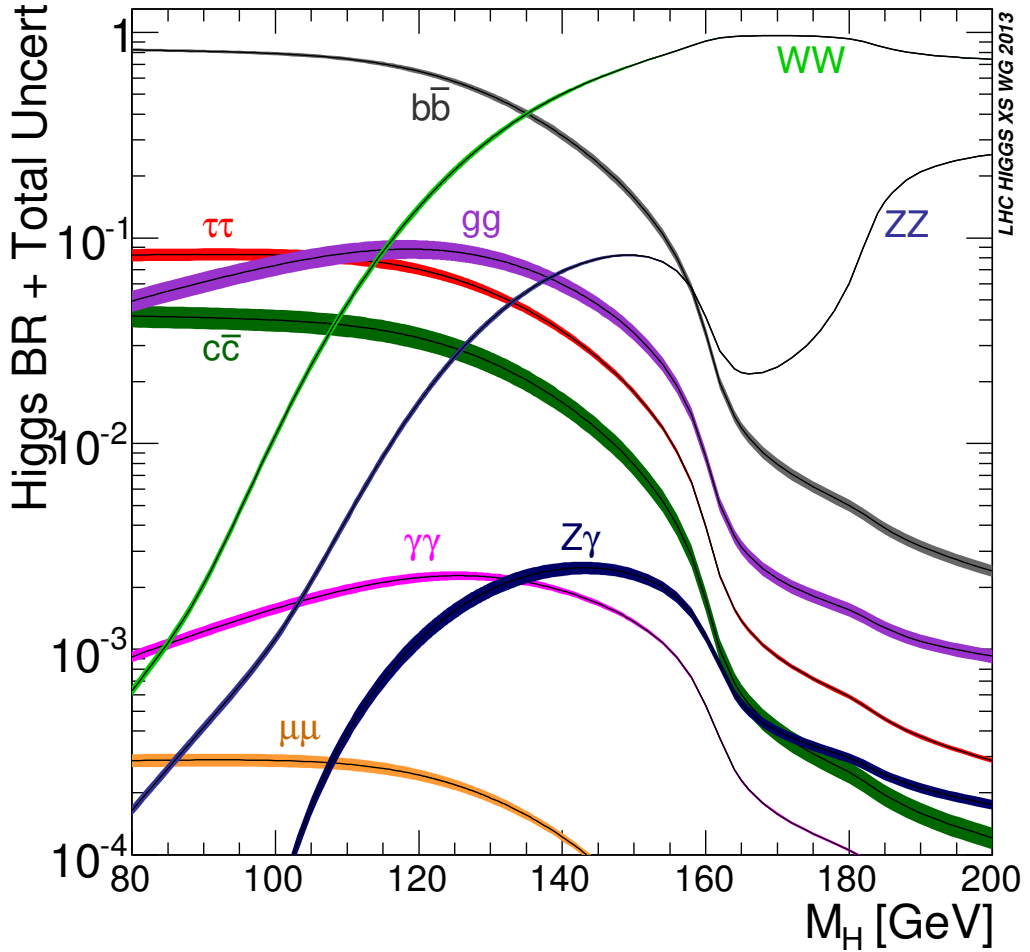


FIGURE 1.6. Decay modes for the Higgs boson as a function of its mass (figure from the ATLAS Collaboration).

Major flaws of the SM include the failure to account for dark matter, lack of gauge unification, and the hierarchy problem.

### 1.2.1. Dark Matter

The SM also only accurately describes the 4.8% of the energy density of the universe as baryonic matter makes up that small fraction; dark energy makes up 69.4% and dark matter makes up 25.8%[8], neither of which are explained by the SM.

The evidence for the existence of dark energy is in the increasingly rapid expansion of the universe.

Dark matter was proposed in the 20<sup>th</sup> century, beginning in 1922 when Jacobus Kapteyn suggested it after observing stellar velocities[9] and again by Fritz Zwicky in 1933 who applied the virial theorem to galaxy rotation and found that most matter in galaxies must be made up of dark matter[10]. It was observed that the stellar velocity was inconsistent with the amount of matter as measured by the brightness of the galaxies and that much more matter was needed to hold the galaxies together. Therefore, there must be some unseen matter. Evidence from galaxy rotation curves came in 1939[11] and again with more accurate measurements in 1980[12]. It was found that the rotation velocity becomes approximately constant as the radius increases, which implies a halo of dark matter with the amount of matter proportional to the radius from the center of the galaxy. Dark matter also has a large effect on the large-scale structure of the universe; by clumping together in the early universe it also gravitationally attracted ordinary matter and is therefore responsible for galaxy formation.

One of the largest pieces of evidence comes from the Bullet Cluster[13], two colliding galaxy clusters. The stars in the clusters passed through the collisions and slightly slowed while gasses, which make up most of the matter of the galaxies, interacted electromagnetically and was slowed much more. Measurements from gravitational lensing showed that most of the matter in the clusters were separated from the baryonic matter, where dark matter had passed through without being

slowed.

While the issue of dark energy is mostly relegated to the realm of cosmology, the issue of dark matter is a problem of particle physics with several approaches, either producing dark matter in colliders, observing possible dark matter decays in cosmic ray detectors, and detecting interactions of dark matter with baryonic matter - sometimes referred to in the field as “make it, break it, shake it” approaches to detecting dark matter, as shown in Figure 1.7. “Making it” means to collide SM particles in an accelerator to produce DM particles; “breaking it” means to observe DM particles annihilating to produce SM particles; and “shake it” refers to direct detection where a DM particle scatters off a SM particle. Since we should be able to create dark matter particles in colliders, searching for dark matter particles and having a viable model to explain it is a high priority.

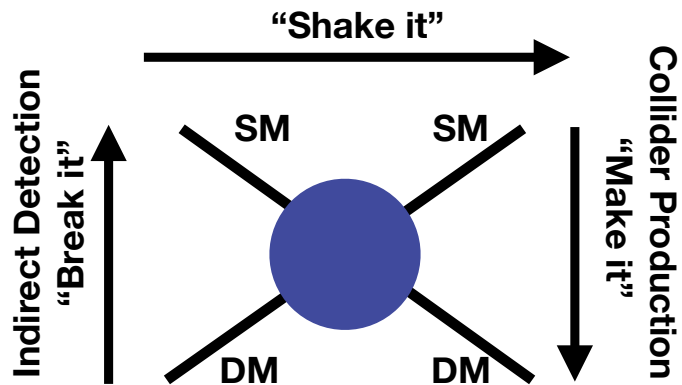


FIGURE 1.7. Three options for detecting dark matter: collider production, where SM particles annihilate to dark matter; direct detection, where dark matter particles scatter off SM particles; and indirect detection, where dark matter particles annihilate to SM particles.

### 1.2.2. Gauge Unification

Since observing that the electromagnetic and weak forces are unified at high energies, a goal of theoretical physics is for all three gauge forces to be unified at some energy. Unfortunately the in the SM this fails, as shown in Figure 1.8, and so there is much work to develop a grand unified theory (GUT) that fixes this.

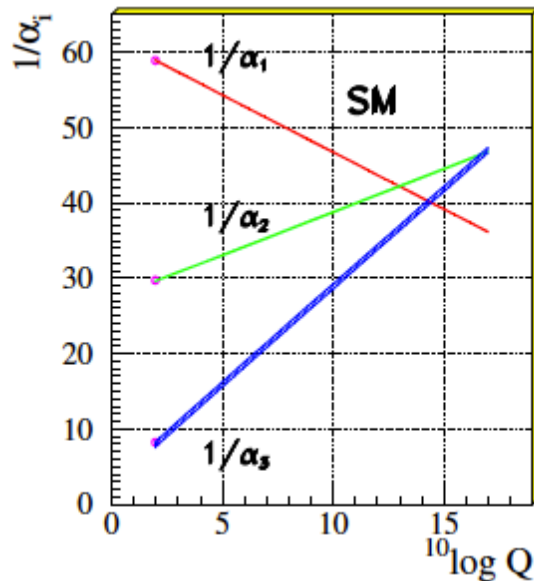


FIGURE 1.8. Evolution of the inverse of the three couplings with increasing energy (figure from [14]). Any two of the three forces unify at sufficient energy but a modification to the SM is needed so that the three couplings unify at the same energy.

### 1.2.3. Hierarchy Problem

The Higgs boson couples to every particle with mass and large quantum corrections should make its mass enormous compared to its measured mass of 125.09 GeV. As a scalar, the correction to  $m_H^2$  from a fermion loop goes as:

$$h^0 \text{---} \begin{array}{c} f \\ \circlearrowleft \end{array} \text{---} = -\frac{\lambda_f^2}{8\pi^2} \Lambda_{\text{UV}}^2 \quad (1.1)$$

where  $\Lambda_{\text{UV}}$  is the ultraviolet cutoff and can be interpreted as the energy scale where new physics comes in to alter the theory. The mass is therefore quadratically sensitive<sup>2</sup> to the cutoff scale; if the value of  $\Lambda_{\text{UV}}$  is on the order of the Planck mass ( $10^{18}\text{-}10^{19}$  GeV) then corrections to the Higgs mass is 30 orders of magnitude above the required value. This means that the mass without any corrections, the *bare mass*, must have a mass that precisely cancels these divergences. This is called *fine-tuning* and the problem is referred to as the hierarchy problem.

Too much fine-tuning is not considered to be *natural*. To maintain  $\sim 1\%$  fine-tuning new physics must come in at the electroweak scale, so this new physics should be accessible at the LHC and is therefore right around the corner.

These flaws motivate Beyond the SM (BSM) theories, which propose new particles and forces, and experiments to test them. One theory that offers a possible solution to these issues with the SM is discussed in Chapter II.

---

<sup>2</sup> While the Higgs is the only particle that has this quadratic dependence in the SM, the other massive particles get their mass from the Higgs and therefore are indirectly affected.

## CHAPTER II

### MOTIVATION FOR TOP PARTNER SEARCHES

Supersymmetry (SUSY)[15–19] is a proposed extension of the SM. It was first proposed as a feature of an early version of string theory, but then developed as a solution to the hierarchy problem. In SUSY there is a boson partner to each fermion in the SM and vice-versa. This means that there is a scalar partner to the top quark, called the stop quark ( $\tilde{t}$ )<sup>1</sup> that cancels the large correction from the top quark. The naming conventions for the SUSY particles are described in Section 2.4. There are similar partners for the other quarks.

With this symmetry there is a transformation that turns a bosonic state to a fermionic one and vice versa; an operator,  $Q$ , that generates such a transformation with:

$$Q|Fermion\rangle = |Boson\rangle, \quad Q|Boson\rangle = |Fermion\rangle \quad (2.1)$$

The fermion and boson states that are transformed to one another by  $Q$  come in pairs (called *supermultiplets*) where the boson and fermion states are *superpartners* of each other have the same mass, as well as the same electric charge, weak isospin, and color degrees of freedom. Additionally, the number of fermionic and bosonic degrees

---

<sup>1</sup> Just as there are left- and right-handed quarks in the SM, there are left- and right-handed SUSY partners,  $\tilde{t}_L$  and  $\tilde{t}_R$  respectively. These mix to form stop eigenstates, the lightest being  $\tilde{t}_1$  and the heavier  $\tilde{t}_2$ . The lighter  $\tilde{t}_1$  is referred to as the  $\tilde{t}$ .

of freedom in a supermultiplet must be equal.

The first three sections of this chapter will describe how SUSY is a solution to the major problems discussed in Chapter I. Then additional considerations of SUSY will be discussed, including more details about the particles it introduces and how it is broken, and then introduce a specific SUSY theory and how it is searched for at ATLAS.

## 2.1. Hierarchy Problem

As discussed in Section 1.2.3, one-loop corrections to the Higgs mass results in large divergences. One solution is to introduce additional physics that adds diagrams to cancel the troublesome diagrams, as:

$$\text{---} \tilde{t} \text{---} = +\frac{\lambda_f^2}{8\pi^2} \Lambda_{\text{UV}}^2 \quad (2.2)$$

This is because the sign difference between the fermion and scalar loops leads to the cancellation of the fermion loops and also persists to higher order loop corrections. The existence of such scalars arises naturally if there exists a symmetry relating bosons to fermions, as in SUSY.

## 2.2. Dark Matter

In some SUSY models lepton and baryon numbers can be violated, which results in the lifetime of a proton being shorter than observed[20]. It is not desirable to simply

take baryon and lepton conservation as a postulate because it is a consequence of the SM. However a new symmetry, called “matter parity” can be introduced, defined as:

$$P_M = (-1)^{3(B-L)} \quad (2.3)$$

where  $B$  and  $L$  are the baryon and lepton numbers respectively, for each particle in the theory. Quark and lepton supermultiplets have  $P_M = -1$  while the Higgs supermultiplets have  $P_M = +1$ . Gauge bosons and gauginos, which do not have baryon or lepton number, are assigned  $P_M = +1$ . A candidate term in the Lagrangian is only allowed if the product of all  $P_M$  terms is  $+1$ . This is a more exact and fundamental theory than baryon and lepton number conservation. A new symmetry, “ $R$ -parity,”[21] can be introduced to also account for conservation of spin as:

$$P_R = (-1)^{3(B-L)+2s} \quad (2.4)$$

where  $s$  is the spin of the particle. All the particles in the SM have positive, or even,  $R$ -parity, while all SUSY particles have negative, or odd,  $R$ -parity. If  $R$ -parity is exactly conserved then there is no mixing between SM and SUSY particles. Additionally, the lightest supersymmetric particle must be stable since it cannot decay to SM particles.

The upshot of  $R$ -party is that SUSY naturally provides a viable dark matter candidate[22], giving a solution to the second major problem in the SM. In the early universe when the temperature cooled, dark matter particles no longer had the energy to annihilate with each other to produce SM particles and also could not decay directly into SM particles, leaving a relic density of dark matter particles.

### 2.3. Gauge Coupling Unification

The third major problem in the SM, that the SM the gauge couplings unify at some energy scale, also has a solution in SUSY. In some SUSY models the three gauge coupling constants are unified at an energy scale of  $10^{15}$  or  $10^{16}$  GeV. This is referred to as the grand unified theory (GUT) scale. The unification is not exact but very close, as seen in Figure 2.3 and adjustments can be made approaching the GUT scale.

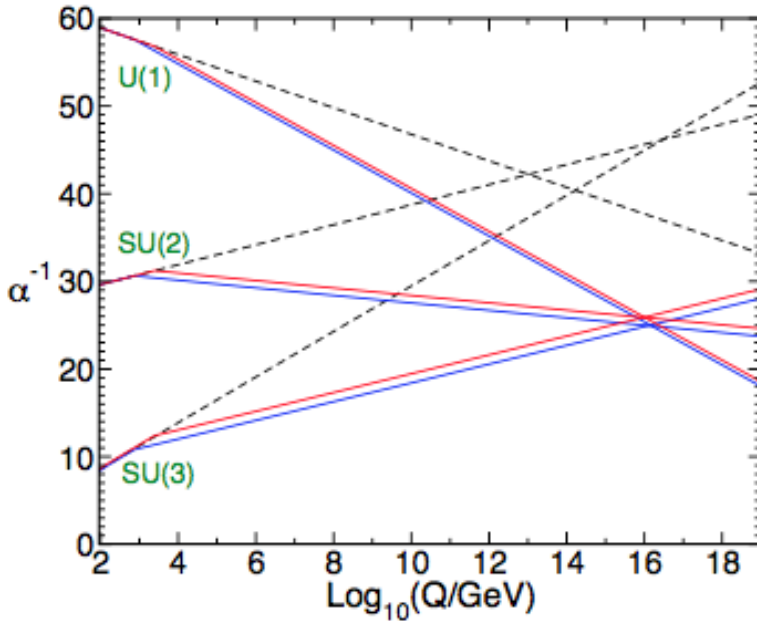


FIGURE 2.1. Renormalization group evolution of inverse gauge couplings in the Standard Model (dashed) and with a SUSY theory (solid) with varying SUSY particle mass thresholds and couplings. The SM couplings do not unify at any point while the MSSM couplings nearly unify at an energy scale of  $10^{16}$  GeV (figure from [23]).

### 2.4. Particle Contents

Only chiral supermultiplets can contain fermions whose left- and right-handed parts transform differently under the gauge group; since all the SM fermions have this property they must be members of the chiral multiplet and therefore the bosonic

partners must be scalar particles, called *sfermions*, named by adding an s (for “scalar”) in front of the standard model particle name, and not spin-1 vector particles. All supersymmetric particles are noted by a tilde ( $\sim$ ) over its letter symbolizing it. The squarks in the first and second families are nearly degenerate (due to smaller Yukawa couplings compared to the third generation) and are much heavier than the sleptons. The stop quark is expected to be the lightest squark as the large Yukawa couplings tend to drive down the masses of the third generation squarks in the renormalization group equations faster than the first two generations[23]. As the masses of the third generation families increase, SUSY becomes less natural and the motivation for SUSY as a solution to the hierarchy problem diminishes.

Alternately, there must be at least two chiral supermultiplet for the Higgs, one to couple to up-type quarks ( $H_u^+, H_u^0$ ) and one to couple to down-type quarks and charged leptons ( $H_d^0, H_d^-$ ). Each of these have a spin-1/2 partner, named by adding “-ino” to the end of the standard model partner, so are named *higgsinos*.

Finally, the gauge bosons have gauge supermultiplets with spin-1/2 superpartners. Similarly to the Higgs, the naming convention is to add “-ino” to the end of the standard model partner, so are named *gauginos*. The partner for the gluon is the *gluino* and the partners for the  $W$  and  $B$  bosons are the *winos* and *bino*. Because of electroweak symmetry breaking, the winos and binos mix to make the zino and photino. The higgsinos and electroweak gauginos mix with each other similarly to the  $W$  and  $B$  bosons mixing in the SM. Also the neutral higgsinos ( $\tilde{H}_u^0, \tilde{H}_d^0$ ) mix with the neutral gauginos ( $\widetilde{W}^0, \widetilde{B}$ ) to create four neutral mass eigenstates called neutralinos,  $\tilde{\chi}_1^0 - \tilde{\chi}_4^0$ , while the charged higgsinos and winos mix to form four charginos,  $\tilde{\chi}_1^\pm - \tilde{\chi}_4^\pm$ .

The lightest neutralino,  $\tilde{\chi}_1^0$ , is the lightest supersymmetric particle (LSP) and is a candidate for dark matter.

The decay of a squark to a quark and gluino will dominate if kinematically allowed. Otherwise squarks can decay to a quark and neutralino or chargino, and the decay to a quark and LSP is kinematically favored and can dominate for right-handed squarks if the LSP is mostly bino. Left-handed squarks may prefer decaying to heavier neutralinos and charginos depending on the coupling to winos compared to binos.

Table 2.1 shows the superpartners of the SM particles.

SM	SUSY partners
Spin-1/2 quarks and spin-0 squarks	
$(u_L \quad d_L)$ $u_R^\dagger$	$(\tilde{u}_L \quad \tilde{d}_L)$ $\tilde{u}_R^*$
$d_R^\dagger$	$\tilde{d}_R^*$
Spin-1/2 leptons and spin-0 sleptons	
$(\nu_L \quad e_L)$ $e_R^\dagger$	$(\tilde{\nu}_L \quad \tilde{e}_L)$ $\tilde{e}_R^*$
Spin-0 Higgs and spin-1/2 Higgsinos	
$(H_u^+ \quad H_u^0)$ $(H_d^0 \quad H_d^-)$	$\begin{pmatrix} \tilde{H}_u^+ & \tilde{H}_u^0 \\ \tilde{H}_d^0 & \tilde{H}_d^- \end{pmatrix}$
Spin-1 gauge bosons and spin-1/2 gauginos	
$g$ $(W^\pm \quad W^0)$ $B^0$	$\tilde{g}$ $(\widetilde{W}^\pm \quad \widetilde{W}^0)$ $\widetilde{B}^0$

TABLE 2.1. Standard Model particles and their associated superpartners.

## 2.5. Supersymmetry Breaking

Particles in multiplets will have the same mass in an unbroken supersymmetry; because this is not the case, as sparticles would have been easily discovered, supersymmetry is a broken symmetry in the vacuum state. Specifically, it must be broken *spontaneously*, meaning that the underlying model is invariant under supersymmetry but the vacuum state is not. This way supersymmetry is hidden at low energies. Since the relationship between the dimensionless couplings of the SM and supersymmetry has to be maintained in order for supersymmetry to be a solution to the hierarchy problem, the idea of “soft” supersymmetry breaking is introduced. The soft terms introduce new Higgs mass corrections as[23]:

$$\Delta m_H^2 = m_{\text{soft}}^2 \left[ \frac{\lambda}{16\pi^2} \ln(\Lambda_{\text{UV}}/m_{\text{soft}}) + \dots \right] \quad (2.5)$$

where  $\lambda$  is a dimensionless coupling term and  $m_{\text{soft}}$  is the mass scale associated with the soft terms. Since the masses of the fermion and their superpartners are not equal the additional diagrams do not perfectly cancel the divergent diagrams. In order to be a viable solution to the hierarchy problem the soft mass term, and thus the lightest supersymmetric particles, should be on the order of the TeV scale.

There are two primary competing proposals for what the mediating interactions may be. The first is new physics that enter at the Planck scale, including gravity, called the Planck-scale-mediated supersymmetry breaking (PMSB). The second proposal is that the interactions for SUSY breaking are the electroweak and QCD gauge interactions in the SM, called gauge-mediated supersymmetry breaking

(GMSB).<sup>2</sup>

## 2.6. Minimal Supersymmetric Standard Model

As previously discussed, the number of fermionic and bosonic degrees of freedom in a supermultiplet must be equal. This means that for the simplest theory with one SUSY transformation ( $Q$ ), called the Minimal Supersymmetric Standard Model (MSSM)[24], the following combinations of supermultiplets are possible, from most to least simple: the *chiral/matter/scalar* multiplet consisting of a Weyl fermion (two spin helicity states) and two real scalars (each with one degree of freedom); the *gauge/vector* multiplet with two degrees of freedom consisting of a massless gauge boson (two helicity states) and a Weyl spin-1/2 fermion; and a gravatino supermultiplet, consisting of a spin-2 graviton (two helicity states) and a massless spin-3/2 gravatino (two helicity states). Any other combination will reduce to these for the MSSM. Other “extended” supersymmetric theories do not reduce to these supermultiplets.

After SUSY breaking, the MSSM adds 105 masses, phases and mixing angles that do not have a counterpart in the ordinary SM, so SUSY breaking introduces an arbitrariness to the theory. One way to handle this is called phenomenological MSSM, or pMSSM.

---

<sup>2</sup> There is also a possibility that the sectors are geographical; in this proposal there are extra spatial dimensions that are of the Kaluza-Klein type or warped type so that there is a physical distance that separates the visible and hidden sectors. This can fit with string theory which suggests six extra spatial dimensions.

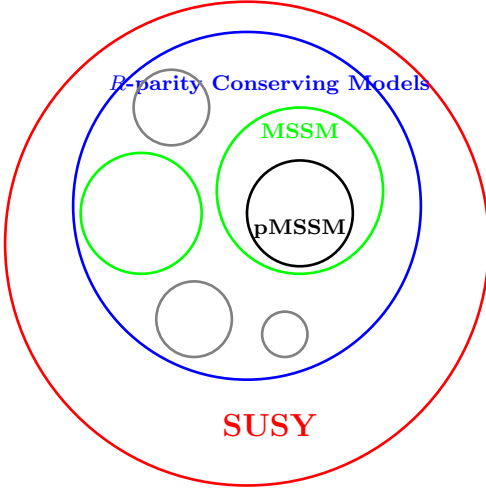


FIGURE 2.2. An illustration of the pMSSM as a subset of the larger MSSM, both under the larger umbrella of SUSY theories (figure based off of [26]).

## 2.7. Phenomenological MSSM

These parameters are reduced in the pMSSM[25] by applying experimental and theoretical constraints to narrow the number to 19. These constraints include assuming  $R$ -parity is conserved, that the LSP is the lightest neutralino, that there is no new CP-violation in the SUSY sector, and no extra flavor changing neutral currents. In addition to these experimental results from electroweak and flavor measurements and searched at LEP and the Tevatron are imposed. Figure 2.2 illustrates how the MSSM and pMSSM fit together in the larger SUSY theory.

This chapter described the theoretical motivations for the analysis described in Chapters V and VII.

## CHAPTER III

### EXPERIMENTAL SETUP

This chapter describes the experimental apparatus that was used in the search: the machine that produces high energy collisions, the Large Hadron Collider (LHC), and the detector used to measure particle properties, ATLAS.

#### 3.1. Proton-proton Collisions at the Large Hadron Collider

The LHC is the world's largest particle accelerator. The tunnel, originally used for the CERN Large Electron-Positron Collider (LEP) and reused for the existing structure to avoid building a new tunnel, is 26.7 km in circumference and lies between 45-170 m underground in order to reduce cosmic radiation backgrounds. The LHC accelerates protons clockwise and counterclockwise around the ring, currently with each beam having an energy of 6.5 TeV, which corresponds to more than 99.9999% of the speed of light. The advantage of a collider over, for instance, a fixed target accelerator, is that the center of mass energy scales as  $E_{CM} = 2E_L$ , where  $E_L$  is the energy of each beam, as opposed to a fixed target accelerator where the center of mass energy scales as  $E_{CM} = \sqrt{E_L}$  due to the necessary contribution to the kinetic energy of the target. Therefore the center of mass energy of the LHC is currently 13 TeV.

The LHC was constructed from 1998-2008. However during testing a faulty electrical connection caused a magnet quench which broke nearby magnets and caused a delay in operations to late 2009 with an original center of mass energy of 7 and 8 TeV during Run 1. Upgrades and repairs from 2012-2015 increased the center of

mass energy to 13 TeV.

While a lepton accelerator would produce cleaner collisions, protons are used to reduce the energy loss from synchrotron radiation, which decreases as the fourth power of the particle mass. Also proton-proton collisions are used instead of proton-antiproton, as was the case of the Tevatron at Fermilab, due to the fact that the time required to produce antiprotons would limit luminosity. This has the effect that nearly all the produced particles stem from gluon-gluon fusion instead of quark-antiquark annihilation. The LHC also produces heavy ion collisions.

It takes several separate machines to accelerate protons to this energy and superconducting magnets are used to focus, steer, and accelerate the protons around the ring. Four main detectors study the collisions; two general purpose detectors, ATLAS and CMS, and two specialty detectors, ALICE (primarily studying heavy ion physics) and LHCb (primarily studying  $b$ -quark physics).

### 3.1.1. Accelerator Complex

Several steps are required to accelerate protons to the energy of the LHC. The protons begin as hydrogen gas (which is composed of a proton with an electron) from bottled hydrogen and is placed into an electric field to strip away the electrons, leaving the positively charged protons. From here the protons are injected into the Linac2, a linear accelerator where they are accelerated to 50 MeV and injected into the Proton Synchotron Booster and accelerated to 1.4 GeV. The Proton Synchrotron then accelerates the protons to 25 GeV, then the Super Proton Synchrotron accelerates

them to 450 GeV. The beam is finally injected into the LHC, where it is accelerated to its final momenta. This is performed using 16 radiofrequency (RF) cavity systems which operate at 400 MHz. The components of the accelerator complex can be seen in Figure 3.1.

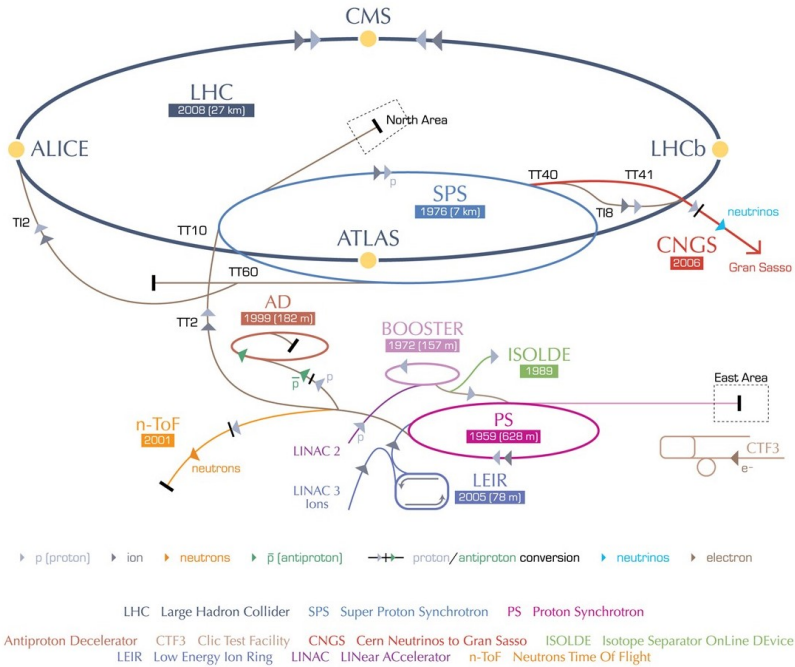


FIGURE 3.1. The LHC accelerator complex (figure from [27]).

The RF cavities generate an oscillating voltage such that the particles are accelerated at the gap, and since the particle must always be accelerated at the gap the RF frequency must be an integer multiple of the revolution frequency. The segments of the circumference of the beam centered on this point are called buckets. Particles that are synchronized with the RF frequency are called synchronous particles and other particles will oscillate around these particles. Therefore particles get clumped around synchronous particles (rather than a uniform spread) in a bunch that is contained in an RF bucket. Because of this the LHC can accelerate a beam made up of 35640

bunches. This is complicated because the PS and SPS are also synchrotrons, and the PS is actually responsible for providing the 25ns spacing that the LHC uses. Also, the buckets can be full of protons or be empty; the empty buckets accommodate the time required to dump the beam. The configuration also determines where the beams cross and collide, which corresponds to different detectors.

The quality of the beam is important, which is expressed in part by beam emittance and beta. Beam emittance refers to the distance a beam is confined to and how similar the particles are in momenta (a small beam emittance corresponds to a closer grouping with the same momentum). A small emittance increases the luminosity by increasing the likelihood of interaction. Beta is determined by the cross section of the bunch and the emittance, so a low beta indicates a more squeezed beam.

### 3.1.2. LHC Magnets

The protons in the beam are steered using 1,232 dipole magnets, each of which are 14.3 meters in length, producing up to 8.4 Tesla magnetic fields. This is achieved using superconducting niobium-titanium (NbTi) Rutherford cables operating at 1.9K with about 11,800 amperes of current.

Because the beams are charged, they will diverge if not focused. Additionally, 392 quadrupole magnets, each between 5-7 meters in length, and each with two apertures, one for each direction, are used to focus the beam. One set of quadrupole magnets squeezes the beam horizontally (QF), another set vertically (QD).

### 3.1.3. Luminosity

Luminosity is defined by the number of collisions produced in a detector per square centimeter per second. This can be determined by the square of the number of particles in a bunch (since each can collide with any in another bunch), the time between bunches, and the cross section of a bunch. This can also be expressed as a function of the beam emittance and beta, as described above. The integrated luminosity, which is the total delivered luminosity, is shown in Figure 3.2 for 2012-2017.

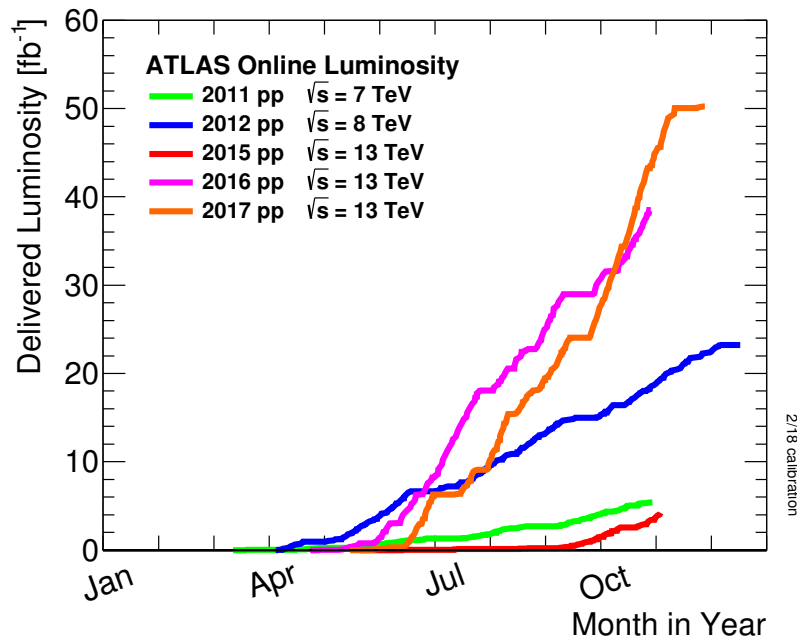


FIGURE 3.2. Integrated luminosity for individual years of running (figure from the ATLAS Collaboration).

### 3.1.4. Pileup

While increasing luminosity is necessary and beneficial for data collection, it corresponds to a major challenge as well; an increase in the number of interactions per bunch crossing, or pileup ( $\langle\mu\rangle$ ). Most interactions are not the hard-scatter events that create potentially interesting physics events, but softer collisions that are not of interest and create noise while raising trigger rates. It's important to reduce pileup as much as possible. Figure 3.3 shows the mean number of interactions per crossing for the years 2015-2017 and can be seen that the number has increased each year.

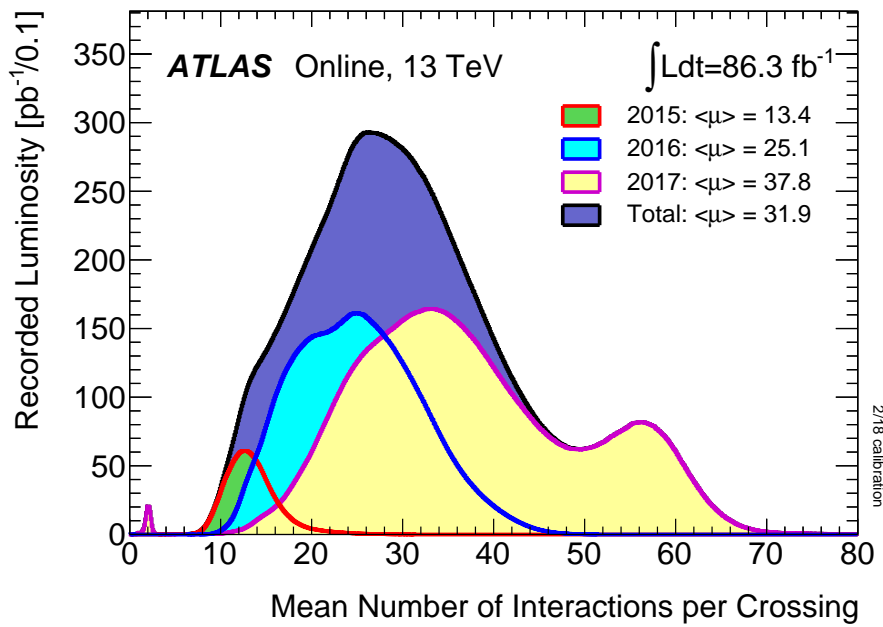


FIGURE 3.3. Pileup during data taking in 2015-2017 (figure from the ATLAS Collaboration).

### 3.2. Overview of the ATLAS Detector

The ATLAS detector, as shown in Figure 3.5, is a general-purpose detector and is the largest detector ever built at 46 meters in length and weighing in at 7000 tons. Its muon system magnets are toroidal in shape, and is perhaps best described as a toroidal LHC apparatus. It's nominally forward-backward symmetric with regards to the interaction point, covering nearly the complete solid angle. It is a general purpose detector that can detect a variety of new physics while also improving Standard Model measurements, and, along with CMS, discovered the Higgs Boson in 2012.

ATLAS uses a variety of technologies to provide accurate and precise measurements of particle trajectories and momenta and consists of three primary subdetectors: the Inner Detector, which measures the paths of charged particles, calorimeters, which measures momenta of charged and neutral particles, and the muon system, which measures the paths of high energy muons. Figure 3.4 shows in what subsystem particles deposit energy or leave tracks. Additionally, the trigger system reduces the event rate from 40 MHz to an order of a kHz to make data collection feasible. A network of computer systems, both on site and off site, allows for data handling and storage as well as supporting analyses.

#### 3.2.1. Coordinate System and Common Variables

ATLAS uses a right-handed coordinate system where the interaction point is the origin of the coordinate system. The beam direction defines the  $z$ -axis and the  $x$ - $y$  plane is transverse to the  $z$ -axis. Positive  $x$  points toward the center of the LHC ring and positive  $y$  points upwards. Side-A of the detector is defined as positive  $z$  and

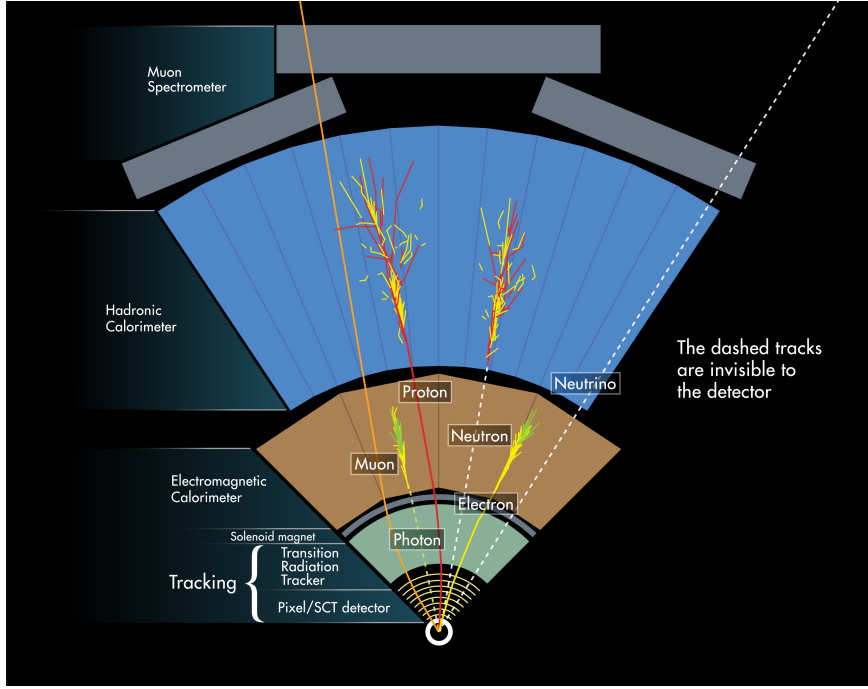


FIGURE 3.4. Cut-away view of ATLAS showing where particles deposit tracks and energy (figure from the ATLAS Collaboration).

side-C as negative. Azimuthal angle  $\phi$  is measured around the beam axis, and the polar angle  $\theta$  defined as the angle from the beam axis. Pseudorapidity,  $\eta$ , is defined as  $\eta = -\ln[\tan(\theta/2)]$  and rapidity,  $y$ , as  $y = \frac{1}{2}\ln(\frac{E+p_z}{E-p_z})$  in the case of massive objects. The transverse momentum,  $p_T$  the transverse energy,  $E_T$ , and the missing transverse momentum (denoted as energy),  $E_T^{\text{miss}}$ , are defined in the  $x$ - $y$  plane. The  $E_T^{\text{miss}}$  is limited to the  $x$ - $y$  axis because momenta of colliding particles (such as gluons) in the  $z$  direction is unknown. Finally, the distance  $\Delta R$  is defined as  $\Delta R = \sqrt{\Delta\eta^2 + \Delta\phi^2}$ .

### 3.2.2. Magnet System

ATLAS has two magnet systems of note, the solenoid magnet and toroid magnets.

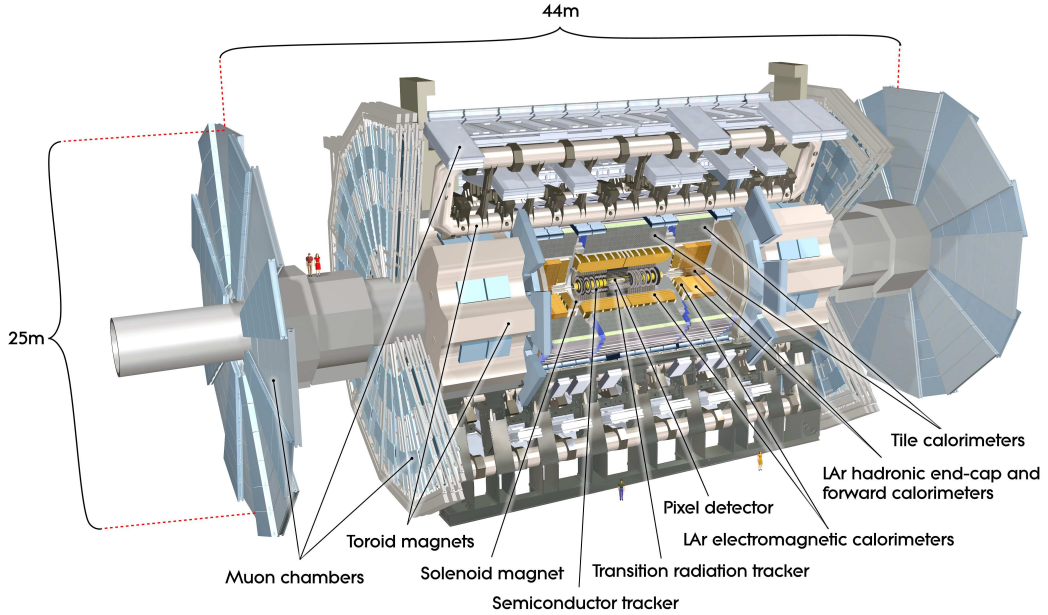


FIGURE 3.5. Cut-away view of the ATLAS detector and its subsystems. Illustrations of people are included to provide a sense of scale (figure from [28]).

A thin superconducting solenoid magnet surrounds the inner detector and creates a 2T field that makes the tracking of charged particles possible.

The toroid system consists of two parts, the endcap and barrel magnets as shown in Figure 3.6. The magnets consists of eight coils, symmetrically arranged around the beam axis and radially assembled, weighing 830 tons. The peak field is of the barrel magnets is 3.9T and 4.1T for the endcap magnets. This strong magnetic field permits tracking high energy muons to determine momentum.

### 3.2.3. Inner Detector

The inner detector, which sits inside the 2T solenoid magnet, is used to reconstruct tracks that charged particles make as they bend in the magnetic field.

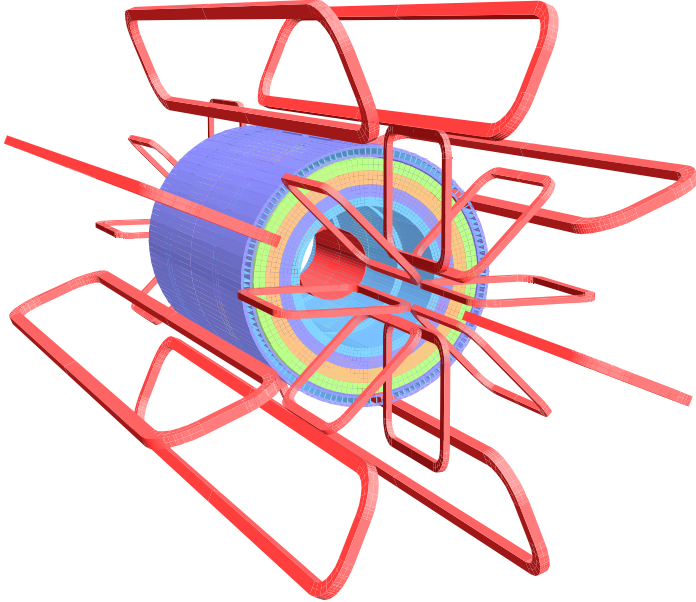


FIGURE 3.6. Layout of the ATLAS toroid magnets (figure from [28]).

It provides hermetic coverage and pattern recognition, extending to  $\eta = 2.5$ , and also provides momentum resolution and both primary and secondary vertex measurement. Secondary vertices are important to identify and measure particles with delayed decays, such as bottom quarks, charm quarks, and tau leptons.

The inner detector consists of several subsystems. Going from innermost to outermost of the beam, they are the Pixel Detector (with the newest addition, the insertable *b*-layer (IBL), added during Long Shutdown I), Semiconductor Tracker (SCT), and the Transition Radiation Tracker(TRT). This can be seen in Figure 3.7.

The IBL was added to be closer to the IP and thus improve vertexing, and involved adding a smaller beam pipe. It uses a combination of planar technology, the same as the silicon pixel layers, and 3D technology, where the electronics pass through

the bulk of the sensors in addition to lying on the surface. The 3D technology covers the outermost 25% of the IBL to improve resolution in the forward regions.

The Pixel Detector consists of four layers. The pixel sensor is made by implanting high positive and negative dose regions on each side of a wafer, so when a charged particle passes through the wafer an electric current passes through it. The design also ensures single pixel isolation and minimizes leakage current. The SCT is a silicon microstrip tracker and can provide up to 4 additional measurement points, so these layers provide good tracking information.

The transition radiation tracker (TRT) consists of 73 straw planes in the barrel and 160 in the endcap, extending to  $|\eta| = 2.0$ . The detector exploits the fact that charged particles emit electromagnetic radiation with moving from one medium to another, in this case carbon dioxide and polypropylene. The energy loss depends on the mass of the particle, so lighter particles emit more of their energy. Emitted EM radiation interacts with the gases inside a tube to increase the current when a charged particle passes though. This can distinguish between, for instance, electrons and pions. While the resolution of the TRT is less than the silicon wafers, extending silicon wafers out to the endpoint of the TRT is cost prohibitive.

### 3.2.4. Calorimeters

Unlike the ID, which changes the path of charged particles to provide tracking information, the calorimeters absorb both charged and neutral particles to measure their energy. The exception to this is muons, which pass through the calorimeters, as

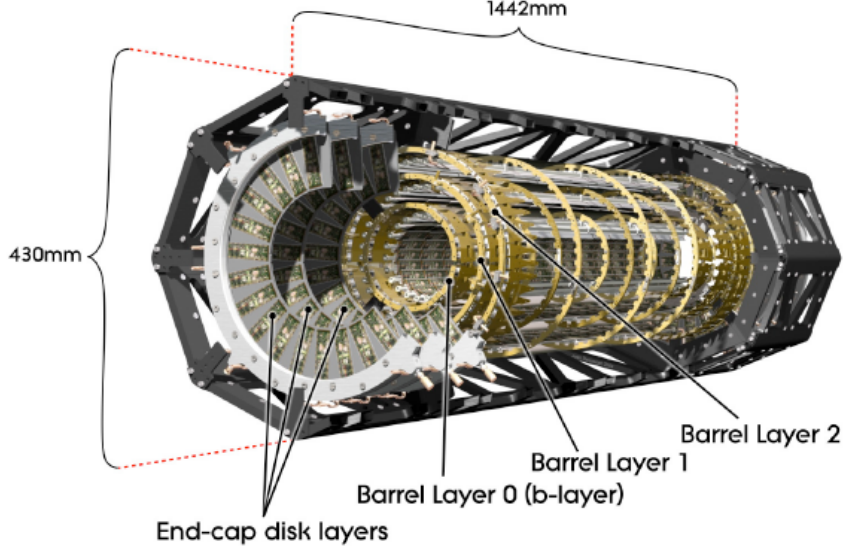


FIGURE 3.7. Cut-away view of the ATLAS inner detector (figure from [29]).

well as neutrinos which pass through the entire detector without detection. This can be done with a homogeneous material, like a scintillator, or with separate layers of absorber and detector material, called a sampling calorimeter. This is the case with the ATLAS liquid argon (LAr) calorimeter, in which lead (absorber) and liquid argon (detector) is arranged in an accordion shape with copper-tungsten sensors as can be seen in Figure 3.11. Lead is chosen because its density increases the probability of interaction with the particles, and argon is chosen because it is radiation hard, stable, and affordable. The particle interacts with the absorber material to generate secondary particles. This in turn creates cascades of particles, the energy of which is measured from ionizations in the detector regions. This aids in measuring neutral particles, the energy of which is measured by the secondary particles they create. The absorptive power is also statistical as a Poisson distribution so precision depends on  $\frac{\Delta E}{E}$  and varies like  $\sqrt{E}$  while spectrometers vary as  $E^2$ . There is also a fast response, which aides in triggering. However, the measured energy is limited to a few tens of

percents of the signal, so statistics has a large effect. The radiation length ( $\chi_0$ ) of a description of a material where, by passing through it,  $1/e$  of a particle's energy is lost to bremsstrahlung (also  $7/9$  of the mean free path for photon pair production). There are at least 25 radiation lengths through any path in the calorimeter. The number of radiation lengths through different portions of the calorimeter is shown in Figure 3.9. The LAr calorimeter primarily measures the energy of electrons and photons.

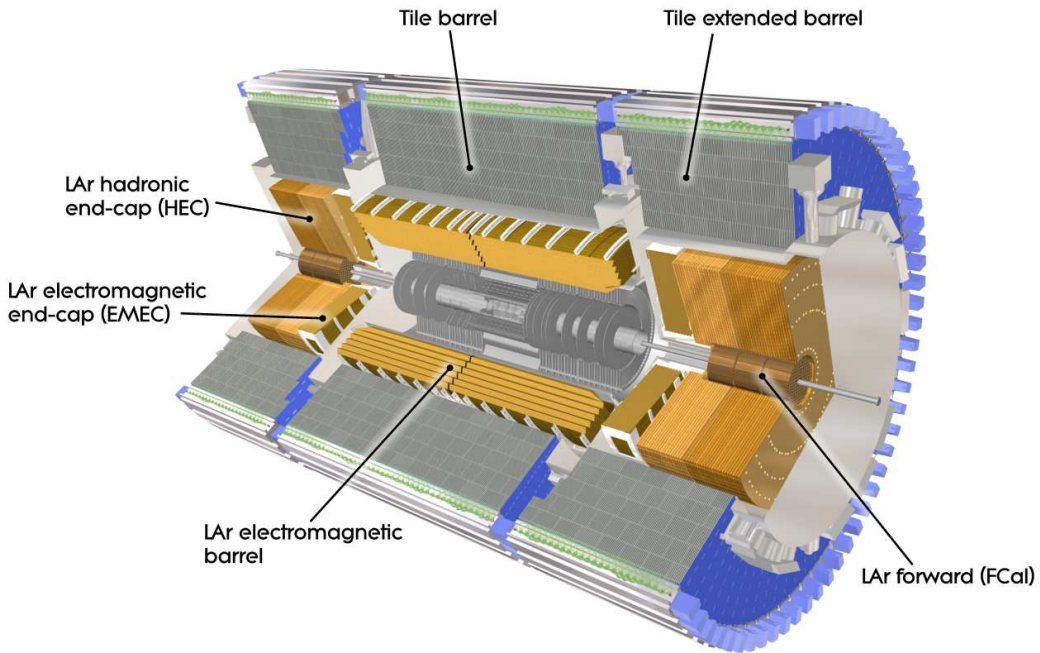


FIGURE 3.8. Cut-away view of the ATLAS calorimeters (figure from [28]).

Hadrons can only be measured by hadron-nucleon interactions, which is characterized by the mean free path of the hadron, its nuclear interaction length. While the EM calorimeter is adequate for absorbing electrons and photons, it is only about 2 nuclear interaction lengths to measure the energy of hadrons. Beyond the

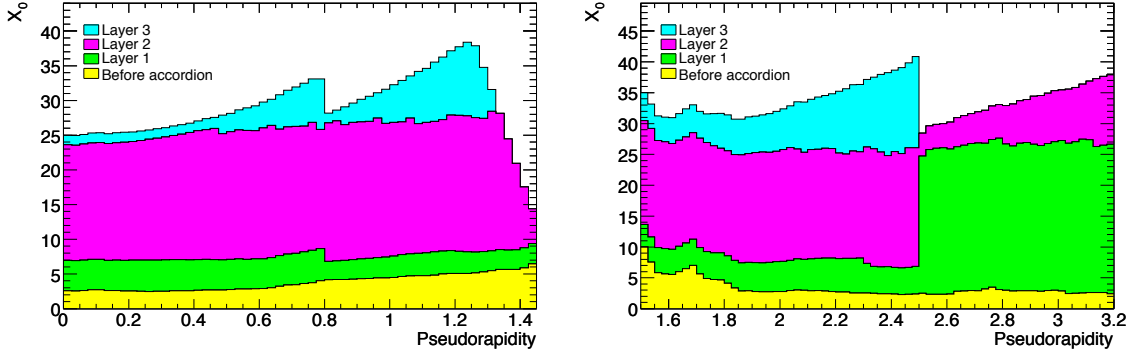


FIGURE 3.9. Number of radiation lengths ( $\chi_0$ ) as a function of  $\eta$  (figure from [28]).

liquid argon calorimeter is the hadronic calorimeter, which adds 9 interaction lengths. The number of interaction lengths through different parts of the hadronic calorimeters is shown in Figure 3.10. The hadronic calorimeter is another sampling calorimeter in which steel is used as absorber and scintillating tiles sandwiched between the steel layers measure the deposited energy. This choice in technology was partly for cost savings as this is a large subdetector, providing coverage up to  $|\eta| < 1.7$  and radially extending from 2.28 m to 4.25 m.

### 3.3. Liquid Argon Calorimetry at ATLAS

As discussed previously, the Liquid Argon calorimeter is a sampling calorimeter capable of absorbing and measuring the energy of charged and neutral particles. The LAr calorimeter covers the pseudorapidity range  $|\eta| < 3.2$ . The hadronic calorimeter is comprised of a scintillator-tile calorimeter, separated into a large barrel and two smaller extended barrel cylinders on each side of the central barrel and covers the pseudorapidity range  $|\eta| < 1.7$ . The endcaps, with  $|\eta| > 1.5$  also use LAr calorimetry and extend to  $\eta = 3.2$ . The LAr forward calorimeters provide EM and hadronic

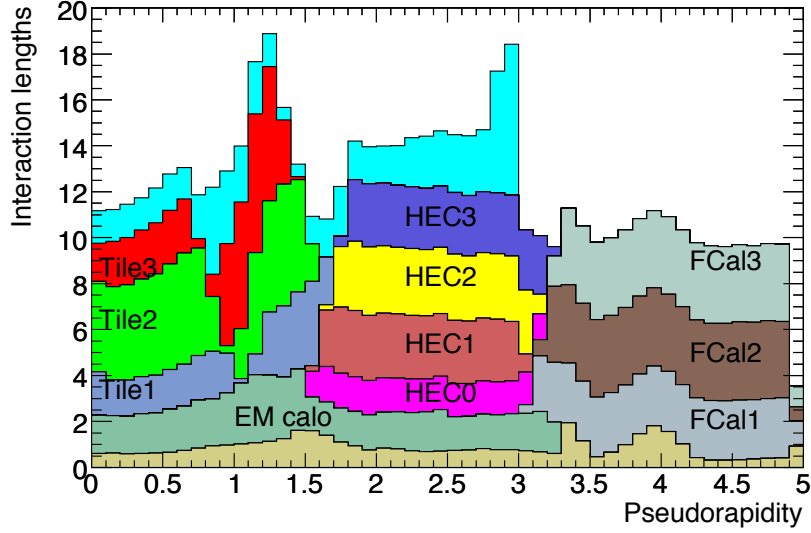


FIGURE 3.10. Number of interaction lengths as a function of  $\eta$  (figure from [28]).

measurements and extend to  $\eta = 4.9$ . Because of the complexity of the arrangement, there are some gaps in the coverage; otherwise, coverage is nearly hermetic.

An aspect to the LAr calorimeter is that it must be kept very cold to operate, so is housed in a cryostat operated at 89K, which contributes to dead material. In order to reduce the total amount of dead material the LAr calorimeter shares the cryostat and vacuum vessel with the solenoid magnet.

The LAr calorimeter typically operates at a 2000V, with some variance, to create a particle avalanche when a charged particle ionizes the liquid argon. There is a presampler layer in the barrel region, which corrects for energy loss in material upstream of the calorimeter, followed by three additional layers, which sum together to form a Trigger Tower, which are analog sums of energy deposits contained in an

area of  $\Delta\eta \times \Delta\phi = 0.1 \times 0.1$  across longitudinal layers of the calorimeters.

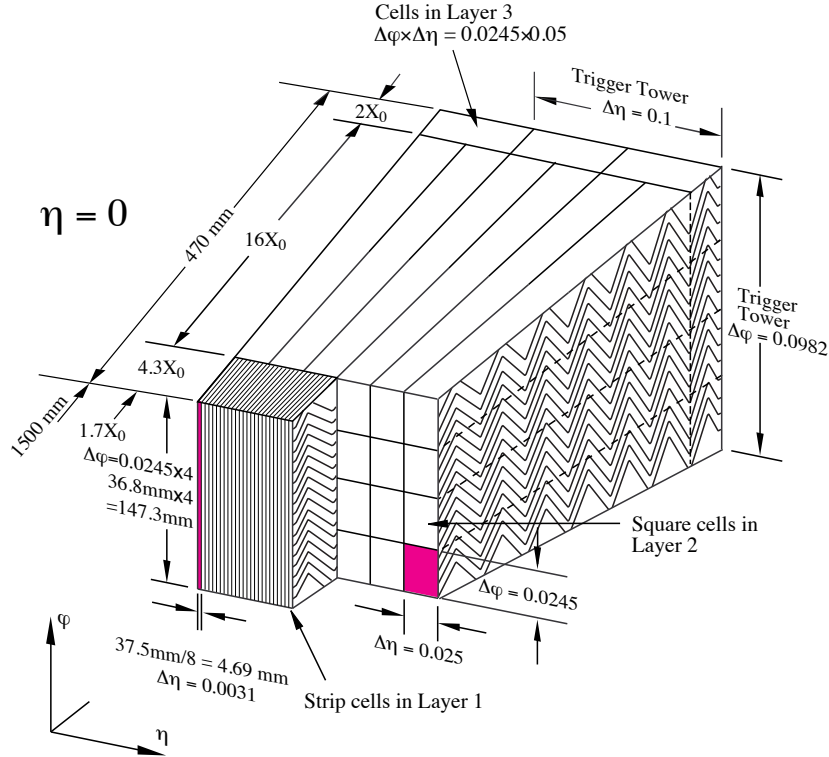


FIGURE 3.11. An illustration of a LAr calorimeter module in the barrel region which shows the accordion structure of the absorbers and the geometry of each section and a Trigger Tower (figure from [30]).

### 3.3.1. Signal Propagation

The drift time in the LAr calorimeter is 400-600 ns, compared to the 25 ns bunch-crossing time. To prevent signal overlapping, an RC-CR<sup>2</sup> shaping with a time constant of 20 ns is applied to analog signals, which minimizes sensitivity to pileup and electronic noise and results in a 100 ns positive pulse and 400 ns negative lobe as shown in Figure 3.12. This pulse shape gives an integral of 0, although it is unlikely that any sampled value is exactly 0. The most likely measured value is called the

pedestal. The most significant quantity for the scale of the signal is the peak current in a readout cell corresponding to an energy deposit. Both the pileup and the mean energy of a calorimeter cell depend on how signals are treated.

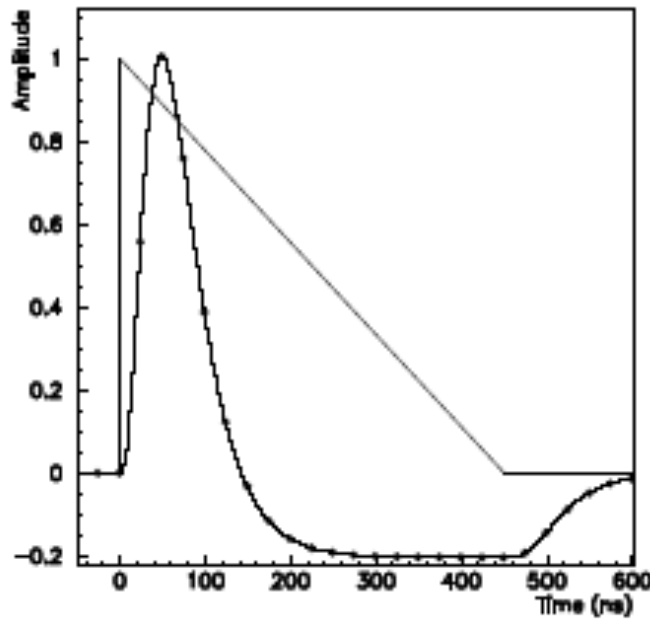


FIGURE 3.12. Signal shape before shaping (triangle) and after shaping (curved with dots). The dots are positions of successive bunch crossings (figure from [28]).

Since the calorimeters use warm preamplifiers (with exception to the HEC) for long term reliability, the shaping stage is designed to handle both pileup and thermal noise. It also must cover a dynamic range in excess of 17 bits, so the range is split by three linear output ranges with gains of 1, 10, and 100. This means that necessary range can be covered by the 12 bit system downstream of the shaper. The shaped signals are sampled and stored in analog form by switched-capacitor array (SCA) analog pipeline chips.

After the front-end board (FEB), off-detector boards perform digital filtering used to extract information from four samples around the peak of the pulse shape. Analog sums are performed in steps due to the large number of channels on the shaper chip, the FEB, and on designated boards in front-end crates and used to form trigger towers. Figure 3.13 shows the signal path in the LAr electronics.

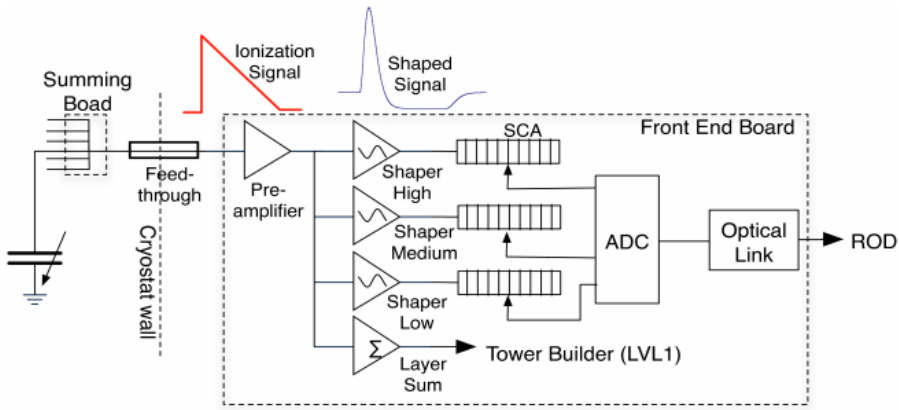


FIGURE 3.13. Signal propagation through the LAr electronics (figure from [31]).

### 3.3.2. Calibration

In order to properly measure the energy deposited in a cell, the calorimeters must be properly calibrated. The conversion of signal Analog to Digital Converter (ADC) samples to raw energy depends on the conversion of ADC to Digital Analog Converter (DAC), called the Ramps, the Optimal Filtering Coefficients, which use a noise autocorrelation function of the samples (the ratio of thermal to pileup noise amplitudes) to maximize the signal/noise ratio and determine the time origin and amplitude of the signal, and the Pedestals as described previously.

In order to calibrate these items:

- Pedestal, noise, and noise autocorrelation: FEBs are read with no input signal and performed separately for each gain
- Ramp: Scan input current and fit DAC vs. ADC curve
- Delay: All cells pulsed with a known current signal and a delay between calibration pulses and DAQ introduced - this allows for full calibration curve to be reconstructed

Once these values are properly set one can go find the energy in a cell with:

$$E = \sum F_j (\sum a_i (ADC_i - P))^j \quad (3.1)$$

where  $E$  is the energy,  $F_j$  are the ramps,  $a_i$  are the OFCs,  $ADC_i$  are the raw samples and  $P$  are the pedestals.

In order to detect the Higgs boson, the uncertainty must be small, especially in channels that led to the Higgs discovery,  $H \rightarrow \gamma\gamma$  and  $H \rightarrow 4l$ . The low uncertainty for electron  $p_T$  can be seen in Figure 3.14 and the uncertainty in the four lepton channel is 0.7% of the overall 8.0%[5].

Calibration is also important for the missing energy trigger. Missing energy, an imbalance of momentum of detected particles, is an indication of new physics as there could be new particles that pass through the detector without interacting with it. Mis-measured energy can give a false positive for a new particle, so any uncertainty pushes up the quantity of missing energy that can be triggered on with reasonable

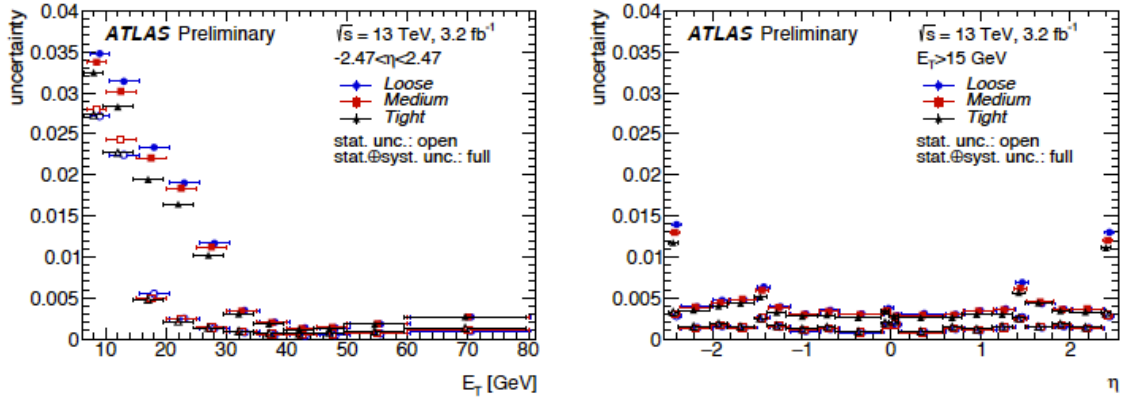


FIGURE 3.14. Electron uncertainty as a function of  $p_T$  (left) and  $\eta$  (right)(figure from [32]). The low uncertainty leads to more precise measurements on important quantities, such as the Higgs mass.

rates. Therefore the uncertainty on measured momentum must be minimized. This is discussed further in Section 6.7.

### 3.3.3. Forward Detectors

There are additional calorimeters in the forward region that deal with high particle flux: two for EM showers, the electromagnetic end-cap calorimeter (EMEC) and the forward calorimeter (FCal), and one for hadronic showers, the hadronic end-cap calorimeter (HEC). All these use liquid argon as the active material, including the HEC as scintillating tiles would degrade in the high particle flux. The absorber material used have shorter radiation lengths and nuclear interaction lengths; lead is used for the EMEC and FCal and copper-tungsten is used in the HEC.

There are two forward detectors that measure luminosity, LUCID (LUminosity measurement using Cerenkov Integrating Detector), ALFA (Absolute Luminosity For ATLAS), and ZDC (Zero-Degree Calorimeter). LUCID detects inelastic p-p scattering in the forward region and is the main luminosity monitor for ATLAS. ALFA

is located  $\pm 240$ m down the beam line and contains fiber trackers inside Roman pots, designed to be as close as 1mm to the beam. ZDC is used with heavy-ion collisions and is located  $\pm 140$ m down the beam pipe, just before the single beam pipe separates into two, and consists of alternating quartz rods and tungsten plates to measure neutral particles to measure centrality of heavy-ion collisions.

### 3.3.4. Muon System

The outermost layer of the detector is the muon spectrometer, which measures the momentum of muons whose path bends in the strong magnetic field from the toroid magnets it is emerged in. The central region,  $|\eta| < 2.7$  has three layers of Monitored Drift Tubes (MDTs), for tracking, and Resistive Plate Chambers (RPCs), for the trigger system. In forward regions, Cathode Strip Chambers (CSCs) are multiwire proportional chambers and can handle high rates and harsh conditions. Thin Gap Chambers (TGCs) are used in the end-cap regions. Muons will usually hit three layers to provide tracking and momentum information. Figure 3.15 shows the ATLAS muon system.

## 3.4. The ATLAS Trigger System

The ATLAS trigger system has the job of reducing the enormous quantity of data collected by the detector and reducing the rate to a reasonable one. The LHC machine has a crossing rate of 40 MHz and data on the order of a kHz can be read out. To do this the trigger uses a hardware trigger (Level 1, or L1) followed by

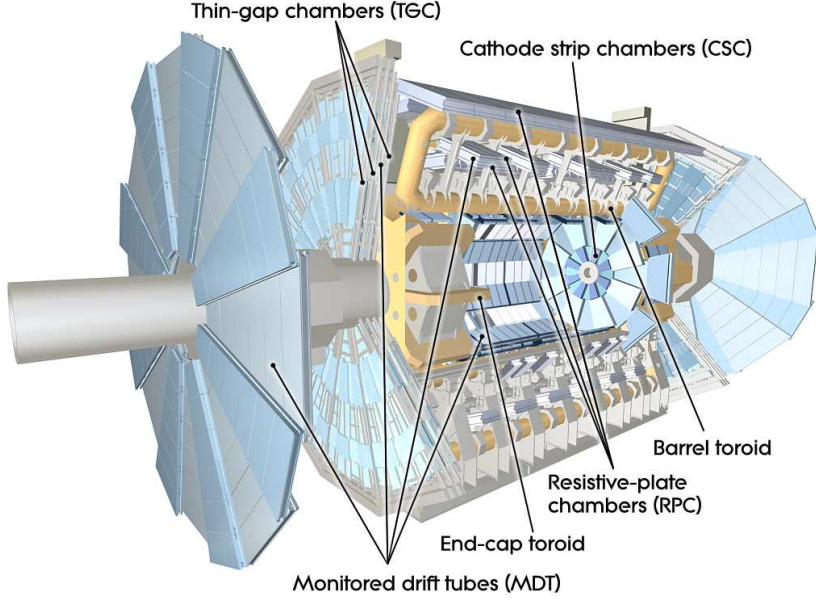


FIGURE 3.15. Cut-away view of ATLAS Muon System (figure from [28]).

software-level triggers (the High Level Trigger, or HLT).

The hardware trigger uses fast algorithms with subsets of detector information to reduce the rate to 100 kHz. The L1Calo trigger uses the calorimeter systems for electrons, photons, hadrons, jets, and  $E_T^{\text{miss}}$ . The L1Muon trigger uses muon information from the muon system. The results from the L1 systems are passed to the central trigger processor, which implements a trigger menu made of combinations of trigger selections. The L1 systems identify regions of interest (RoI) defined by detector geometry and criteria passed, which are passed to the HLT. The decision time is 25  $\mu\text{s}$ .

The Level 2 (L2) trigger, part of the HLT, uses RoIs from the L1 trigger along with full detector granularity to make selections and are designed to reduce the rate

to about 3.5kHz in 40 ms. Finally, the Event Filter reduces the rate to about 1-2 kHz using offline analysis procedures in about 4 seconds.

### 3.5. Calorimeter Trigger Phase I Upgrades

At the end of Run 2 the LHC will have delivered an impressive  $150 \text{ fb}^{-1}$  of data. However, if the LHC continues to run with the same luminosity as in Run 2 the statical gain would be marginal. Therefore, an increase in instantaneous luminosity is planned during Long-Shutdown 2 (LS2), scheduled for the end of 2019 and taking 24 months. During this time the Phase-I upgrade will take place. This includes major upgrades; at the accelerator complex, Linac2 will be replaced by Linac4, which is expected to double the brightness of the beam from the PSB, reducing the beam emittance with smaller  $\beta$  functions. This will increase the luminosity from the current  $1.37 \times 10^{34} \text{ cm}^{-2} \text{s}^{-1}$  to  $2 - 3 \times 10^{34} \text{ cm}^{-2} \text{s}^{-1}$ . During the Run 3 an estimated  $300 \text{ fb}^{-1}$  will be delivered.

The instantaneous luminosity planned for Run 3 corresponds to 55-80 interactions per bunch crossing (pileup) with a 25 ns bunch spacing. Maintaining an optimal trigger system in these conditions requires a trigger electronics upgrade, including improvements in object energy resolution and more advanced algorithms to maintain a high trigger acceptance and rate for L1Calo objects, while also triggering on events with boosted hadronically decaying bosons. The LAr calorimeter will increase in granularity by an order of magnitude to accomplish this.

The current calorimeter trigger information consists of Trigger Towers; during the Phase-I upgrade the granularity will be increased by using Super Cells, which include information from each layer as well as providing finer segmentation within the middle layers as shown in Figure 3.16. The presampler and the last layer will keep the  $\Delta\eta \times \Delta\phi = 0.1 \times 0.1$  geometry while the front and middle layers will increase in granularity to  $\Delta\eta \times \Delta\phi = 0.025 \times 0.1$ . This means an increase in granularity by a factor of 10 depending on the part of the barrel and improves energy resolution and efficiency for selecting electrons, photons,  $\tau$  leptons, jets, and  $E_T^{\text{miss}}$  while also improving discrimination against backgrounds and fakes in high pileup conditions.

Additionally, new LAr Trigger Digitizer Boards (LTDB) will be installed on the Front-End crates. These will both digitize high-granularity information from the calorimeters and also create analog sums to maintain a functional legacy system.

After digitization the LTDB transfers calorimeter signals to the LATOME (LAr Trigger prOcessing MEzzanine) cards in the off-detector LAr Digital Processing System (LDPS), each of which uses a filtering algorithm on an FPGA to reconstruct the transverse energy of the Super Cells every 25 ns and identifies the related bunch-crossing (BCID). The LATOME then transmits information to the new feature extraction processors (FEXs) that will implement sophisticated object identification algorithms. These include the eFEX (electron), jFEX (jet), and gFEX (global). The eFEX receives full super cell information, and the jFEX receives  $\Delta\eta \times \Delta\phi = 0.1 \times 0.1$  super cell energy sums. Figure 4.1 shows the updated L1Calo system.

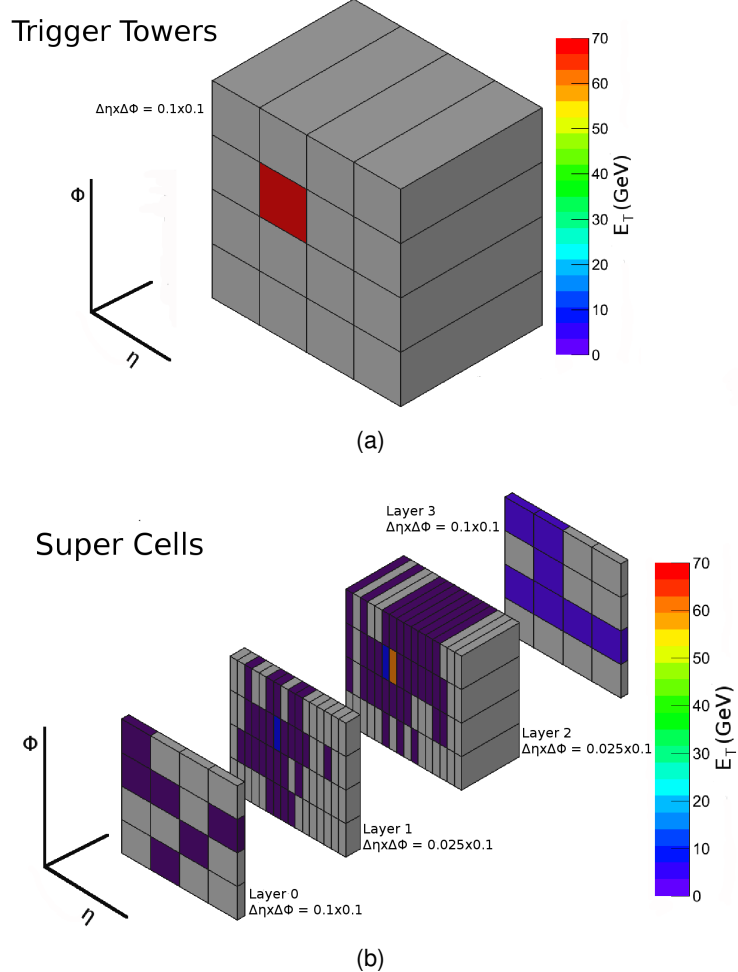


FIGURE 3.16. A sample event of a 70 GeV electron as seen by the current L1Calo Trigger, with all cells summed into a Trigger Tower (a) and after the Phase I upgrade with Super Cells (b) (figure from [33]).

In addition to the eFEX and jFEX, the gFEX is new and unique in the fact that it can scan the entire calorimeter with a single module and thus use full-scan algorithms and trigger on boosted topologies. In order to accommodate the calorimeter on one board the granularity is reduced so the gFEX receives  $\Delta\eta \times \Delta\phi = 0.2 \times 0.2$  super cell energy sums, called gTowers. gTowers can be summed into  $3 \times 3$  contiguous towers to form gBlocks also and summed into  $R=1.0$  jets called gJets. Large  $R$  jets are typical

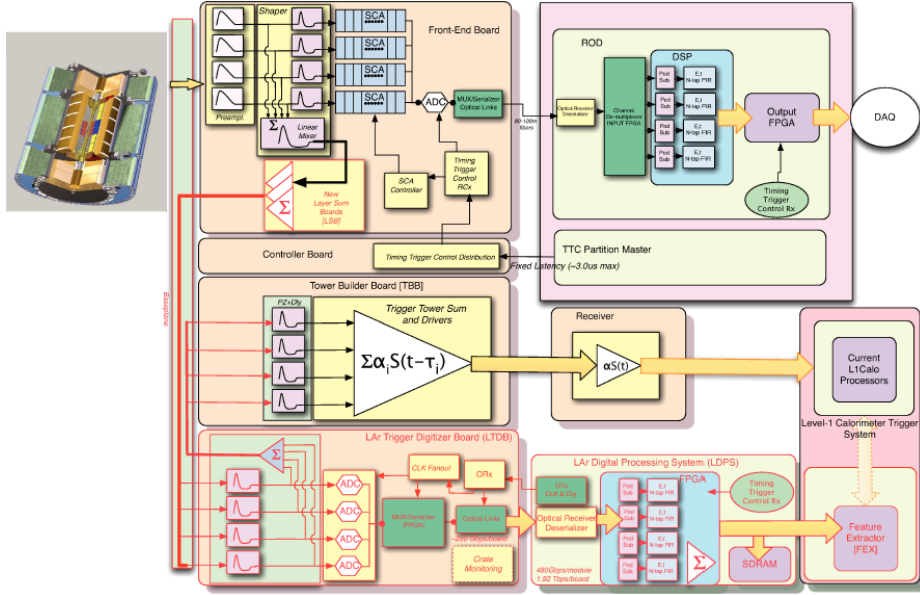


FIGURE 3.17. Schematic diagram of the LAr trigger readout architecture after the Phase I upgrade with new components indicated by red outlines and arrows (figure from [33]).

of boosted objects, which can be the results of interesting physics processes, and the gFEX will provide the capability to trigger on them and also study their substructure. Additionally, since the entire calorimeter is on one board it can calculate  $E_T^{\text{miss}}$  as well. The gFEX will be discussed more in the Chapter IV.

The Phase-I upgrade also includes consolidation of the existing sub-detectors and an installation of the New Small Wheel (NSW) and additional chambers in the muon spectrometer to improve geometrical coverage, and additional neutron shielding for the muon endcap toroids.

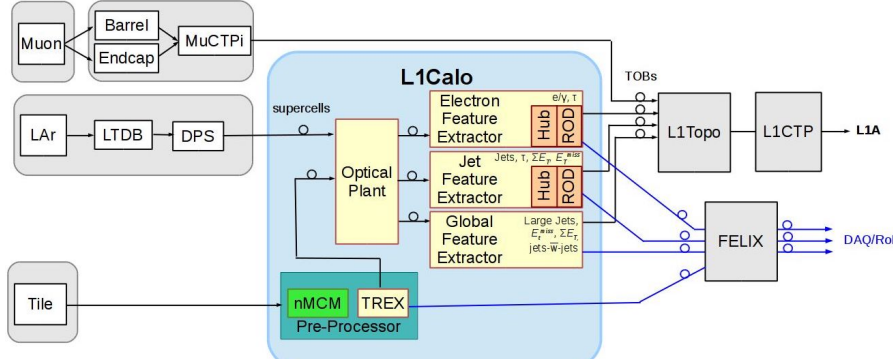


FIGURE 3.18. L1Calo system after the Phase I upgrade with new elements including the FEXs (figure from [34]).

### 3.6. Calorimeter Trigger Phase II Upgrades

After Run 3 a longer shutdown, LS3, is planned to upgrade the LHC to the High Luminosity LHC (HL-LHC)[35]. This upgrade, the Phase II upgrade is scheduled for 2024-2026 and will upgrade various detector systems to handle the increase in luminosity. The HL-LHC will see an increase in peak luminosity during Run 4 of up to  $5 \times 10^{34} \text{ cm}^{-2}\text{s}^{-1}$  in order to deliver  $250 \text{ fb}^{-1}$  per year, or  $3000 \text{ fb}^{-1}$  (possible as high as  $4000 \text{ fb}^{-1}$ ) by the end of Run 4. This enormous quantity of data will allow for precision measurements of the Higgs boson with all production processes and decay modes, improved SM measurements, and beyond the SM searches. This will also increase pileup to  $\sim 200$ .

The following upgrades are scheduled in order to support the physics goals of the HL-LHC:

- Inner Tracker: New strip and pixel detectors with an increase in acceptance up to  $|\eta| = 4.0$ .

- Calorimeters: The readout electronics for the LAr and Tile calorimeters will be upgraded to accommodate the radiation tolerance and to allow the front-end electronics to operate under the trigger rates and latencies needed for the increased luminosity. The LAr Signal Processor (LASP) will provide the ability to run more sophisticated algorithms to suppress pileup and improve cell resolution.
- Muon Spectrometer: An upgrade to the L0 trigger electronics of the RPC and TGC chambers will improve the performance of the muon trigger chambers, and new RPC detectors will increase coverage to  $|\eta| < 1$ . The MDT front-end readout will also be replaced to improve muon resolution.
- TDAQ: There are three main upgrades to the TDAQ system:
  - \* Level-0 (L0) Trigger: In addition to the Phase I FEXs, there will be the addition of the forward Feature EXtractor (fFEX) to reconstruct forward jets and electrons. The global trigger will be added to extend the functionalities and resources' limits for the FEXs, especially by implementing algorithms to refine calculations, apply tighter isolation criteria, and integrate topological functionality of  $\Delta R$  between objects.
  - \* Data Acquisition: Results from the L0 trigger decision is transmitted to all detectors with a readout rate of 1 MHz.
  - \* Event Filter (EF): The EF system uses a CPU-based processing farm, assisted by a Hardware-based Tracking for the Trigger (HTT) system, to select events with a maximum rate of 10 kHz to save to permanent storage.

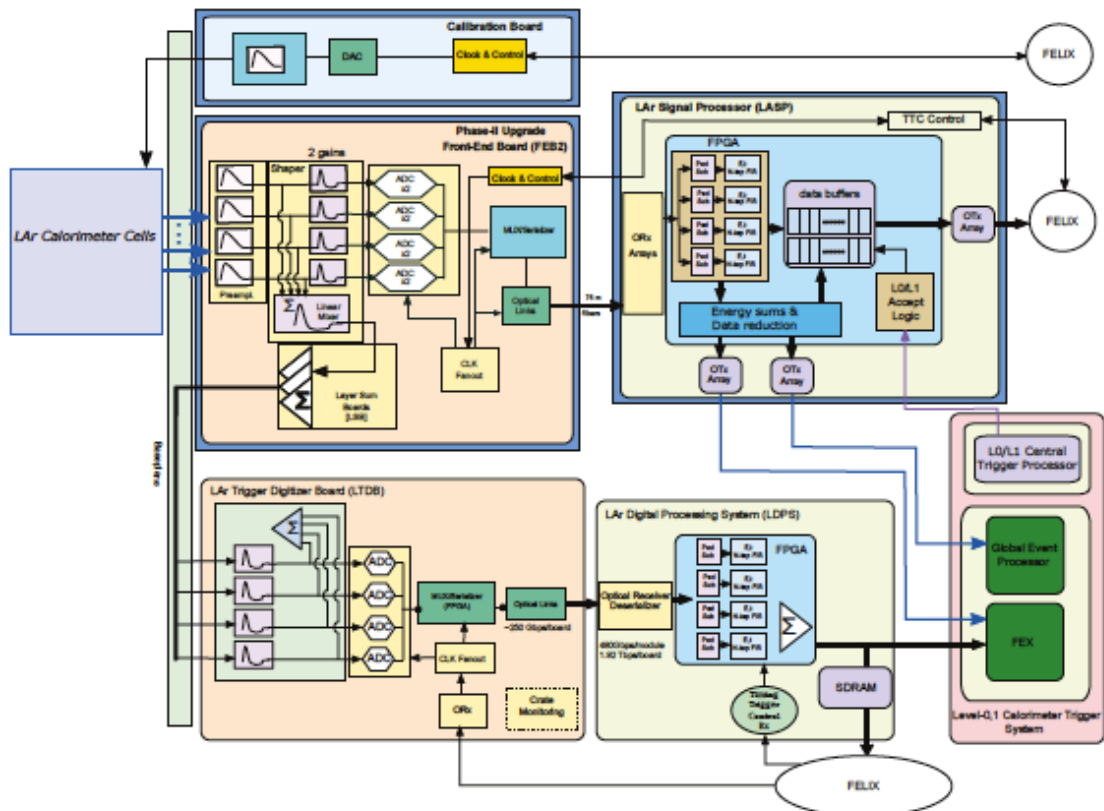


FIGURE 3.19. Schematic diagram of the LAr trigger readout architecture after the Phase II upgrade (figure from [36]).

## CHAPTER IV

### OVERVIEW OF THE GLOBAL FEATURE EXTRACTOR

This chapter gives more details about the gFEX upgrade to the ATLAS trigger and the calibration scheme developed for it.

#### 4.1. Global Feature Extractor Phase I Upgrade

The Phase I upgrade to the ATLAS detector will be performed during Long Shutdown 2, scheduled for 2019-2020. This is in preparation of Run 3, which will see a maximum instantaneous luminosity of  $2\text{-}3 \times 10^{34}\text{cm}^{-2}\text{s}^{-1}$  and 55-80 interactions per bunch crossing with 25ns spacing. The trigger electronics must be upgraded to maintain an optimal trigger system. This includes improvement in object energy resolution and more advanced algorithms to maintain trigger acceptance and rate. The Liquid Argon (LAr) calorimeter will also be upgraded to have an increase in granularity of an order of magnitude. This will be done by implementing super cells, as shown in Figure 3.16, which increase the granularity in the front and middle layers from  $(\Delta\eta \times \Delta\phi) = (0.1 \times 0.1)$  to  $(0.025 \times 0.1)$ . New modules in the trigger system, Feature EXtractors (FEXs) will use this increased granularity for object identification algorithms.

For transmitting this information to the FEXs, LAr Trigger Digitizer Boards (LTDBs) will be installed in available slots of the LAr front-end crates. These digitize and transmit calorimeter signals to the LAr Trigger prOcessing MEzzanine (LATOME) cards in the off-detector LAr Digital Processing System (LDPS). A Field Programmable Gate Array (FPGA) chip on the LATOME reconstructs the transverse

energy of each super cell and the bunch-crossing identification (BCID). The LATOME then transmits the super cell information to the FEXs in appropriate granularities; full granularity to the electron Feature EXtractor (eFEX),  $(\Delta\eta \times \Delta\phi) = (0.1 \times 0.1)$  to the jet Feature EXtractor (jFEX),  $(\Delta\eta \times \Delta\phi) = (0.2 \times 0.2)$  to the global Feature EXtractor (gFEX). The LDPS processes, buffers, and transmits data to the ATLAS Trigger and Data Acquisition System (TDAQ) readout chain and monitoring processes to Level 1 Trigger Acceptance (L1A). After L1A data from the FEXs and LDPS are routed to the Front End Link EXchange (FELIX) which interfaces sub-detectors with data acquisition. The LDPS also recreates analog sums with the current granularity and sends the information to the current systems for commissioning of the new systems.

The L1Calo system after Phase I is shown in Figure 4.1.

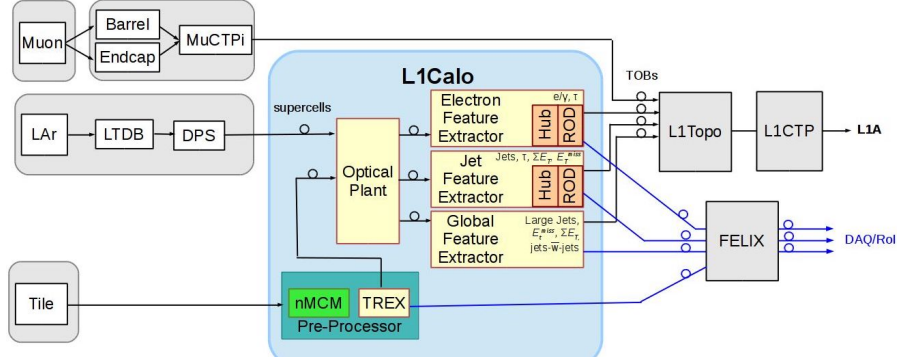


FIGURE 4.1. L1Calo system after the Phase I upgrade with new elements including the FEXs (figure from [34]).

While the eFEX and jFEX will provide improved but similar functionality as the CPMs and JEMs, the gFEX is a new technological addition. Unlike any other part of the trigger system the gFEX will have the entire calorimeter available on a single module and so can scan the full  $\eta$  range of the calorimeter. This allows the gFEX to trigger on large-radius jets, typical of Lorentz-boosted objects, as well as calculate

missing energy,  $E_T^{\text{miss}}$ , and centrality-related variables for heavy ion events.

In order to scan the entire calorimeter, the gFEX will use three Virtex Ultrascale+ processor FPGAs (pFPGA) to run algorithms and one hybrid Zynq Ultrascale+ FPGA (zFPGA) for control and readout[34]. The central region of the calorimeter is split between two pFPGAs and the forward regions one the third pFPGA, but pFPGAs will be able to communicate with each other.

The input data from the calorimeters are organized into gTowers, which are summed electromagnetic and hadronic towers typically  $(\Delta\eta \times \Delta\phi) = (0.2 \times 0.2)$  in size. Groups of gTowers, called gBlocks, are constructed with a sliding window algorithm and are usually  $3 \times 3$  gTowers, with  $(\Delta\eta \times \Delta\phi) = (0.6 \times 0.6)$ . These are used to seed large-radius jets and determining jet substructure, as well as for calibration. Large-radius ( $R=1.0$ ) jets constructed from gTowers, gJets, are constructed with a simple-cone jet algorithm seeded by gBlocks. gBlocks and gJets are permitted to overlap. The layout of the gFEX, showing the gTowers in a black grid, colored rectangular gBlocks, and lighter colored round gJets are shown in Figure 4.2.

Boosted hadronic topologies are characteristics in many new physics scenarios as the decay products of high momenta boson and top quark decay products are highly energetic and are usually very collimated. Because of this they can merge into a large radius jet which can be detected by the gFEX. The current trigger system, which looks at relatively small regions of interest, may not trigger on these sort of objects.

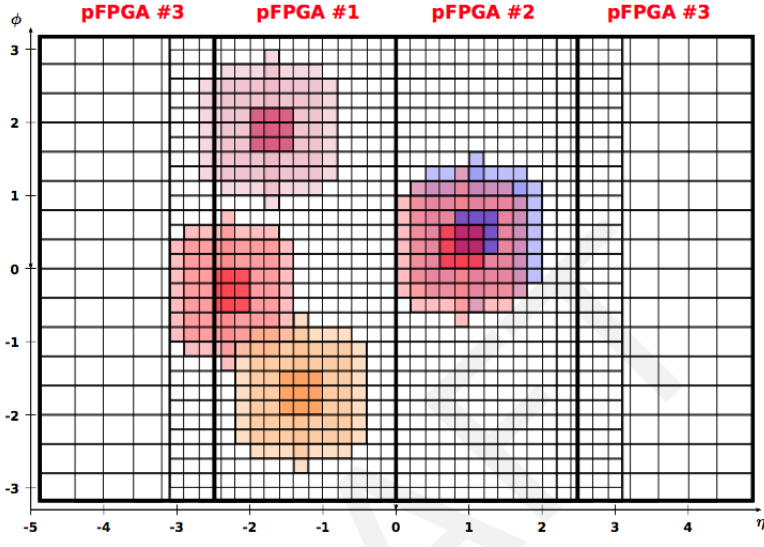


FIGURE 4.2. Layout of the gFEX. The black squares are gTowers, groups of gTowers are gBlocks, and circular groups of gTowers are gJets, seeded by gBlocks. Note that gBlocks and gTowers can overlap (figure from [34]).

Most interactions in a bunch crossing are not hard-scatter events that can create interesting physics events, but are soft collisions that are not of interest to physics searches. The number of interactions per bunch crossing will increase after the Phase I and Phase II upgrades as the luminosity in the LHC increases. Pileup increases the uncertainty of energy of a jet, worsening the jet energy resolution (JER). As the uncertainty of the energy of a jet increases, the likelihood of fake missing energy increases. This increases the rate of the missing energy trigger, so the threshold must be increased to accommodate this.

Momentum imbalances are also signatures of many new physics scenarios that predict stable invisible particles, such as supersymmetry and dark matter. Since the missing energy trigger is also very sensitive to pileup, and as the missing energy trigger is often the most efficient trigger to use in searches for new physics, reducing

pileup effects in the gFEX is very important.

In addition to improving the JER and reducing pileup effects, the gFEX must also be calibrated to determine the jet energy scale (JES). In the case of dijet events, the gBlock area covers  $\geq 90\%$  of an anti- $k_t$  R=0.4 jet. Therefore truth R=0.4 jets can be used to calibrate gBlocks and the JES constant the ratio of  $R = \frac{E_T^{gBlock}}{E_T^{truth}}$  (not to be confused with the jet radius parameter R). With enough statistics the distribution of the ratio can be built with the JES equal to the mean of the distribution and the JER equal to the RMS of the distribution. A lookup table (LUT) with correction factors as function of energy and  $\eta$  can be constructed and implemented in the gFEX firmware. This calibration is performed using the official JetETmiss calibration software with a few modifications described below.

## 4.2. Pileup Suppression

The small energy deviations in a gTower are mostly due to electronic and pileup noise and since the average pileup over all events is 0 if the proper OFCs are applied, a noise cut on the gTowers is applied as a function of the standard deviation of the noise (a pileup distribution is shown in Figure 4.3); all gTowers whose absolute energy is less than the noise cut have their energy set to zero.

After this noise cut the JES is determined similarly to typical approach with the exception that in addition to matching to a truth jet a gTower must also match to an offline jet as that is what is reconstructed offline.

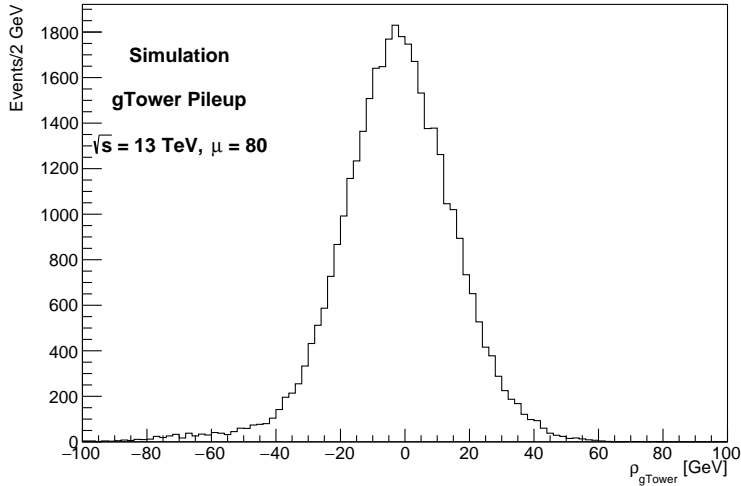


FIGURE 4.3. Distribution of pileup (energy density per unit area) across all events with  $\langle \mu \rangle = 80$  for dijet events (JZ0W) with  $\sqrt{s} = 13$  TeV. The distribution is centered around 0 with proper OFCs. The standard deviation of this distribution is 18.22 GeV/area, so a  $1\sigma$  noise cut is  $18.22 \times (0.2 \times 0.2) = 0.73$  GeV, or 2.92 GeV for a  $4\sigma$  noise cut (3 GeV used).

### 4.3. Calibration

The JetETmiss software is designed to match truth jets to reconstructed HLT jets and determine the JES by the mean of the distribution of the ratio  $R = \frac{E_T^{gBlock}}{E_T^{truth}}$  in bins of energy and  $\eta$ . The values of the JES are checked by calculating the closure.

A noise cut of  $4\sigma$  on the energy is shown, though other choices may be optimal for other pileup conditions. After making this noise cut on the gTowers they are binned as  $E_{true} \times \frac{E_{gTower,central}}{E_{gBlock}}$  since most of the energy of a dijet lies in the central gTower. Figure 4.6 shows the energy response of a slice in  $\eta$  and  $p_T$ .

This response is repeated over all  $\eta$  and  $p_T$  to obtain a complete set of calibration constants. Figure 4.5 shows the response over the calorimeters with various values of

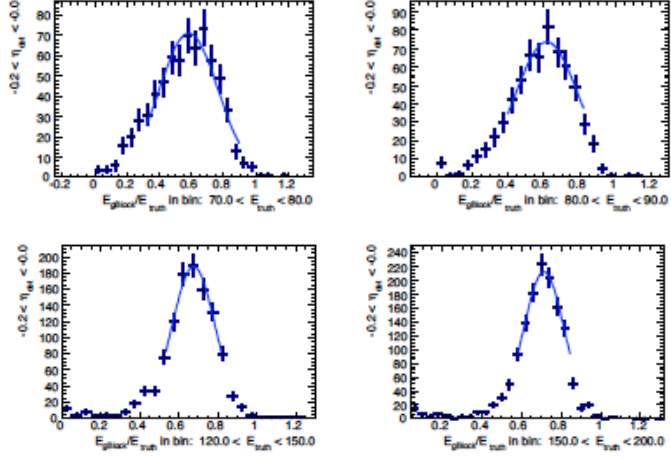


FIGURE 4.4. Energy response of gTowers after a  $4\sigma$  noise cut prior to calibration for a slice in  $\eta$  and various  $p_T$  slices. The mean of the gaussian fit gives the JES used for calibration and the RMS of the fit gives the JER.

$p_T$ .

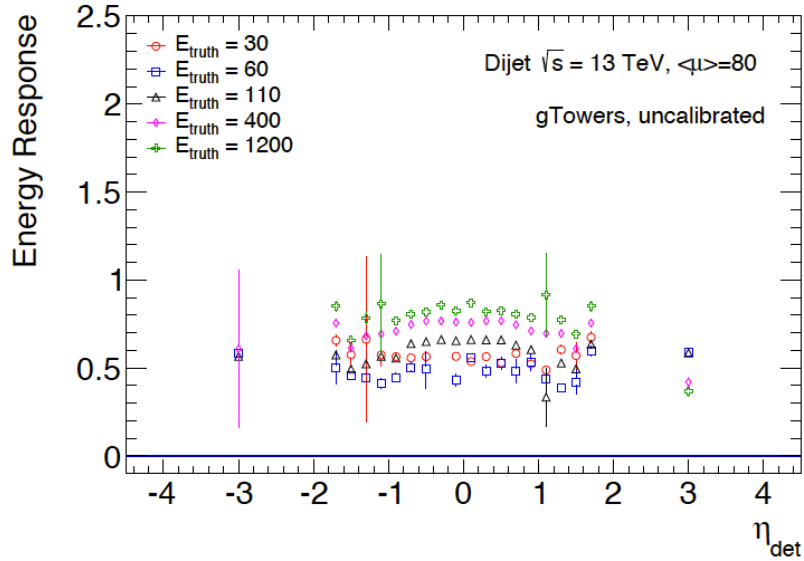


FIGURE 4.5. Energy response of the gTowers after a noise cut as a function of  $\eta$  for various energies of truth jets.

After determining and applying the calibration to the gTowers, the gBlocks are constructed from the calibrated gTowers. Figure 4.6 shows the energy response of

the gBlocks compared to truth jets after this calibration. If the calibration is perfect then one would expect a straight line at 1.0. For higher  $p_T$  truth jets this is close to the result. Lower  $p_T$  truth jets have a worse response, but this is to be expected as a sampling calorimeter only detects a fraction of the energy of a jet and low  $p_T$  jets are generally hard to calibrate. This is a hardware trigger, so perfect calibration isn't necessary.

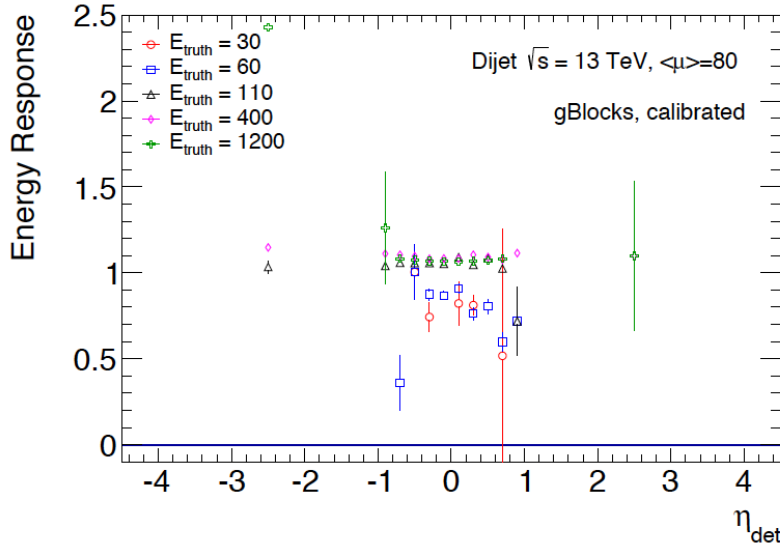


FIGURE 4.6. Energy response of gBlocks after being constructed from calibrated gTowers over  $\eta$  for several values of  $p_T$ .

#### 4.4. Effects of Calibration on $p_T$ and $E_{\text{T}}^{\text{miss}}$

The distribution of the leading gBlock  $p_T$  both without any noise cuts or calibration and with a  $4\sigma$  noise cut and calibration are shown in Figure 4.7. The primary purpose is to check that the distributions are as expected and that the noise cut and calibration does not alter the distribution in a physically unrealistic way.

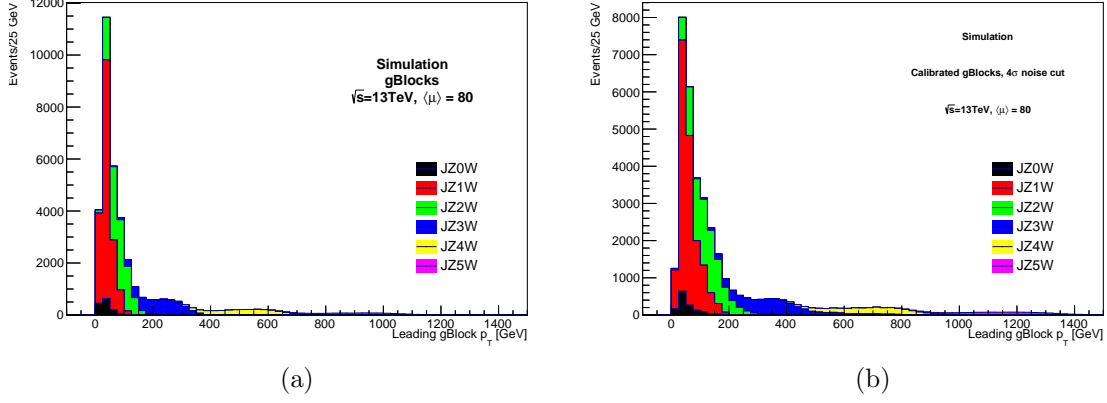


FIGURE 4.7. Distributions of leading gBlock  $p_T$  (a) prior to a noise cut and calibration and (b) after a noise cut of  $4\sigma$  and calibration. The stacked histograms show the breakdown of JZW slices. The primary purpose of this distribution is a check on the distributions.

The  $E_T^{\text{miss}}$  distributions, broken down in the  $x$  and  $y$  directions to show any bias in the calorimeter or calibration, calculated from gTowers before and after a noise cut and calibration are shown in Figure 4.8. As this is a dijet sample no real  $E_T^{\text{miss}}$  is expected, so ideally the distributions would have a single peak at 0, but this is not the case due to jet energy resolution uncertainty.

#### 4.5. Trigger Efficiencies and Rate

The turn-on curve represents the efficiency of the trigger and the steepness of the plot demonstrates the resolution for a jet at a certain energy. After a  $4\sigma$  noise cut, the turn-ons for a calibrated (120 GeV) and uncalibrated (85 GeV) gBlocks in the central region are shown in Figure 4.9. The efficiency curve is constructed by determining if the leading truth jet is in the central region of the calorimeter. If it is then the  $p_T$  is added to a “denominator” histogram. Then, if the leading gBlock is also located in

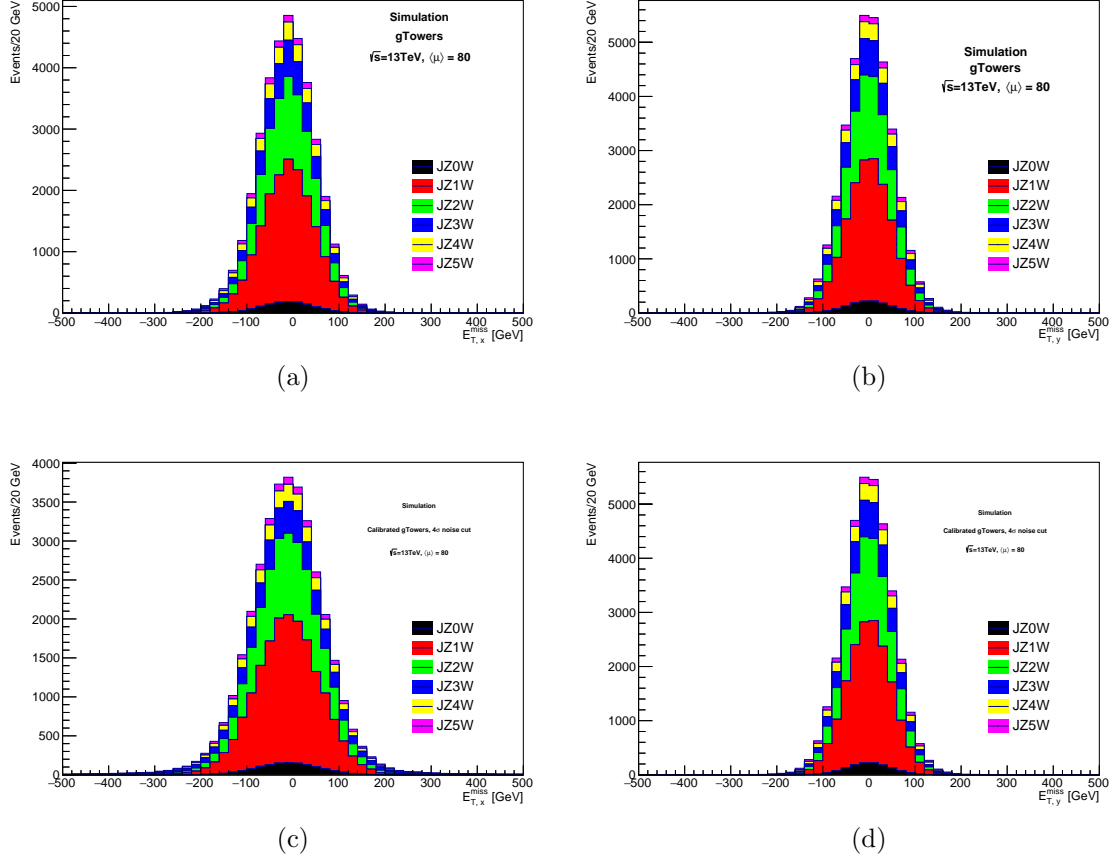


FIGURE 4.8. Distributions of  $E_{T}^{\text{miss}}$  calculated from gTowers before calibration in the (a) $x$  direction and (b) $y$  direction and after a noise cut of  $4\sigma$  and calibration in the (c) $x$  direction and (d) $y$  direction. The stacked histograms show the breakdown of JZW slices. As this is a dijet sample no real  $E_{T}^{\text{miss}}$  is expected.

the central region of the calorimeter and if its  $p_{\text{T}}$  passes a cut (e.g. 120 GeV) then the leading truth jet  $p_{\text{T}}$  is added to a ‘‘numerator’’ histogram. After all events are checked in a sample the numerator histogram is divided by the denominator histogram. This shows the likelihood of a truth jet  $p_{\text{T}}$  passing the gBlock trigger.

The rate plot helps determine the jet energy that can be triggered on, since there is limited bandwidth. In order to compare calibrated and uncalibrated  $p_{\text{TS}}$ ,

the uncalibrated gBlocks were scaled by a factor of  $\frac{1}{0.6}$  to approximate a calibration constant. The rate is shown in Figure 4.10.

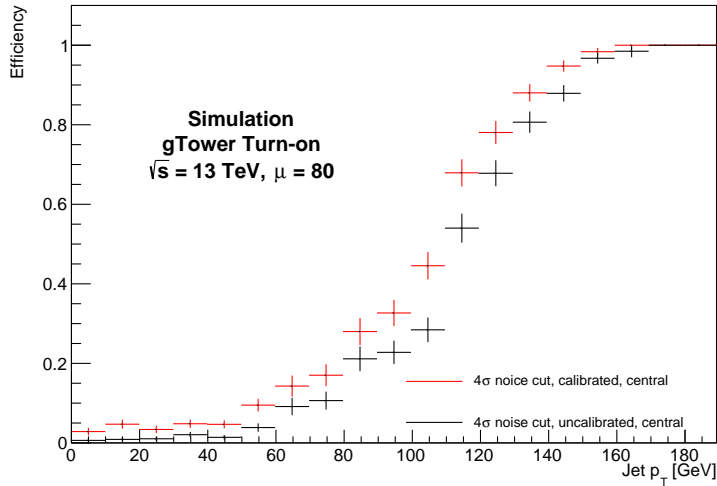


FIGURE 4.9. Trigger efficiency for a calibrated gBlock threshold of  $p_T = 120$  GeV and uncalibrated threshold of 85 GeV for the central region,  $|\eta| < 0.5$ , with a noise cut of  $4\sigma$  for  $\langle \mu \rangle = 80$  for dijet events (JZ0W-JZ5W) with  $\sqrt{s} = 13$  TeV.

## 4.6. Outlook

A new pileup suppression and calibration scheme was presented here for the gFEX upgrade to the ATLAS trigger system. Further studies are still needed, such as optimizing the noise cut value and studies with the Phase II levels of pileup, but the scheme looks promising for the future.

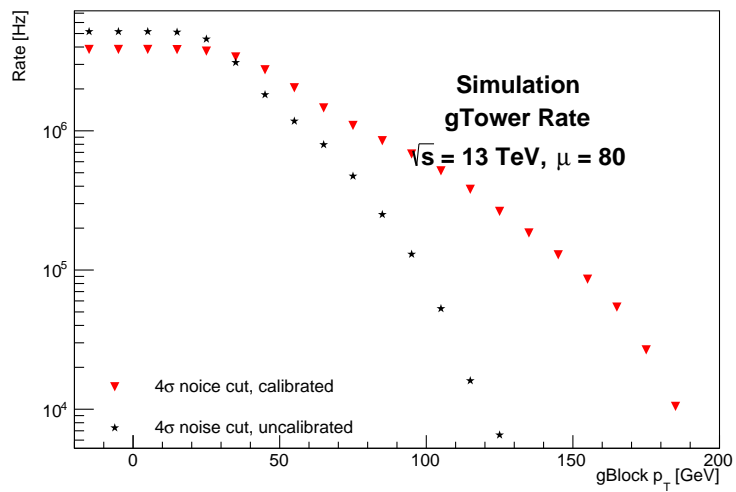


FIGURE 4.10. Trigger rates for a range of gBlock  $p_T$  with a noise cut of  $4\sigma$  with and without calibration with  $\langle \mu \rangle = 80$  for dijet events (JZ0W and JZ1W) with  $\sqrt{s} = 13$  TeV.

## CHAPTER V

### ANALYSIS OVERVIEW

This chapter provides an overview of the analysis described in Chapter VII and published in 2017 in *JHEP*[1]. This chapter contains material coauthored with the ATLAS Collaboration. I was the primary contributor to the  $t\bar{t}$  background estimation. Other members of the analysis group, part of the ATLAS Collaboration, estimated other backgrounds, and the background estimates were used by the analysis group to produce the results, including exclusion plots. As described in Chapter II, the search for the stop is well-motivated since the stop should be lighter than other squarks. As it has the highest impact on naturalness, and could be the lightest squark, the stop is an important particle for which to perform a search. Additionally, the lightest supersymmetric particle, e.g. the neutralino, is a viable dark matter candidate and is produced in conjunction with the stop in  $R$ -parity conserving SUSY models. This dissertation describes a search for **direct** stop pair production (in contrast to top squarks produced through gluino cascade decays). Figure 5.1 shows the direct production cross section of the stop quark as a function of its mass with several SM processes shown for comparison.

Three different decay scenarios are considered in this search: (a) both top squarks decay via  $\tilde{t}_1 \rightarrow t^{(*)}\tilde{\chi}_1^0$ , (b) at least one of the top squarks decays via  $\tilde{t}_1 \rightarrow b\tilde{\chi}_1^\pm \rightarrow bW^{(*)}\tilde{\chi}_1^0$ , with various hypotheses for  $m_{\tilde{\chi}_1^0}$  and  $m_{\tilde{\chi}_1^\pm}$ , and (c) where  $m_{\tilde{\chi}_2^0}$  is small enough for at least one top squark to decay via  $\tilde{t}_1 \rightarrow t\tilde{\chi}_2^0 \rightarrow h/Z\tilde{\chi}_1^0$ , where  $h$  is the SM-like Higgs boson with a mass of 125 GeV, as illustrated in Figure 5.2(a)–(c), respectively. In addition to direct pair production, top squarks can be produced

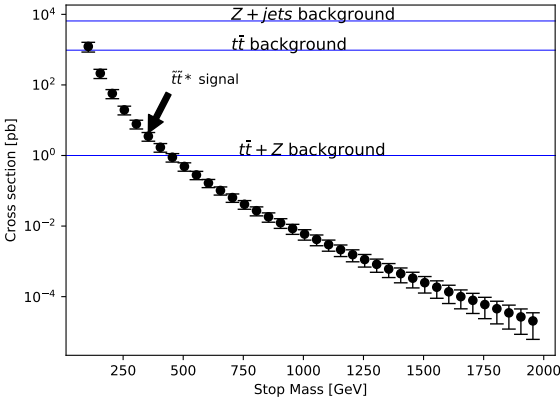


FIGURE 5.1. Cross section for direct stop pair production as a function of stop mass at a center-of-mass energy of 13 TeV. Several SM cross sections,  $t\bar{t}$ ,  $Z + \text{jets}$ [37], and  $t\bar{t} + Z$ [37], are shown as well for reference. Note that for heavier stop quarks SM processes have cross sections that are orders of magnitude larger.

indirectly through gluino decays, as shown in Figure 5.2(d). In all cases, the all-hadronic decay of the top quark (or of the W in the  $b + W^{(*)} + \tilde{\chi}_1^0$  mode) is considered. Orthogonal searches also exist that focus on the lepton+jets[38] and dilepton[39] decay modes of the top quark.

The all-hadronic top decay mode nominally has six jets in the final state, but events with at least four reconstructed jets are considered. However, this channel has the feature that there are no neutrinos in the final state, so the only intrinsic  $E_T^{\text{miss}}$  is from the  $\tilde{\chi}_1^0$ s except possibly from semi-leptonic  $b$  decays. Therefore the experimental signature is multiple jets and high  $E_T^{\text{miss}}$ .

A common feature of all analyses studying a specific phenomenon is defining a region of phase space designed to have a significant excess of signal events compared to background events. This is done by applying selections to sets of kinematic observables and is called a signal region (SR). Several signal regions have been

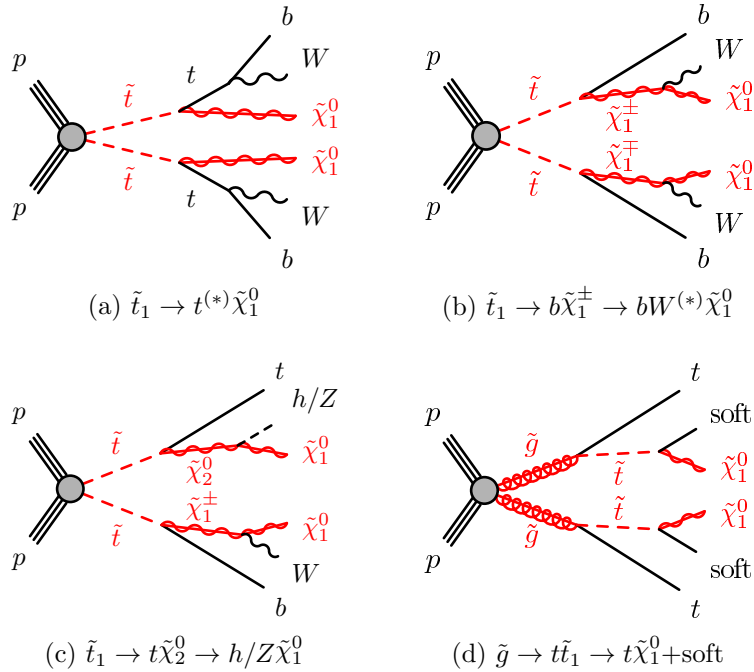


FIGURE 5.2. The decay topologies of the signal models considered with experimental signatures of four or more jets plus missing transverse momentum. Decay products that have transverse momenta below detector thresholds are designated by the term “soft”.

developed to optimize sensitivity to different stop-neutralino mass combinations, as illustrated in Figure 5.3, and different final states, as illustrated in Figure 5.2.

More details on the SRs are presented in Section 7.1. Signal regions A (SRA) and B (SRB) are optimized for high stop masses in the decay channel shown in Figure 5.2(a). SRA is optimized to be sensitive to decays of heavy stops into a top quark and a light  $\tilde{\chi}_1^0$ . Events are divided into three categories based on the reconstructed top candidate mass (nominally 175 GeV), which was not done in the Run 1 analysis[40]. The Run 1 analysis was performed on  $20.1 \text{ fb}^{-1}$  at a center-of-mass energy of 8 TeV. The TT category includes events with two well-reconstructed

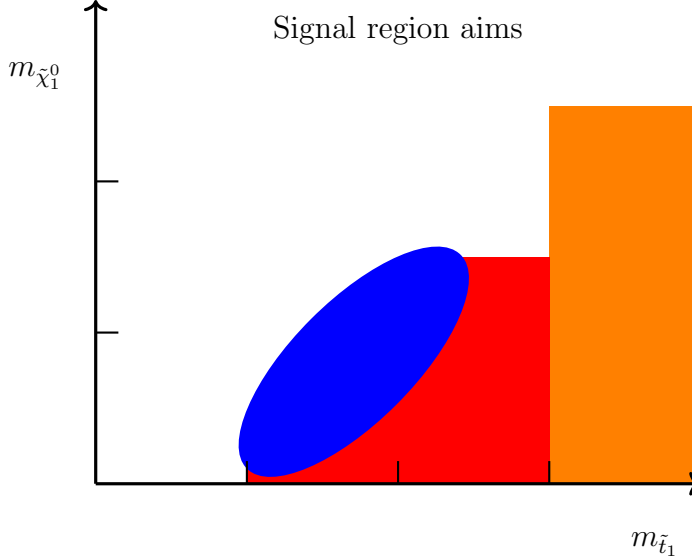


FIGURE 5.3. Multiple signal regions have been developed to increase sensitivity in different stop and neutralino mass combinations: SRC in blue, SRB in red, and SRA in orange.

top candidates, the TW category contains events with a well-reconstructed leading  $p_T$  top candidate and a well-reconstructed subleading  $W$  candidate (from the subleading  $R = 1.2$  reclustered mass), and the T0 category represents events with only a leading top candidate. This is shown in Figure 5.4, where the horizontal axis is the mass of the leading  $R = 1.2$  reclustered mass and the vertical axis is that of the second-leading  $R = 1.2$  reclustered mass. Optimizing the significance<sup>1</sup> in the categories showed an improvement in discovery significance compared to the combined optimization.

In SRC the signature of stop decays when  $\Delta m(\tilde{t}_1, \tilde{\chi}_1^0) \sim m_t$  is significantly softer with low  $E_T^{\text{miss}}$  for the decay channel shown in Figure 5.2(a). This decay topology is very similar to non-resonant  $t\bar{t}$  production making signal and background separation challenging. However, several kinematic properties can be exploited to separate stop

---

<sup>1</sup> Significance is defined as  $\frac{S}{\sqrt{B}}$  where  $S$  is the number of signal events and  $B$  is the number of background events

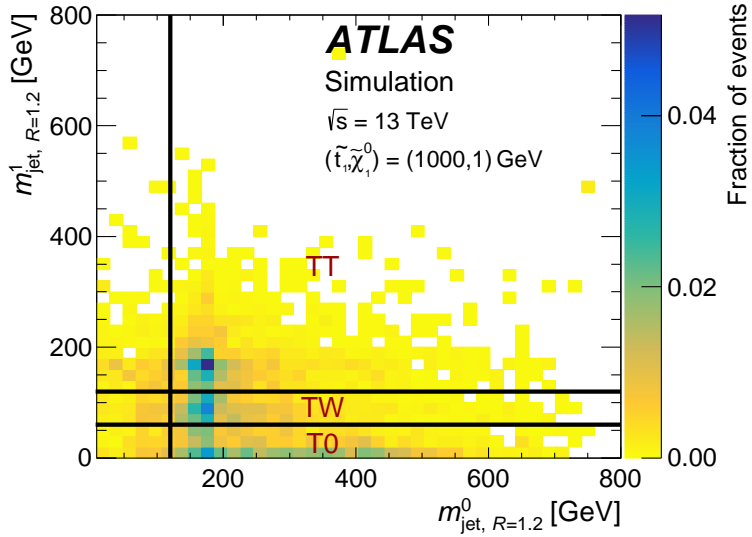


FIGURE 5.4. Illustration of signal-region categories (TT, TW, and T0) based on the  $R = 1.2$  reclustered top-candidate masses for simulated direct top-squark pair production with  $(m_{\tilde{t}_1}, m_{\tilde{\chi}_1^0}) = (1000, 1)$  GeV after the loose preselection requirement described in the text. The black lines represent the requirements on the reclustered jet masses.

decays from  $t\bar{t}$  when an ISR jet is present in the final state. These variables are described in Section 7.1.2.

The selections for SRD are optimized for the decay of both pair-produced top squarks into a  $b$  quark and a  $\tilde{\chi}_1^\pm$  as shown in Figure 5.2(b). SRE is designed for a model for which the tops are highly boosted. Such signatures can either come from direct stop pair production with a very high stop mass, or in the gluino-mediated compressed-stop scenario with large  $m_{\tilde{g}} - m_{\tilde{t}_1}$  as shown in Figure 5.2(d).

Background processes that contaminate SRs must also be estimated. Control regions (CRs) are designed for each dominant background to be pure in that background and have as little signal contamination as possible. Appendix B shows the

signal contamination in each of the CRs and VRs. These are compared to data and therefore must be orthogonal to the SRs, but still as close as possible kinematically in order to reduce uncertainties when extrapolating. The CRs are defined for the major backgrounds in each SR to normalize the simulation to data and ensure the shapes of the simulated backgrounds match those of the data. However, enough data is required in order to minimize the uncertainties in the normalization factors.

The dominant background sources are:

- $Z \rightarrow \nu\bar{\nu}$  plus additional  $b$ -jets, typically produced in a Drell-Yan process.
- Semileptonic  $t\bar{t}$  events, which contain  $W \rightarrow e/\mu/\tau\nu$  decays where the lepton is either lost or mis-identified as a jet (and have high  $E_T^{\text{miss}}$  due to the escaping neutrino).
- $W \rightarrow \ell\bar{\nu}$  plus additional  $b$ -jets,
- $t\bar{t} + Z$ , where both tops decay hadronically and  $Z \rightarrow \nu\bar{\nu}$ , and
- $Wt$ -channel single top decays, where one  $W$  decays hadronically and one leptonically.

Figure 5.5 summarizes theory predictions and ATLAS measurements for various SM production cross-sections and shows both total and fiducial cross sections<sup>2</sup>.

It can be seen in Figure 5.6, which shows the backgrounds in SRB, that  $Z \rightarrow \nu\bar{\nu}$  and  $t\bar{t}$  are major contributors to the background processes.

---

<sup>2</sup> A fiducial cross section is a cross section for the subset of a process which is visible in the detector.

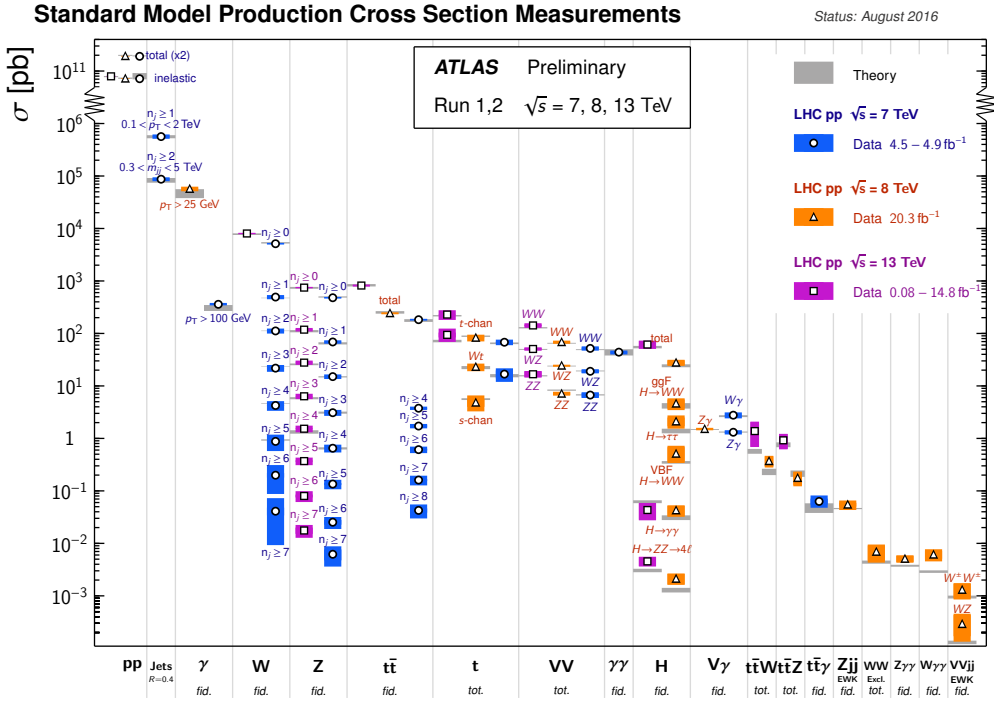


FIGURE 5.5. Summary of several SM total and fiducial production cross section measurements compared to the corresponding theoretical expectations[41].

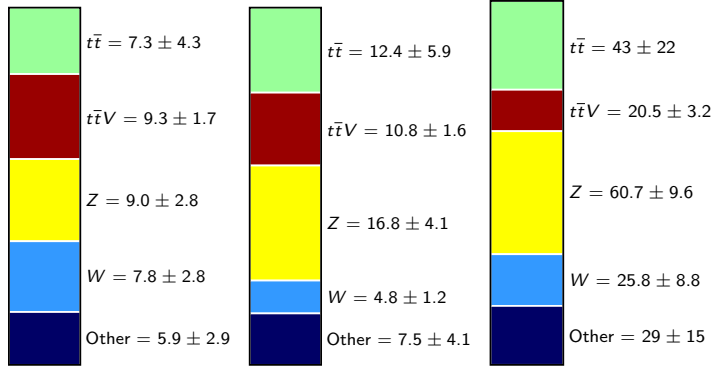


FIGURE 5.6. Breakdown of the backgrounds in SRB-TT, -TW, and -T0 from left to right.

The strategy for the CRs are:

- 1-lepton: Requires exactly one well-identified lepton in order to be orthogonal to the SRs and treat it as a jet. This CR is used for leptonically-decaying  $W$  bosons, as in the  $t\bar{t}$ ,  $W$ +jets, and single top backgrounds. The CRs are orthogonal to 1-lepton searches.
- 2-lepton: Requires exactly two well-defined leptons in order to be orthogonal to the SRs. This is used to model  $Z \rightarrow \nu\bar{\nu}$  events, so the invariant mass of the leptons must be that of the  $Z$  boson. These leptons are thus treated as invisible particles and their  $p_T$  added to the  $E_T^{\text{miss}}$ .
- The  $t\bar{t} + Z$  background uses a photon to model the  $Z$   $p_T$ .
- The QCD multijet background occurs when jets are mis-modeled to produce fake  $E_T^{\text{miss}}$ . To estimate this background jet smearing[42] is used, where the  $p_T$  and jet response function of well-measured jets with low  $E_T^{\text{miss}}$  in data are smeared to simulate jet mis-modeling.

More details on the CRs are shown in Section 7.2. The observed numbers of events in the various control regions are included in a binned profile likelihood fit[43] to determine the SM background estimates for  $Z$ ,  $t\bar{t}$ ,  $W$ , single top, and  $t\bar{t}+Z$  in each signal region. The normalizations of these backgrounds are determined simultaneously to best match the observed data in each control region taking contributions from all backgrounds into account. A likelihood function is built as the product of Poisson probability functions, describing the observed and expected number of events in the control regions[44]. This procedure takes common systematic uncertainties (discussed in Section 7.3) between the control and signal regions and their correlations into account as they are treated as nuisance parameters in the fit and are modeled by Gaussian probability density functions. The contributions from all

other background processes (dibosons and multijets) are fixed at the values expected from the simulation, using the most accurate theoretical cross sections available, while their uncertainties are used as nuisance parameters in the fit.

Validation Regions (VRs) are designed to validate the factors determined in the CRs and are a region orthogonal to both the SR and the CR while between the two kinematically, e.g. 0-lepton validation regions are closer kinematically than a 1- or 2-lepton CR.

The validation regions for  $Z$ +jets avoids overlap with the signal region by reversing the  $\Delta R(b, b)$  and/or the  $m_{\text{jet},R=1.2}^0/m_{\text{jet},R=0.8}^0$  requirement. The validation regions for  $t\bar{t}$  avoids overlap with the signal regions by reversing the  $m_T^{b,\min}$  requirement. More details on the VRs are shown in Section 7.2.

There are also important checks on the data and simulation that must be performed in order to be confident in the results. For this analysis the following checks were performed:

- Checking the dependence of discriminating variables on pileup to ensure that different pileup conditions do not affect the analysis.
- Checking for problems with specific runs by making sure that the data yields normalized by luminosity are consistent.
- Checking for any missing data by comparing processed data to reference numbers.

- Checking for duplicate events in simulation as previous productions contained a bug that caused this. This can cause regions to be mis-modeled.
- Checking the debug stream for any events in CRs and SRs. The debug stream catches events in which the trigger was unable to make a decision due to some failure in the online system.
- Checking the pileup reweighting to make sure that the pileup weight for simulation matches data after applying the weight.

The checks helped to validate the data and simulation and the data is stable and have high quality. Figure 5.7 show the dependence on pileup for  $m_{\text{jet},R=1.2}^0$ ,  $E_T^{\text{miss}}$ , and jet multiplicity. The full results for several of these checks are shown in Appendix A.

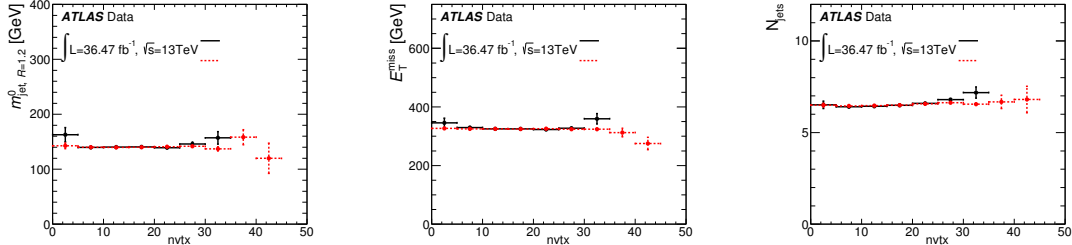


FIGURE 5.7. Checks on the dependence of pileup of  $m_{\text{jet},R=1.2}^0$ ,  $E_T^{\text{miss}}$ , and jet multiplicity. Ideally there is no dependence and the distributions are flat.

After the normalization factors have been validated, the background predictions are extrapolated to the SRs and then the data is “unblinded,” and the SRs are compared to observed data. For discovery a p-value is calculated in each SR and subregion independently.

As no excess is observed in any of the signal regions, new limits are placed on SUSY masses in the  $m_{\tilde{t}_1}-m$ , as shown in Figure 7.7 as well as in terms of  $m_{\tilde{g}}-m_{\tilde{t}_1}$ . For

the exclusion fits, the orthogonal subregions of SRA, SRB, and SRC are statistically combined. For the overlapping signal regions defined for SRD (SRD-low and SRD-high), the signal region with the smallest expected  $CL_s$ [45, 46] value is chosen for each signal model. Once the signal subregions are combined or chosen, the signal region with the smallest expected  $CL_s$  is chosen for each signal model in the  $\tilde{t}_1-\tilde{\chi}_1^0$  signal grid. Additionally, results are interpreted in terms of the pMSSM and several models have new exclusion limits. There are more details on the exclusion limits in Section 7.5.

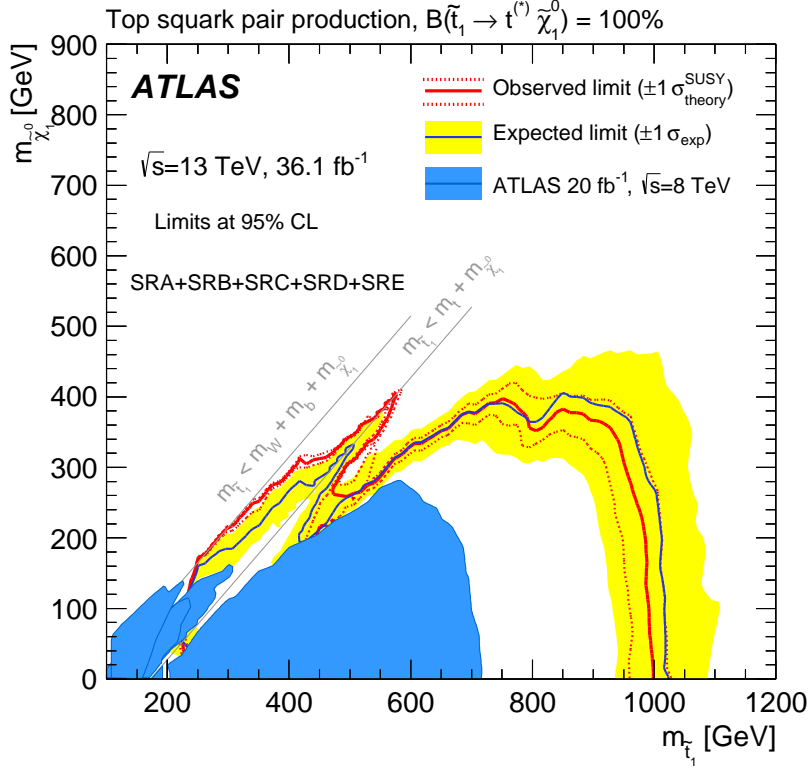


FIGURE 5.8. Observed (red solid line) and expected (blue solid line) exclusion contours at 95% CL as a function of  $\tilde{t}_1$  and  $\tilde{\chi}_1^0$  masses in the scenario where both top squarks decay via  $\tilde{t}_1 \rightarrow t^{(*)} \tilde{\chi}_1^0$ . Masses that are lower than the masses along the lines are excluded. Uncertainty bands corresponding to the  $\pm 1\sigma$  variation on the expected limit (yellow band) and the sensitivity of the observed limit to  $\pm 1\sigma$  variations of the signal theoretical uncertainties (red dotted lines) are also indicated. Observed limits from all third-generation Run-1 searches [47] at  $\sqrt{s} = 8$  TeV centre-of-mass energy are overlaid for comparison in blue.

## CHAPTER VI

### EVENT RECONSTRUCTION

#### 6.1. Particle Identification

The ATLAS detector tracks the path of final state particles and records their energy deposits. In order to determine what happened in the interaction point these particles must be identified and traced back in time to the interaction, reconstructing the event. This chapter discusses the process by which this is performed, including starting with tracks and topoclusters and constructing jets, leptons and photons, as well as the role that modeling has.

##### 6.1.1. Tracks

As a charged particle travels through the inner detector (ID) its path is curved by the 2T magnetic field created by the ATLAS solenoid magnet and it leaves “hits” in the ID layers. The hits are converted from raw data in the layers into three-dimensional measurements called space-points. Specialized algorithms reconstruct the charged particle trajectories from the space-points, and these trajectories can be used to determine the transverse and longitudinal impact parameters, the angles of the trajectory, and the ratio of charge to momenta[48]. Tracks are also used to reconstruct vertices, including secondary vertices which are important for identifying  $b$ -jets, and in jet calibration to reduce flavor dependence[49].

### 6.1.2. Topoclusters

Topological clusters (topoclusters) are groups of connected calorimeter cells defined by the 4-2-0 algorithm[50]. The 4-2-0 algorithm begins with seed cells which have an absolute value of signal energy greater than four times the noise energy (electronic and pileup). Then all adjacent cells with at least twice the noise energy are added to it, and then finally all adjacent cells with energy greater than 0 are added.

The topoclusters can have a local calibration applied, referred to as “local hadronic cell weighting” (LCW) calibration. These values are determined with MC simulations and is called “local” because it calibrates small and local topoclusters. If this weight is applied the topoclusters are referred to as LCTopo jets, otherwise they are EMTopo jets.

## 6.2. Jets

### 6.2.1. Jet-finding

The topoclusters are used as inputs to a jet finding algorithm. A jet finding algorithm must satisfy two requirements; first, that adding or removing a soft jet will not change the jet collections (infrared safe) and second that splitting or merging high  $p_T$  particles will not change the jet collections (collinear safe). Jet finding algorithms that are not safe are infrared or collinear sensitive; this is illustrated in Figure 6.1.

The jet finding algorithm currently most commonly used at ATLAS is the anti- $k_t$  algorithm, which is one of several  $k_t$  algorithms. These algorithms start by calculating

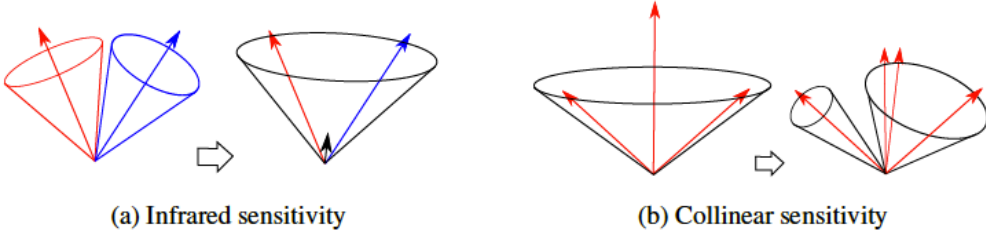


FIGURE 6.1. Illustration of a) infrared sensitivity and b)collinear sensitivity (figure from [51]). Adding a soft jet merges the jets when infrared sensitive and splitting the high  $p_T$  jet separates the jets when collinear sensitive.

the distances between an entity  $i$  and all possible pseudojets  $j$ ,  $d_{ij}$ , and between  $i$  and the beam  $B$ ,  $d_{iB}$  as:

$$d_{ij} = \min(k_{ti}^{2p}, k_{tj}^{2p}) \frac{(\Delta R)_{ij}^2}{R}, \quad (6.1)$$

$$d_{iB} = k_{ti}^{2p} \quad (6.2)$$

where  $R = \sqrt{(\Delta\eta)^2 + (\Delta\phi)^2}$  is the distance parameter (most commonly in ATLAS is  $R = 0.4$ ),  $k_t = p_T$ , and  $p$  is an integer whose value depends on the specific algorithm. The inclusive  $k_t$  algorithm has a  $p$  value of 1, the anti- $k_t$  algorithm has a  $p$  value of -1, and the inclusive Cambridge/Aachen algorithm has a  $p$  value of 0. If  $d_{ij}$  is smaller than  $d_{iB}$  then  $i$  and  $j$  are merged, otherwise  $i$  is labeled as a jet and removed from the list of entities. This is repeated for all possible entities.

The  $k_t$  family of algorithms are both infrared safe and collinear safe. Figure 6.2 shows how the anti- $k_t$  algorithm performs compared to other jet finding algorithms. Note that for the anti- $k_t$  algorithm hard jets have a circular, more physical shape that gives good position resolution, with a radius equal to the distance parameter  $R$  while

softer jets are crescent moon-shaped when bordering a hard jet, which takes some of the area of the softer jet. Compare this to, for instance, the  $k_t$  algorithm where the jets have irregular shapes and lighter jets can steal some of the area of the harder jets.

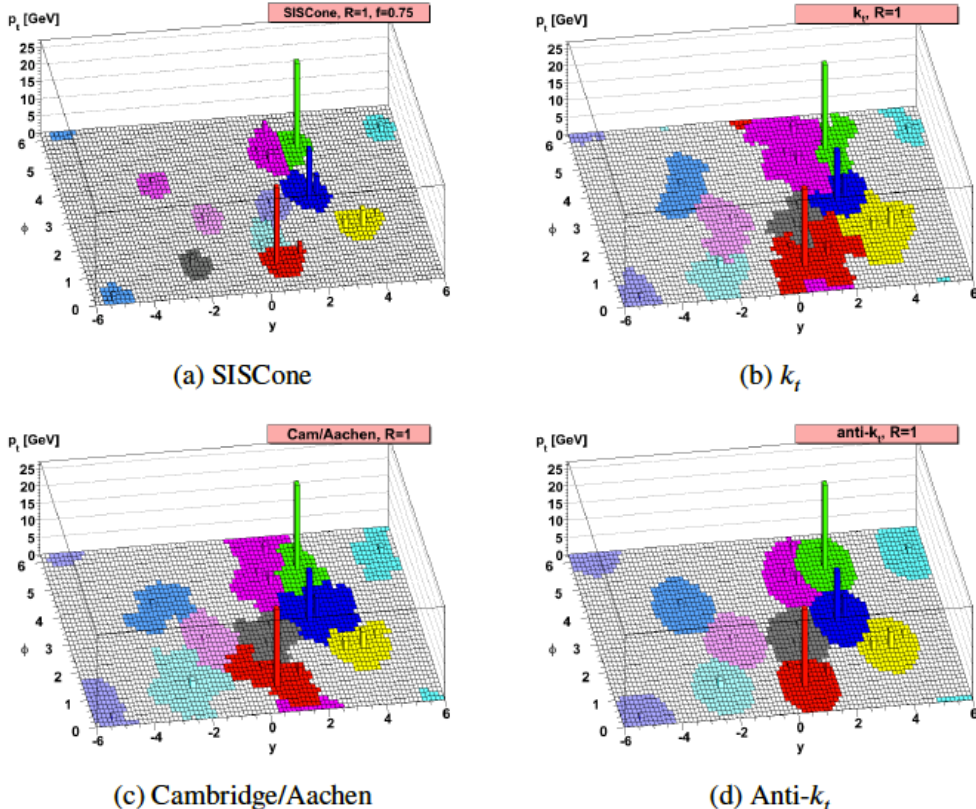


FIGURE 6.2. Results from several jet finder algorithms (figure from [52]). Note the shape differences in different algorithms and what jet  $p_T$ s can steal away from other jets.

### 6.2.2. Jet calibration

After the jets are constructed they must be calibrated. The steps are shown in Figure 6.3. First, a pileup correction is made by subtracting the average energy of the  $\eta \times \phi$  plane as well as corrections based on the number of primary vertices and

the average number of interactions per bunch crossing.

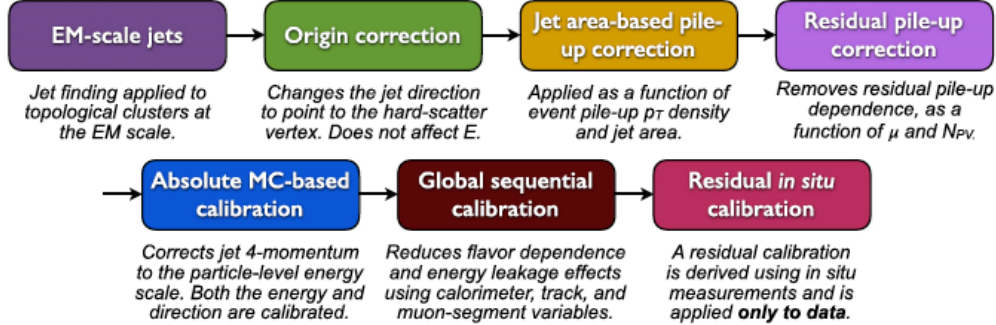


FIGURE 6.3. Jet calibration steps at ATLAS (diagram from [53]).

Next the jet energy scale (JES) correction is applied. The scale factors are determined from truth particles in simulation and are a function of  $\eta$  and  $p_T$  of the jet. An origin correction is also applied to correct for bias in the  $\eta$  direction, which shows up especially in the gap and transition regions.

There is also dependence of the JES on longitudinal and transverse features of the jet. These dependencies are corrected sequentially as they are mostly uncorrelated. These dependencies include the fraction of energy deposited in the tile calorimeter and in the third layer of the EM calorimeter, the number of tracks associated to the jet, the  $p_T$ -weighted width of the tracks, and the number of muon segments associated to the jet. These corrections are referred to as global sequential corrections.

Finally in situ corrections correct differences between data and MC. This is performed with well-measured and understood objects like  $\gamma/Z + \text{jets}$  and multijet processes.

### 6.2.3. Jet cleaning

There can be several backgrounds for jets coming from hard collisions, including[54]:

- Beam induced background (BIB), coming from proton interactions upstream of the interaction point
- Cosmic-ray showers, produced in the atmosphere and mostly made up of muons as most other particles will not penetrate to the depth of the detector underground
- Calorimeter noise from large scale coherent noise or isolated pathological cells

The process to reject these "fake" jets is called "jet cleaning" and uses the following variables:

- $Q_{cell}^{LAr}$ : The quadratic difference between actual and expected pulse shapes
- $\langle Q \rangle$ : The average jet quality, defined as the energy-squared weighted average of pulse quality of the calorimeter cells in the jet
- $f_Q^{LAr}$ : Fraction of the energy in the LAr calorimeter cells of a jet with poor signal shape quality
- $f_Q^{HEC}$ : Fraction of energy in the HEC calorimeter cells of a jet with poor signal shape quality
- $E_{neg}$ : Sum of the energy of all cells with negative energy as negative energy in a good jet is due to electronic and pileup noise

- $f_{ch}$ : Ratio of the scalar sum of the  $p_T$  of the tracks from the primary vertex associated with the jet to the jet  $p_T$
- $f_{max}$ : The fraction of the jet energy in the layer with maximum deposit.

A jet is considered fake if it satisfies at least one of the requirements listed above. The first two identify jets due to sporadic noise bursts in HEC, the third identifies jets due to large coherent noise or isolated pathological cells in LAr, and the last three are more general and identify hardware issues, BIB or cosmic muon showers:

- $f_{HEC} > 0.5$  and  $|f_Q^{HEC}| > 0.5$  and  $\langle Q \rangle > 0.8$
- $|E_{neg}| > 60$
- $f_{EM} > 0.95$  and  $f_Q^{LAr} > 0.8$  and  $\langle Q \rangle > 0.8$  and  $|\eta| < 2.8$
- $f_{max} > 0.99$  and  $|\eta| < 2$
- $f_{EM} < 0.05$  and  $f_{ch} < 0.05$  and  $|\eta| < 2$
- $f_{EM} < 0.05$  and  $|\eta| \geq 2$

#### 6.2.4. *b*-tagging

Since bottom quarks have a delayed decay due to the small decay rates to up and charm quarks,  $B$  mesons live long enough to travel a significant distance, on the order of hundreds of  $\mu\text{m}$  from the primary vertex before decaying to lighter hadrons. The tracks that these lighter hadrons produce trace to a secondary vertex instead of the primary vertex and this can be used to discriminate  $b$ -jets from other jets. Unfortunately charm quarks as well as tau leptons also can have delayed decays so it can be difficult to distinguish between the two. Therefore multivariate

algorithms have been developed[55] that use information such as the impact parameter significance, presence of a secondary vertex, and reconstruction of  $B$  meson decay chains to tag  $b$ -jets. The algorithm used in this search has an efficiency of 77%, with rejection factors for charm quarks, light-flavor and tau leptons rejection factors, which are the opposite of efficiency, of 5, 10, and 140 respectively.

### 6.3. Electrons

Electrons leave a track in the ID as well as producing an electromagnetic (EM) shower in the calorimeter. Electrons are reconstructed by[56]:

- A sliding window of size  $3 \times 5$  in  $\eta \times \phi$  corresponding to the granularity of the middle layer of the LAr calorimeter search for electron cluster “seeds” with cluster energy greater than 2.5 GeV. Clusters are formed around the seeds that allow for duplicates to be removed.
- Pattern recognition for the track fit uses the electron hypothesis, which allows for more energy to be lost by bremsstrahlung.
- Seed clusters and tracks are matched to give electron candidates.

However an electron can be not-prompt, meaning that it is a product of a delayed decay and is not a signal object. An electron can also be produced from a background jet or a photon conversion. In order to reject background electrons to signal electrons a number of discriminating variables are used in addition to track-cluster matching, including hadronic leakage, EM layer information, track conditions, and TRT radiation. A likelihood-based method is used to reject background photons with Loose, Medium, Tight, with each a subset of previous criteria, and the VeryLoose

criteria which is used in this analysis to reject electrons. Electrons falling into the gap region, from  $1.37 < |\eta| < 1.52$ , are also considered electrons in the analysis. For this search electrons are also required to be isolated in a cone of  $\Delta R = 0.2$  divided by the electron  $p_T$  to reduce background from hadrons imitating a lepton and from leptons from hadron decays or photon conversion.

For signal electrons, used in the control regions, the electron must have a  $p_T$  greater than 20 GeV, have  $|\eta| < 2.47$  and is rejected of  $0.2 < \Delta R(e, jet) < 0.4$ .

#### 6.4. Photons

While photons produce an EM shower in the calorimeter, unlike electrons they are not charged and therefore should not leave a track in the ID. This is complicated by the possibility of pair production from a photon in the tracker. In this case the cluster is matched to two oppositely-charged tracks. If there are no tracks associated to a cluster then it is considered an unconverted photon. Similar to Section 6.3, shower shape variables from hadronic leakage and EM layer information is used[57] to create two criteria, loose and tight. Photons are used in this analysis for the control region for  $t\bar{t} + V$  background.

#### 6.5. Muons

Since muons act as minimum-ionizing particles (MIPS) through the calorimeter, the outermost part of the ATLAS detector, the muon spectrometer (MS) is used to detect and measure properties of muons. Several criteria are used to identify muons[58]: *q/p significance*, the difference in the ratio of charge and momenta

measured in the ID and MS;  $\rho'$ , the difference between the transverse momenta measured in the ID and MS; and the normalized  $\chi^2$  of the combined track fit. There are also requirements on the numbers of hits in the ID and MS.

There are four muon types depending on the subdetectors used in the reconstruction. Combined muons use hits in the MS to trace back to hits in the ID to reconstruct the muon track, though the opposite approach can complement this. Segment-tagged muons are formed when a track in the ID is matched to one layer in the MS because of low  $p_T$  or because it crosses a region in the MS with reduced acceptance. Calorimeter-tagged muons identifies a muon consistent with a MIP in the calorimeters and is used to find muons that cross the ID and MS in regions where cabling prevents particle detection. Extrapolated muons require only tracks in the MS for regions beyond the coverage of the ID.

After identifying and classifying the muons there are four selections based on the type of muon with additional criteria, Loose, Medium, Tight, and High- $p_T$  in order of rejecting background. Loose (Medium) criteria with  $p_T > 6 \text{ GeV}$  ( $p_T > 20 \text{ GeV}$ ) with  $\Delta R(\mu, \text{jet}) > 0.4$  are used to identify muons for the signal regions (control regions).

Additionally, bad or fake muons can be identified by high hit multiplicities in the MS. This is due to very energetic punch-through jets, which survive the calorimeters and enter the MS, or badly mis-measured ID tracks in jets wrongly matched to MS segments. These fake muons are a potential source of fake  $E_T^{\text{miss}}$ .

## 6.6. Taus

The tau lepton is the only lepton heavy enough to decay hadronically, which results in a final state of a tau neutrino and jets from the  $W$  decay in  $t\bar{t}$  or  $W+\text{jets}$  events. The decay can have either 1 or 3 charged hadrons; therefore a jet is identified as a tau candidate if it has four or fewer tracks, is close to the  $E_{\text{T}}^{\text{miss}}$  vector ( $\Delta\phi(E_{\text{T}}^{\text{miss}}, \text{jet}) < \pi/5$ ) from the neutrino, as well as not  $b$ -tagged. In this analysis these are not fully reconstructed in order to have efficient rejection of  $\tau$  candidates from the  $W$  bosons, and leptonic decays are rejected from the lepton veto.

## 6.7. Missing Transverse Momentum

Missing transverse momentum,  $E_{\text{T}}^{\text{miss}}$ , is the vector sum of transverse momenta of all final state particles. This sum must be equal to zero or there are some final state particles that are invisible to the detector, such as neutrinos or new physics. Only transverse momenta can be calculated from a hadron collider like the LHC since momenta of the colliding protons is non-uniformly distributed across its constituent partons (thus the missing  $z$ -momenta cannot be calculated). As a function of its  $x$  and  $y$  components,  $E_{\text{T}}^{\text{miss}}$  and its azimuthal angle  $\phi^{\text{miss}}$  is:

$$\mathbf{p}_{\text{T}}^{\text{miss}} = \sqrt{(E_x^{\text{miss}})^2 + (E_y^{\text{miss}})^2} \quad (6.3)$$

$$\phi^{\text{miss}} = \arctan\left(\frac{E_y^{\text{miss}}}{E_x^{\text{miss}}}\right) \quad (6.4)$$

The missing energy vector is therefore defined as:

$$\mathbf{p}_T^{\text{miss}} = -\Sigma(p_T(e) + p_T(\gamma) + p_T(\text{jets}) + p_T(\mu) + p_T(\text{soft})), \quad (6.5)$$

where  $p_T(e)$ ,  $p_T(\gamma)$ ,  $p_T(\text{jets})$ ,  $p_T(\mu)$  are the momenta of electrons, photons, jets, and muons. Low- $p_T$  objects not associated with hard  $p_T$  objects and unassociated topoclusters are grouped into the  $p_T(\text{soft})$  term. There are several methods of calculating  $E_T^{\text{miss}}$  that differ in important ways, several of which are compared[59].

The first includes a calorimeter-based soft term, CSC  $E_T^{\text{miss}}$ . This is constructed from energy deposits in the calorimeter not associated with hard objects that come from underlying event activity and soft radiation. This is vulnerable to pileup interactions, both in-time and out-of-time. The second, Track  $E_T^{\text{miss}}$  uses tracks from the inner detector and is therefore resilient to pileup. However, used purely it misses neutral particles that don't leave tracks. The third includes a track-based soft term, TST  $E_T^{\text{miss}}$ , and is combined with the calorimeter-based measurements for the hard terms. This is a good compromise between the first two methods and is the primary method for Run 2, including for this analysis, while CST  $E_T^{\text{miss}}$  was the primary method for Run 1. Pure track  $E_T^{\text{miss}}$  is also used to reject  $E_T^{\text{miss}}$  from mis-modeled jets.

## 6.8. Monte Carlo Simulations

The complexities of collisions and decays, along with detector effects, make full calculations unmanageable. Therefore in order to test predictions from theory,

observables in data must be compared to those in computer simulations. This is performed with event generators and detector simulations.

### 6.8.1. Event Generators

To simulate particle interactions and productions Monte Carlo generators are used as the number of observables and uncertainties in theory predictions and experimental effects and uncertainties make calculations unmanageable.

Figure 6.4 shows a simplified diagram of an event. Quarks and gluons, which carry color, can emit QCD radiation either as initial state radiation (ISR) or final state radiation (FSR). Parton shower (PS) generators simulate these processes, the precision of which are leading logarithm (LL), next-to-leading logarithm (NLL), etc, classified by the number of logarithms arriving from loop calculations.

To begin with, the momentum of an individual proton is non-uniformly spread out over its components. The fraction of momenta each parton carries is controlled by the parton distribution function (PDF) which is determined experimentally. Then hard scattering and following possible decays are called matrix elements (ME) and are computed to some approximation as it is too laborious to calculate beyond a few orders in perturbation theory. The precision of the approximation is leading order (LO), next-to-leading order (NLO), etc.

There are various Monte Carlo generators that are used to simulate events that can be chosen depends on the physics needs:

- SHERPA[60]: (Simulation of High-Energy Reactions of PArticles) A general-purpose tool that contains a flexible tree-level matrix-element generator for

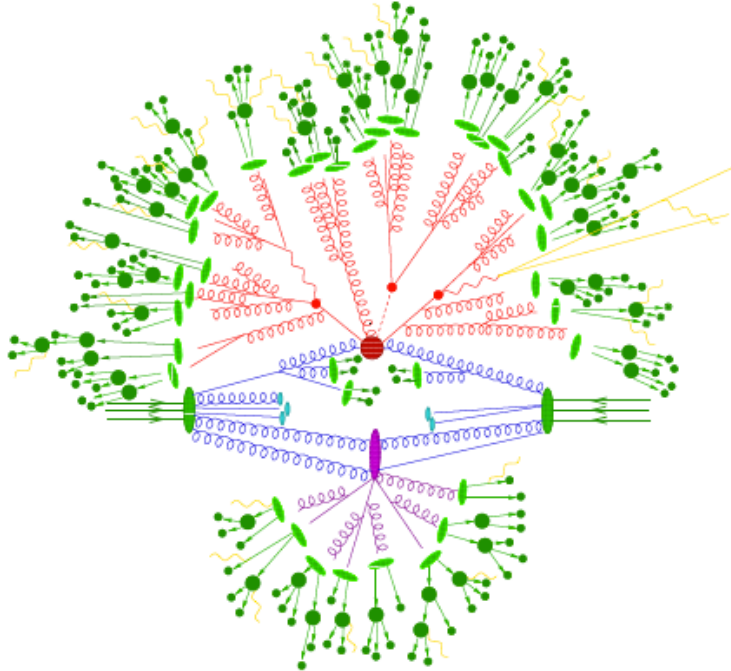


FIGURE 6.4. Pictorial representation of a  $t\bar{t}$  event produced by an event generator (figure from [60]). The large red blob is the hard interaction followed by decays of the top quarks and Higgs as smaller red blobs. Hard QCD scattering is produced in red and a secondary interaction takes place in the purple blob, then the final-state partons hadronize, light green, and hadrons decay, dark green. Additional photon radiation can occur at any stage and is in yellow.

calculating hard scattering processes with both SM and new physics models.

This generator is used for  $Z+\text{jets}$  and  $W+\text{jets}$  in the analysis.

- PYTHIA[61]: A standard tool for modeling the evolution from a few-body hard process to a complex multihadronic final state, including modeling ISR and FSR parton showers.
- POWHEG[62]: (Positive Weight Hardest Emission Generator) A NLO generator. For this analysis leptonic top decay and single-top production background processes use this generator interfaced to PYTHIA for parton scattering and hadronization.

- MadGraph\_aMC@NLO[63]: A leading order and NLO amplitude and event generator. For this analysis  $t\bar{t} + V$ , where  $V$  is a  $W$  or  $Z$ , and  $t\bar{t} + \gamma$  background processes use this generator interfaced to PYTHIA for parton scattering and hadronization.
- EvtGen[64]: A generator for  $b$  physics including underlying events, used for  $b$ -hadron decays in this analysis.

Table 6.1 shows an overview of the generators used for the signal samples and each of the backgrounds.

TABLE 6.1. Overview of the nominal simulated samples.

Process	Generator	fragm./hadron.	PDF set	UE Tune	Cross section order
SUSY Signal	MADGRAPH5_AMC@NLO	PYTHIA 8	NNPDF2.3	A14	LO
$t\bar{t}$	POWHEG-BOX v2	PYTHIA 6	CT10	PERUGIA 2012	NLO
Single top	POWHEG-BOX v2	PYTHIA 6	CT10	PERUGIA 2012	NLO
$W/Z+jets$	SHERPA 2.2.1	SHERPA	NNPDF3.0NNLO	Default	NLO
Diboson	SHERPA 2.2	SHERPA	CT10	Default	LO
$t\bar{t} + V$	MADGRAPH5_AMC@NLO	PYTHIA 8	NNPDF3.0NNLO	A14	NLO

### 6.8.2. Detector Simulation

The toolkit GEANT[65] was developed to simulate all aspects particles passing through the detector, including tracking, geometry, physics models, and particle showers in calorimeters and covers a comprehensive range of physics processes. In a full simulation particles' interactions with every part of ATLAS is simulated with all details, and in fast simulation showers in the EM and hadronic calorimeters are simulated. Energy deposits are processed in the digitizer to simulated the readout system and then turned into the raw data format identical to real data. Figure 6.5 puts the simulations together visually.

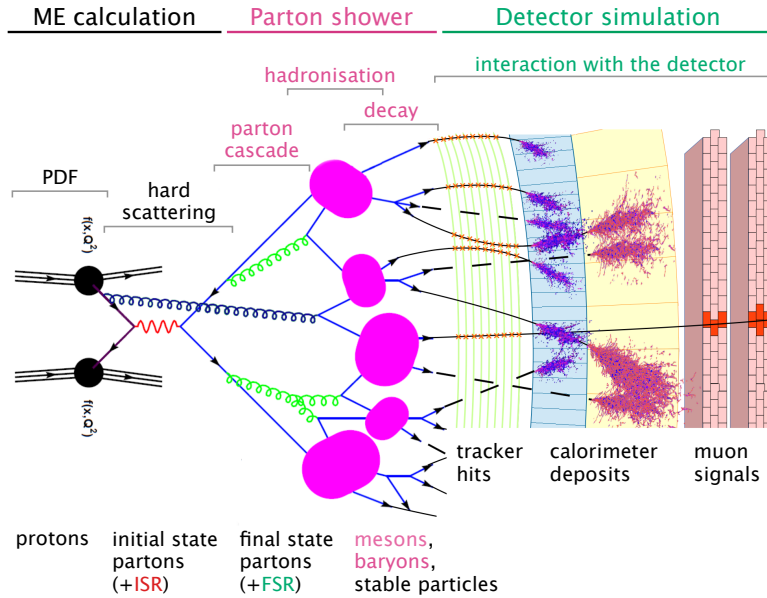


FIGURE 6.5. Visual representation of different stages of simulation (figure from [66]).

This chapter described the way in which events are reconstructed and modeled, which is essential to performing the analysis described in Chapter VII.

## CHAPTER VII

### ANALYSIS

This chapter describes the analysis in depth, beginning with the signal regions and continuing with background estimation and finally presenting the results, interpretations, and outlook. This work was published in 2017 in *JHEP*[1]. This chapter contains material coauthored with the ATLAS Collaboration. I was the primary contributor to the  $t\bar{t}$  background estimation. Other members of the analysis group, part of the ATLAS Collaboration, estimated other backgrounds, and the background estimates were used by the analysis group to produce the results, including exclusion plots. The lightest supersymmetric partner to the top quark<sup>1</sup> being produced in direct pair production is the main focus of the analysis, while other scenarios are also discussed.

#### 7.1. Signal Region Definitions

Leading order stop pair-production at the LHC is expected to be dominated by gluon fusion, then by the subprocess  $q\bar{q}$  annihilation. The stops are pair produced, conserving  $R$ -parity, and are produced directly, so there are no intermediate particles in the simplified model.

As discussed in Chapter V there are five distinct signal regions developed to optimize discovery significance for different topologies, SRA-E. All of the searches share the following preselection requirements:

---

<sup>1</sup> There is a SUSY partner to the helicity states of the top quark in the SM,  $\tilde{t}_L$  and  $\tilde{t}_R$ , which mix to form the  $\tilde{t}_1$  and  $\tilde{t}_2$  where the  $\tilde{t}_1$  is the lightest of the two.

- For data samples, events must be in the Good Runs List (GRL), which are runs that pass certain data quality requirements.
- For data samples, Must pass cleaning selection which removes events with incomplete data or with calorimeter noise bursts.
- The event must pass the lowest unprescaled  $E_T^{\text{miss}}$  trigger as well as have offline  $E_T^{\text{miss}} > 250$  GeV.
- The event must have a reconstructed primary vertex.
- The event must not contain any “bad jets” from the jet definition described in section 6.2.3 with  $p_T > 20$  GeV.
- The event must not contain any cosmic muons as discussed in section 6.2.3
- The event must not contain any bad muons as described in section 6.5.
- The event must contain no baseline electron candidates with  $p_T > 7$  GeV and no baseline muons with  $p_T > 6$  GeV.
- The event must contain at least four jets.
- The  $\Delta\phi$  between the leading two (three) jets and the  $E_T^{\text{miss}}$ ,  $|\Delta\phi(\text{jet}^{0,1}, \mathbf{p}_T^{\text{miss}})|$ , ( $|\Delta\phi(\text{jet}^{0,1,2}, \mathbf{p}_T^{\text{miss}})|$ ), must be greater than 0.4 for ISR based regions (non-ISR based regions).
- The  $E_T^{\text{miss,track}}$  must be greater than 30 GeV.
- The  $\Delta\phi$ , between the calo  $E_T^{\text{miss}}$  and the  $E_T^{\text{miss,track}}$ ,  $|\Delta\phi(\mathbf{p}_T^{\text{miss}}, \mathbf{p}_T^{\text{miss,track}})|$ , must be smaller than  $\pi/3$ .
- At least one b-tagged jet at the 77% working point is required.

The analysis relies heavily on reconstruction top quark candidates, which is done using jet “reclustering.” Jet reclustering is performed using the anti- $k_t$  algorithm with a larger distance parameter (i.e.  $R = 1.2$ ) over the calibrated anti- $k_t$   $R = 0.4$  jet collection. The highest (second-highest)  $p_T$  reclustered jet is designated as the first (second) top candidate. Various optimization studies have found that this method using  $R = 1.2$  (top candidate) and  $R = 0.8$  ( $W$  candidate) results in the best signal sensitivity. The mass distribution is shown in Figure 7.1. The masses are indicated by  $m_{\text{jet},R=1.2}^0$ ,  $m_{\text{jet},R=1.2}^1$ ,  $m_{\text{jet},R=0.8}^0$ ,  $m_{\text{jet},R=0.8}^1$ .

A suite of discriminating variables based on anti- $k_t$   $R = 0.4$  jets will be considered in the analysis optimization:

- $|\Delta\phi(\text{jet}^{0,1}, \mathbf{p}_T^{\text{miss}})|$ : The difference in  $\phi$  between the jet and  $E_T^{\text{miss}}$  for the two leading jets in the event. This variable rejects events with fake  $E_T^{\text{miss}}$  from QCD, hadronic  $t\bar{t}$ , and detector effects.
- $H_T$ : The scalar sum of the  $p_T$  of all signal anti- $k_t$   $R = 0.4$  jets ( $p_T > 20$  GeV,  $|\eta| < 2.8$ , after overlap removal).
- $m_T^i$ : The transverse mass ( $m_T$ ) between the  $i$ th jet and the  $E_T^{\text{miss}}$  in the event. The massless approximation is used for this and all following  $m_T$  variables:  

$$m_T^i = \sqrt{2p_T^{\text{jet},i}E_T^{\text{miss}}(1 - \cos\Delta\phi(\text{jet}^i, E_T^{\text{miss}}))}$$
, where  $p_T^{\text{jet},i}$  is the transverse momentum of the  $i$ th jet.
- $m_T^{b,\text{min}}$ : Transverse mass between closest  $b$ -jet to  $E_T^{\text{miss}}$  and  $E_T^{\text{miss}}$ . This variable provides the most powerful discrimination between signal and semileptonic  $t\bar{t}$  background.

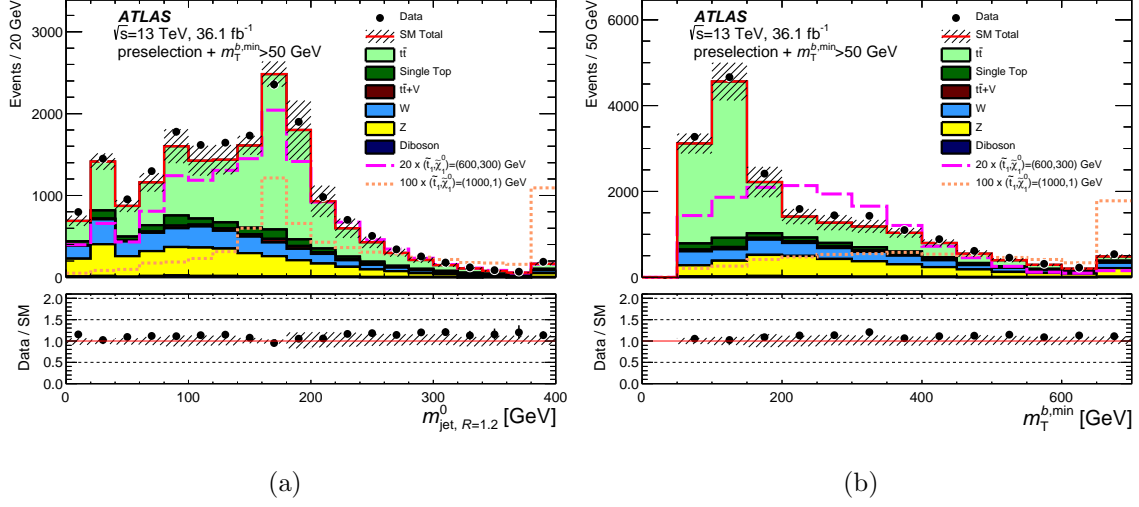


FIGURE 7.1. Distributions of the discriminating variables (a)  $m_{\text{jet},R=1.2}^0$  and (b)  $m_T^{b,\text{min}}$  after the common preselection and an additional  $m_T^{b,\text{min}} > 50 \text{ GeV}$  requirement. The stacked histograms show the SM prediction before being normalized using scale factors derived from the simultaneous fit to all dominant backgrounds. The “Data/SM” plots show the ratio of data events to the total SM prediction. The hatched uncertainty band around the SM prediction and in the ratio plots illustrates the combination of statistical and detector-related systematic uncertainties. The rightmost bin includes overflow events.

- $m_T^{b,\text{max}}$ : Transverse mass between furthest  $b$ -jet to  $E_T^{\text{miss}}$  and  $E_T^{\text{miss}}$ . This variable provides very good discrimination between signal and semileptonic  $t\bar{t}$  background.
- $\Delta R(b,b)$ : The angular separation between the two jets with the highest  $b$  weights. This variable is useful in discriminating against the  $Z(\nu\bar{\nu}) + b\bar{b} + \text{jets}$  background.

A common preselection used for all five sets of signal regions is defined in Table 7.1.

Distributions of (a)  $m_{\text{jet},R=1.2}^0$  and (b)  $m_T^{b,\text{min}}$  are shown in Figure 7.1.

TABLE 7.1. Selection criteria common to all signal regions. Different triggers were used for different data periods in 2016.

Trigger	Data 2015: HLT_xe70_mht_L1XE50 Data 2016: HLT_xe90_mht_L1XE50, HLT_xe100_mht_L1XE50, HLT_xe110_mht_L1XE50
$E_T^{\text{miss}}$	$> 250 \text{ GeV}$
$N_{\text{lep}}$	0
anti- $k_t$ $R = 0.4$ jets	$\geq 4$ , $p_T > 80, 80, 40, 40 \text{ GeV}$
$b$ -tagged jets	$\geq 1$
$ \Delta\phi(\text{jet}^{0,1}, \mathbf{p}_T^{\text{miss}}) $ or $ \Delta\phi(\text{jet}^{0,1,2}, \mathbf{p}_T^{\text{miss}}) $	$> 0.4$
$E_T^{\text{miss,track}}$	$> 30 \text{ GeV}$
$ \Delta\phi(\mathbf{p}_T^{\text{miss}}, \mathbf{p}_T^{\text{miss,track}}) $	$< \pi/3$

### 7.1.1. SRA and SRB

SRA and SRB are optimized for high stop masses. In addition to the preselection, SRA and SRB have common requirements of  $m_T^{b,\text{min}} > 200 \text{ GeV}$ , which reduces  $t\bar{t}$  background, two b-tagged jets, and a  $\tau$ -veto.

SRA is optimized to be sensitive to decays of heavy stops into a top quark and a light  $\tilde{\chi}_1^0$ . The main discriminating variables are the reclustered top masses, with  $R = 1.2$  and  $R = 0.8$ ,  $m_T^{b,\text{min}}$ ,  $\Delta R(b, b)$ , and  $E_T^{\text{miss}}$ . Events are divided into three categories based on the reconstructed top candidate mass ( $R = 1.2$  reclustered jet mass). The TT category includes events with two well-reconstructed top candidates, the TW category contains events with a well-reconstructed leading  $p_T$  top candidate and a well-reconstructed subleading  $W$  candidate (from the subleading  $R = 1.2$  reclustered mass), and the T0 category represents events with only a leading top

candidate.

The categorization showed an improvement in discovery significance, assuming the shape of the  $m_{\tilde{t}_1} = 800$  GeV,  $m_{\tilde{\chi}_1^0} = 1$  GeV benchmark, from  $2\sigma$  to  $3\sigma$ , yielding comparable results to a boosted decision tree (BDT). For the benchmark point with  $m_{\tilde{t}_1} = 1000$  GeV,  $m_{\tilde{\chi}_1^0} = 1$  GeV, after the SRA-B preselection,  $\sim 91\%$  (TT=38%, TW=22%, and T0=31%) of events fall into one of these three categories.

Additionally, requirements on the stransverse mass ( $m_{\text{T2}}^{\chi^2}$ ) [67, 68] are made which are especially powerful in the T0 category where a  $\chi^2$  method is applied to reconstruct top quarks with lower momenta where reclustering was suboptimal. The  $m_{\text{T2}}^{\chi^2}$  variable is constructed from the direction and magnitude of the  $\mathbf{p}_{\text{T}}^{\text{miss}}$  vector in the transverse plane as well as the direction of two top-quark candidates reconstructed using a  $\chi^2$  method. The minimization in this method is done in terms of a  $\chi^2$ -like penalty function,  $\chi^2 = (m_{\text{cand}} - m_{\text{true}})^2 / m_{\text{true}}$ , where  $m_{\text{cand}}$  is the candidate mass and  $m_{\text{true}}$  is set to 80.4 GeV for  $W$  candidates and 173.2 GeV for top candidates. Initially, single or pairs of  $R = 0.4$  jets form  $W$  candidates which are then combined with additional  $b$ -tagged jets in the event to construct top candidates. The top candidates selected by the  $\chi^2$  method are only used for the momenta in  $m_{\text{T2}}^{\chi^2}$  while the mass hypotheses for the top quarks and the invisible particles are set to 173.2 GeV and 0 GeV, respectively.

A similar strategy was taken for the optimization of SRB which is aimed at being sensitive to  $m_{\tilde{t}_1} = 600$  GeV,  $m_{\tilde{\chi}_1^0} = 300$  GeV. In addition to the  $E_{\text{T}}^{\text{miss}}$  and reclustered masses,  $m_{\text{T}}^{b,\text{max}}$ ,  $m_{\text{T}}^{b,\text{min}}$ , and  $\Delta R(b, b)$  were used in the optimization. The fraction of events in each category is after the SRA-B preselection: TT=14%, TW=20%,

$T_0=35\%$ . All three categories are used in the optimization resulting in the signal regions defined in Table 7.2.

TABLE 7.2. Selection criteria for SRA and SRB, in addition to the common preselection requirements as shown in Table 7.1. The signal regions are separated into topological categories based on reconstructed top-candidate masses.

Signal Region		TT	TW	T0
	$m_{\text{jet},R=1.2}^0$	$> 120 \text{ GeV}$		
	$m_{\text{jet},R=1.2}^1$	$> 120 \text{ GeV}$	$[60, 120] \text{ GeV}$	$< 60 \text{ GeV}$
	$m_T^{b,\text{min}}$	$> 200 \text{ GeV}$		
	$N_{b-\text{jet}}$	$\geq 2$		
	$\tau$ -veto	yes		
	$ \Delta\phi(\text{jet}^{0,1,2}, \mathbf{p}_T^{\text{miss}}) $	$> 0.4$		
<b>A</b>	$m_{\text{jet},R=0.8}^0$	$> 60 \text{ GeV}$		
	$\Delta R(b, b)$	$> 1$	-	
	$m_{T2}^{\chi^2}$	$> 400 \text{ GeV}$	$> 400 \text{ GeV}$	$> 500 \text{ GeV}$
	$E_T^{\text{miss}}$	$> 400 \text{ GeV}$	$> 500 \text{ GeV}$	$> 550 \text{ GeV}$
<b>B</b>	$m_T^{b,\text{max}}$	$> 200 \text{ GeV}$		
	$\Delta R(b, b)$	$> 1.2$		

### 7.1.2. SRC

The signature of stop decays when  $\Delta m(\tilde{t}_1, \tilde{\chi}_1^0) \sim m_t$  is significantly softer with low  $E_T^{\text{miss}}$ . This decay topology is very similar to non-resonant  $t\bar{t}$  production making signal and background separation challenging. However, several kinematic properties can be exploited to separate stop decays from  $t\bar{t}$  when an ISR jet is present in the

final state.

An additional set of discriminating variables is defined for signal regions using ISR to gain sensitivity the compressed ( $m_{\tilde{t}_1} - m_{\tilde{\chi}_1^0} \sim m_t$ ) signal grid region. These variables are all defined in the transverse center-of-mass (CM) of the sparticle plus ISR frame. Visible objects are grouped into being either a part of the ISR or the sparticle system. This is performed using a recursive jigsaw reconstruction technique[69], which looks for a “thrust axis” where the  $p_T$ -projection of all jets and  $E_T^{\text{miss}}$  in the center of mass frame in the event are maximized. This axis then divides the space into the sparticle or ISR system. This association with the ISR or sparticle system is indicated by an ISR or S superscript, respectively. The “V” subscript denotes the visible part of system. For example,  $m_V$  denotes the transverse mass of only the visible (jets+leptons) part of the sparticle system without the  $E_T^{\text{miss}}$ . The variables considered are:

- $N_{b\text{-jet}}^S$ : number of b-tagged jets associated with the sparticle hemisphere.
- $N_{\text{jet}}^S$ : number of jets associated with the sparticle hemisphere.
- $p_{T,b}^{0,S}$ :  $p_T$  of the leading b-jet in the sparticle hemisphere.
- $p_T^{4,S}$ :  $p_T$  of the fourth jet ordered in  $p_T$  in the sparticle hemisphere.
- $\Delta\phi(\text{ISR}, \mathbf{p}_T^{\text{miss}})$ : angular separation in  $\phi$  of the ISR and the  $E_T^{\text{miss}}$  in the CM frame.
- $p_T^{\text{ISR}}$ :  $p_T$  of the ISR system, evaluated in the CM frame.
- $m_S$ : transverse mass between the whole sparticle system and  $E_T^{\text{miss}}$ .

- $m_V/m_S$ : ratio of the transverse mass of the only the visible part of the sparticle system without  $E_T^{\text{miss}}$  and the whole sparticle system including  $E_T^{\text{miss}}$ .
- $R_{\text{ISR}}$ : Ratio between invisible system ( $E_T^{\text{miss}}$ in CM frame) and  $p_T^{\text{ISR}}$

After the preselection, defined in Table 7.1, additional requirements are made resulting in five signal regions, SRC-1 through SRC-5, for which the exact requirements are listed in Table 7.3.

TABLE 7.3. Selection criteria for SRC, in addition to the common preselection requirements as shown in Table 7.1. The signal regions are separated into windows based on ranges of  $R_{\text{ISR}}$ .

Variable	SRC1	SRC2	SRC3	SRC4	SRC5
$N_{b-\text{jet}}$			$\geq 1$		
$N_{b-\text{jet}}^S$			$\geq 1$		
$N_{\text{jet}}^S$			$\geq 5$		
$p_{T,b}^{0,S}$			$> 40 \text{ GeV}$		
$m_S$			$> 300 \text{ GeV}$		
$\Delta\phi(\text{ISR}, \mathbf{p}_T^{\text{miss}})$			$> 3.0$		
$p_T^{\text{ISR}}$			$> 400 \text{ GeV}$		
$p_T^{4,S}$			$> 50 \text{ GeV}$		
$R_{\text{ISR}}$	0.30–0.40	0.40–0.50	0.50–0.60	0.60–0.70	0.70–0.80

### 7.1.3. SRD

The selections for SRD are optimized for the decay of both pair-produced top squarks into a  $b$  quark and a  $\tilde{\chi}_1^\pm$ . In this case no top-quark candidates are reconstructed, so the sum of the transverse momenta of the two jets with the highest  $b$ -tagging weight, as well as that of the second, fourth, and fifth highest, are used for

additional background rejection. The models considered for the optimization have the chargino mass fixed to two times the neutralino mass,  $m(\tilde{\chi}_1^\pm) = 2 \cdot m(\tilde{\chi}_1^0)$ .

The best selections for the signal samples with  $m(\tilde{t}_1) = 400$  GeV,  $m(\tilde{\chi}_1^0) = 50$  GeV (SRD-low),  $m(\tilde{t}_1) = 700$  GeV,  $m(\tilde{\chi}_1^0) = 100$  GeV (SRD-high) are reported in Table 7.4. The two regions are not combined, individual p-values are quoted for discovery while the region with the best expected sensitivity is chosen during the exclusion fit.

TABLE 7.4. Selection criteria for SRD, in addition to the common preselection requirements as shown in Table 7.1.

Variable	SRD-low	SRD-high
$ \Delta\phi(\text{jet}^{0,1,2}, \mathbf{p}_T^{\text{miss}}) $		$> 0.4$
$N_{b-\text{jet}}$		$\geq 2$
$\Delta R(b, b)$		$> 0.8$
$p_T^{0,b} + p_T^{1,b}$	$> 300$ GeV	$> 400$ GeV
$\tau$ -veto		yes
$p_T^1$		$> 150$ GeV
$p_T^3$	$> 100$ GeV	$> 80$ GeV
$p_T^4$		$> 60$ GeV
$m_T^{b,\text{min}}$	$> 250$ GeV	$> 350$ GeV
$m_T^{b,\text{max}}$	$> 300$ GeV	$> 450$ GeV

#### 7.1.4. SRE

SRE is designed for a model for which the tops are highly boosted. Such signatures can either come from direct stop pair production with a very high

stop mass, or in the gluino-mediated compressed-stop scenario with large  $m_{\tilde{g}} - m_{\tilde{t}_1}$ . The benchmark for this signal region is a model where  $(m_{\tilde{g}}, m_{\tilde{t}_1}, m_{\tilde{\chi}_1^0}) = (1700, 400, 395)$  GeV. Due to the large boost, the top daughters are more collimated compared to typical topology expected in Signal Region A. Compared to direct stop pair production with  $m_{\tilde{t}_1} = 800$  GeV and  $m_{\tilde{\chi}_1^0} = 1$  GeV, the  $\Delta R$  separation between the  $W$  and the bottom quark tends to be smaller. This is shown in Figure 7.2. Therefore, anti- $k_t$   $R = 0.8$  reclustered jet collection will be considered as the top candidates instead of  $R = 1.2$  masses in other signal region. Table 7.5 shows the selection criteria for SRE.

TABLE 7.5. Selection criteria for SRE in addition to the common preselection requirements as shown in Table 7.1.

Variable	SRE
$ \Delta\phi(\text{jet}^{0,1,2}, \mathbf{p}_T^{\text{miss}}) $	$> 0.4$
$N_{b-\text{jet}}$	$\geq 2$
$m_{\text{jet}, R=0.8}^0$	$> 120$ GeV
$m_{\text{jet}, R=0.8}^1$	$> 80$ GeV
$m_T^{b,\text{min}}$	$> 200$ GeV
$E_T^{\text{miss}}$	$> 550$ GeV
$H_T$	$> 800$ GeV
$E_T^{\text{miss}}/\sqrt{H_T}$	$> 18\sqrt{\text{GeV}}$

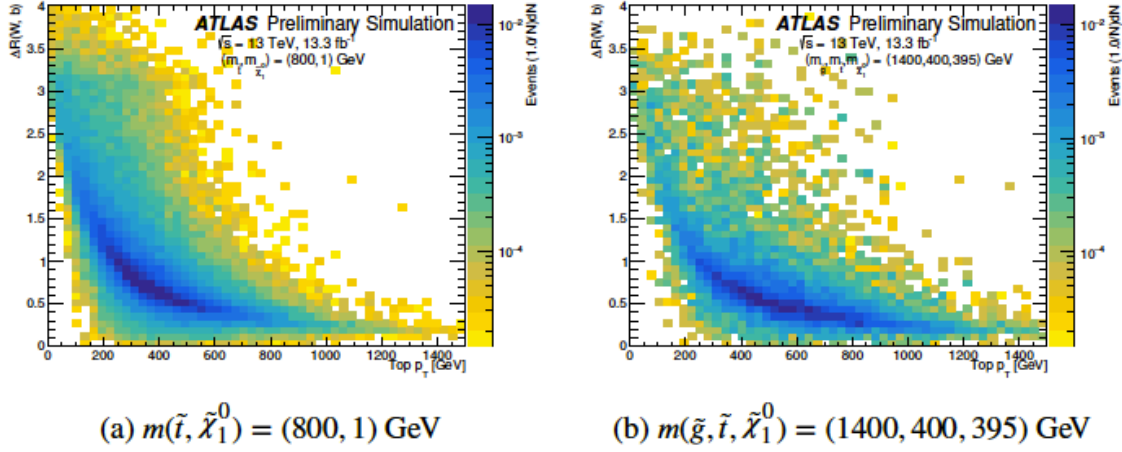


FIGURE 7.2. The true  $\Delta R$  between the  $W$  and the  $b$ -quark vs. the truth top  $p_T$  for (a) SRA and (b) SRE. The common preselection criteria are applied with the exception of the  $b$ -jet requirement.

## 7.2. Background Estimation

### 7.2.1. $Z + \text{jets}$

The  $Z \rightarrow \nu\nu + \text{jets}$  background becomes more relevant as the  $E_T^{\text{miss}}$  requirement is tightened. A possible way to estimate the  $Z \rightarrow \nu\nu$  background is by using a  $Z \rightarrow \ell\ell + \text{jets}$  control sample. The latter channel has the advantage of an easier selection of pure samples in terms of non- $Z$  background, but it is characterized by a lower branching fraction than the background that it is trying to estimate due to the axial-vector couplings of the charged leptons to the  $Z$ . This becomes particularly problematic when estimating the background for events with large  $Z$   $p_T$  where the number of expected events becomes very small. In the current analysis the number of  $Z + \text{jets}$  events is reduced by the  $E_T^{\text{miss}}$  selection, the high jet multiplicity and the requirement for 2  $b$ -tagged jets.

### 7.2.1.1. Control Region

A control region is designed for TT and TW in SRA and SRB and for T0 in SRA and SRB, as well as for SRD and SRE. A CR for SRC was not developed since there is negligible background from  $Z + \text{jets}$ . A summary of the CR selections can be found in Table 7.6 and the lepton triggers used in the analysis are shown in Table 7.7.

TABLE 7.6. Selection criteria for the  $Z + \text{jets}$  control regions used to estimate the  $Z + \text{jets}$  background contributions in the signal regions.

Selection	CRZAB-TT-TW	CRZAB-T0	CRZD	CRZE
Trigger	electron or muon			
$N_\ell$	2, opposite charge, same flavour			
$p_T^\ell$	$> 28 \text{ GeV}$			
$m_{\ell\ell}$	$[86,96] \text{ GeV}$			
$N_{\text{jet}}$	$\geq 4$			
$p_T^0, p_T^1, p_T^2, p_T^3$	$80, 80, 40, 40 \text{ GeV}$			
$E_T^{\text{miss}}$	$< 50 \text{ GeV}$			
$E_T^{\text{miss}'}$	$> 100 \text{ GeV}$			
$N_{b-\text{jet}}$	$\geq 2$			
$m_{\text{jet}, R=1.2}^0$	$> 120 \text{ GeV}$		-	
$m_{\text{jet}, R=1.2}^1$	$> 60 \text{ GeV}$	$< 60 \text{ GeV}$	-	
$m_T^{b,\text{min}'}$	-		$> 200 \text{ GeV}$	
$m_T^{b,\text{max}'}$	-		$> 200 \text{ GeV}$	-
$H_T$	-			$> 500 \text{ GeV}$

TABLE 7.7. Lepton triggers

Channel	Trigger
<b>Data 2015</b>	
Electron Muon	HLT_e24_lhmedium_L1EM20VH OR HLT_e60_lhmedium OR HLT_e120_lhloose HLT_mu20_iloose_L1MU15 OR HLT_mu50
<b>Data 2016</b>	
Electron Muon	HLT_e26_lhtight_nod0_ivarloose OR HLT_e60_lhmedium_nod0 OR HLT_e140_lhloose_nod0 HLT_mu26_ivarmedium OR HLT_mu50

### 7.2.1.2. Validation Region

Zero-lepton validation regions for  $Z + \text{jets}$  dedicated to the various SRs have been designed, except for SRC as the contribution of  $Z + \text{jets}$  background to that particular SR is negligible. The various selections are summarized in Table 7.8. To avoid overlap with the signal region the  $\Delta R(b, b)$  and/or the  $m_{\text{jet}, R=1.2}^0/m_{\text{jet}, R=0.8}^0$  requirement is reversed. These reversals also help in reducing  $t\bar{t}$  and signal contamination. The signal contamination can be seen in Appendix B.

### 7.2.2. $t\bar{t}$ , $W + \text{jets}$ , and single-top

The  $t\bar{t}$  (CRTX),  $W + \text{jets}$  (CRW), and single-top (CRST) backgrounds contribute to the signal region selections because one lepton from the decay of a  $W$  boson is out of acceptance, is mis-identified as a jet, or is an hadronically decaying  $\tau$ -lepton. The control regions to estimate the normalization to these backgrounds are thus defined by exploiting a one-lepton (electron or muon) selection, making them orthogonal to the SRs. For consistency with the signal regions, the same  $E_T^{\text{miss}}$  triggers are used as in the SR (Table 7.1). In these regions the lepton is counted as a jet for the  $p_T$

TABLE 7.8. Selection criteria for the  $Z$  validation regions used to validate the  $Z$  background estimates in the signal regions.

Selection	VRZAB	VRZD	VRZE
Jet $p_T^0, p_T^1$	$> 80, > 80$ GeV	$> 150, > 80$ GeV	$> 80, > 80$ GeV
$N_{\text{jet}}$	$\geq 4$	$\geq 5$	$\geq 4$
$N_{b-\text{jet}}$		$\geq 2$	
$\tau$ -veto	yes		no
$m_T^{b,\min}$		$> 200$ GeV	
$m_{\text{jet}, R=1.2}^0$	$< 120$ GeV		-
$\Delta R(b, b)$	$< 1.0$	$< 0.8$	$< 1.0$
$m_T^{b,\max}$	-	$> 200$ GeV	-
$H_T$		-	$> 500$ GeV
$E_T^{\text{miss}} / \sqrt{H_T}$		-	$> 14 \sqrt{\text{GeV}}$
$m_{\text{jet}, R=0.8}^0$		-	$< 120$ GeV

requirements and the jet reclustering but not for the QCD cleaning selections. The top control region is further divided to match the various signal regions. A specially designed top control region is used for SRC using similar ISR and recursive jigsaw methods.

The three sets of CRs (with multiple CRTs) are mutually exclusive. The requirements on the number of b-jets and on  $m_{\text{jet},R=1.2}^0$  ensures that CRW is orthogonal with CRT and CRST. The selection on  $\Delta R(b_{0,1}, \ell)_{\min}$ , defined as the minimum  $\Delta R$  between the two jets with the highest  $b$ -tag weight and the selected lepton, ensures the orthogonality of CRT and CRST. In CRST the requirement on the  $\Delta R$  of the two leading-weight  $b$ -jets is necessary to reject a large part of the remaining  $t\bar{t}$  background.

The selections for CRW and CRST are shown in Table 7.13.

#### 7.2.2.1. $t\bar{t}$ Control Region

Table 7.9 show the definitions of the various top control regions. SRA and SRB each have a set of three orthogonal control regions defined by the top candidate categories. Additionally, control regions are designed for SRC, SRD and SRE. Figure 7.3 shows the distributions of some of the discriminating variables in the top control regions.

The control region for SRC is designed using the same sensitive variables as the SRC definition to mimic the signal regions as close as possible while maintaining a high purity of the dominant background semi-leptonic  $t\bar{t}$ . A cut of  $m_T(\ell, E_T^{\text{miss}}) < 80 \text{ GeV}$

is added to remove signal contamination and a  $\Delta R(b_{0,1}, \ell)_{\min} < 2.0$  cut is added to increase purity and ensure orthogonality to CRW. Requirements for CRTC are shown in Table 7.10.

TABLE 7.9. Selection criteria for the  $t\bar{t}$  control regions used to estimate the  $t\bar{t}$  background contributions in the signal regions.

Selection	CRTA-TT	CRTA-TW	CRTA-T0	CRTB-TT	CRTB-TW	CRTB-T0	CRTC	CRTD	CRTE
Trigger					$E_T^{\text{miss}}$				
$N_\ell$					1				
$p_T^\ell$						$> 20 \text{ GeV}$			
$N_{\text{jet}}$					$\geq 4$ (including electron or muon)				
$p_T^0, p_T^1, p_T^2, p_T^3$					$80, 80, 40, 40 \text{ GeV}$				
$N_{b-\text{jet}}$						$\geq 2$			
$ \Delta\phi(\text{jet}^{0,1}, \mathbf{p}_T^{\text{miss}}) $						$> 0.4$			
$ \Delta\phi(\text{jet}^{0,1,2}, \mathbf{p}_T^{\text{miss}}) $					$> 0.4$		-		$> 0.4$
$m_T(\ell, E_T^{\text{miss}})$					$[30, 100] \text{ GeV}$		$< 100 \text{ GeV}$		$[30, 100] \text{ GeV}$
$m_T^{b,\text{min}}$					$> 100 \text{ GeV}$		-		$> 100 \text{ GeV}$
$\Delta R(b, \ell)_{\text{min}}$					$< 1.5$		$< 2.0$		$< 1.5$
$m_{\text{jet}, R=1.2}^0$					$> 120 \text{ GeV}$				-
$m_{\text{jet}, R=1.2}^1$	$> 120 \text{ GeV}$	$[60, 120] \text{ GeV}$	$< 60 \text{ GeV}$	$> 120 \text{ GeV}$	$[60, 120] \text{ GeV}$	$< 60 \text{ GeV}$			-
$m_{\text{jet}, R=0.8}^0$			$> 60 \text{ GeV}$						$> 120 \text{ GeV}$
$m_{\text{jet}, R=0.8}^1$						-			$> 80 \text{ GeV}$
$E_T^{\text{miss}}$	$> 250 \text{ GeV}$	$> 300 \text{ GeV}$	$> 350 \text{ GeV}$			$> 250 \text{ GeV}$			
$\Delta R(b, b)$	$> 1.0$		-		$> 1.2$		-	$> 0.8$	-
$m_T^{b,\text{max}}$		-			$> 200 \text{ GeV}$		-	$> 100 \text{ GeV}$	-
$p_T^1$					-			$> 150 \text{ GeV}$	-
$p_T^3$					-			$> 80 \text{ GeV}$	-
$p_T^{0,b} + p_T^{1,b}$					-			$> 300 \text{ GeV}$	-
$N_{\text{jet}}^S$					-		$\geq 5$		-
$N_{b-\text{tag}}^S$					-		$\geq 1$		-
$p_T^{\text{ISR}}$					-		$> 400 \text{ GeV}$		-
$p_T^{4,S}$					-		$> 40 \text{ GeV}$		-
$H_T$					-			$> 500 \text{ GeV}$	

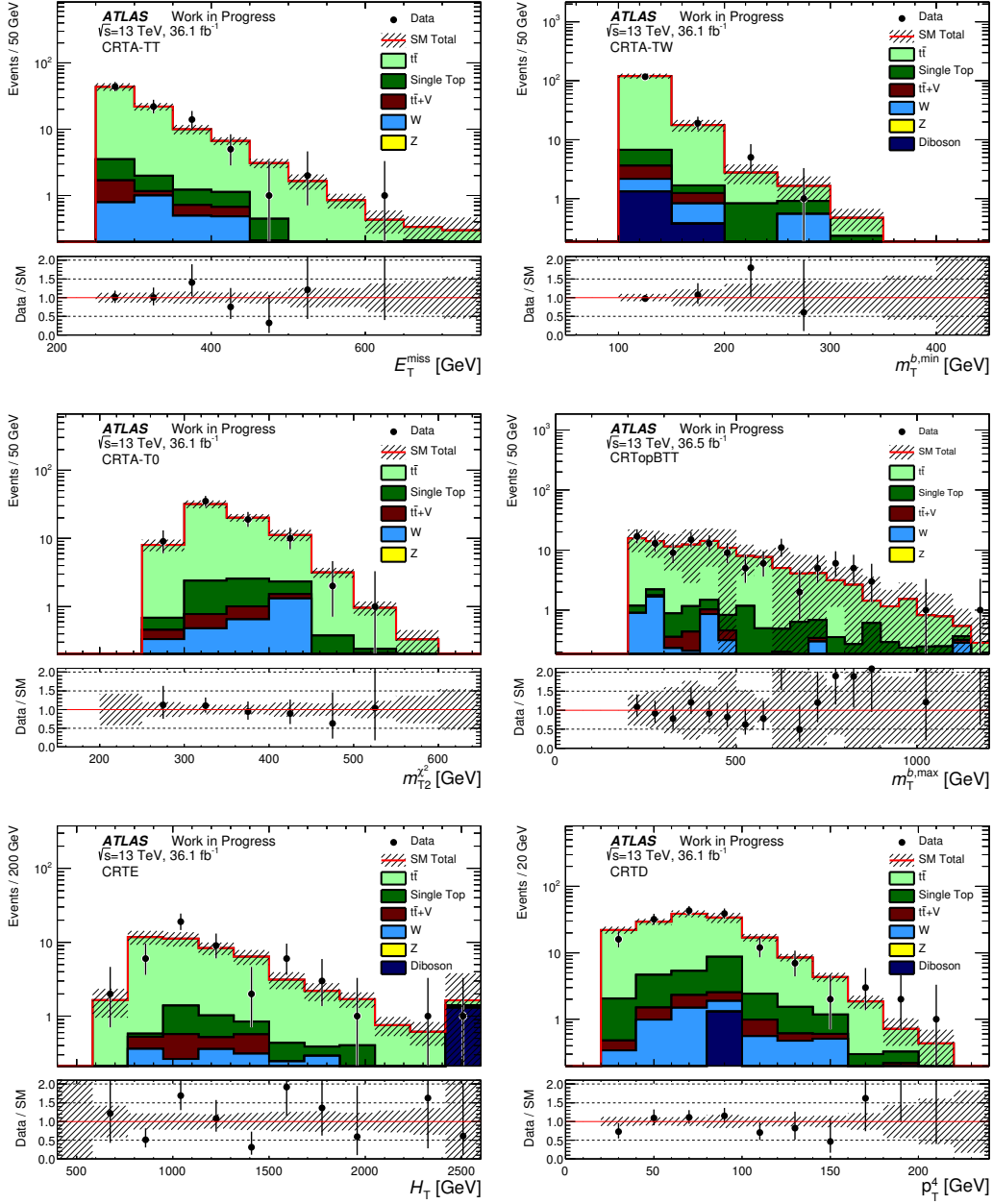


FIGURE 7.3. Postfit distributions for  $36.1 \text{ fb}^{-1}$  of data for various discriminating variables in CRTA, CRTB, CRTD, and CRTE. The ratio between data and MC is shown in the bottom panel. The hashed area in both the top and lower panel represent the uncertainty due to MC statistics and detector systematic uncertainties.

TABLE 7.10. One-lepton  $t\bar{t}$ +ISR control region definitions. The same  $E_T^{\text{miss}}$  triggers as mentioned in Table 7.1 are used.

Variable	1L 1b $t\bar{t}$ +ISR CR
Number of leptons	1
Number of $b$ -jets	$\geq 1$
$m_T(\ell, E_T^{\text{miss}})$	$< 80 \text{ GeV}$
$\Delta R(b_{0,1}, \ell)_{\text{min}}$	$< 2.0$
$N_{\text{jet}}^S$	$\geq 5$
$N_{b\text{-tag}}^S$	$\geq 1$
$p_T^{4,S}$	$> 40 \text{ GeV}$
$p_T^{\text{ISR}}$	$\geq 400$

### 7.2.2.2. $t\bar{t}$ Validation Region

The selections for the  $t\bar{t}$  validation regions in the 0-lepton, two  $b$ -jets channel for the  $t\bar{t}$  background are summarized in Tables 7.11 and 7.12. The same preselection as discussed in Table 7.1 are used.

### 7.2.3. $t\bar{t} + Z$ by $t\bar{t} + \gamma$

The  $t\bar{t}+Z$  background, where the  $Z$  boson decays into neutrinos, is an irreducible background and is increased with respect to the Run 1 analysis. Designing a CR to estimate the  $t\bar{t}+Z$  background by using the charged leptonic  $Z$  boson decays would be favorable. However, such CR is difficult to design due to low statistics and the small branching fraction to leptons. In particular a 2-lepton CR suffers from a large contamination of  $t\bar{t}$  and  $Z + \text{jets}$  processes. For this reason, another data driven approach is followed by building a one-lepton CR for  $t\bar{t}\gamma$  which is a similar process.

TABLE 7.11. Validation region definitions, in addition to the requirements presented in Table 7.1 for VRTA and VRTB.

<b>VRT</b>		<b>TT</b>	<b>TW</b>	<b>T0</b>	
<b>A</b>	$m_{\text{jet}, R=1.2}^0$	$> 120 \text{ GeV}$			
	$m_{\text{jet}, R=1.2}^1$	$> 120 \text{ GeV}$	$60 - 120 \text{ GeV}$	$< 60 \text{ GeV}$	
	$m_T^{b,\text{min}}$	$> 100, < 200 \text{ GeV}$	$> 140, < 200 \text{ GeV}$	$> 160, < 200 \text{ GeV}$	
	Number of $b$ -jets	$\geq 2$			
<b>B</b>	$m_{\text{jet}, R=0.8}^0$	$> 60 \text{ GeV}$			
	$\Delta R(b, b)$	$> 1$	-		
	$E_T^{\text{miss}}$	$> 300 \text{ GeV}$	$> 400 \text{ GeV}$	$> 450 \text{ GeV}$	
<b>C</b>	$\Delta R(b, b)$	$> 1.2$			
	$m_T^{b,\text{max}}$	$> 200 \text{ GeV}$			

A zero-lepton region was considered as a validation region but it was found to have a too low  $t\bar{t}\gamma$  contribution, with  $\gamma+\text{jets}$  being the main contaminant.

The  $t\bar{t} + \gamma$  CR is designed to minimize the differences between the two processes and keep the theoretical uncertainties from the extrapolation of the  $\gamma$  to the  $Z$  low. It requires exactly one photon, exactly one signal lepton (electron or muon, and at least four jets of which at least two are required to be  $b$ -tagged. Moreover, due to the difference in mass between the  $Z$  and the  $\gamma$ , to mimic the  $Z \rightarrow \nu\nu$  decay, the highest  $p_T$  photon is required to have  $p_T > 150 \text{ GeV}$ .

Unlike the CRTs, CRW, and CRST one-lepton control regions the lepton is not treated as a jet and unlike the CRZs the leptons are not removed from the  $E_T^{\text{miss}}$

TABLE 7.12. Summary of the selection for the 0-lepton top validation region for VRTC, VRTD and VRTE, in addition to the requirements presented in Table 7.1.

	VRTC	VRTD	VRTE
$m_T^{b,\min}$	-	$> 100, < 200$ GeV	
Number of jets	$\geq 4$	$\geq 5$	$\geq 4$
Number of $b$ -jets	$\geq 1$	$\geq 2$	
$N_{\text{jet}}^S$	$\geq 4$		-
$N_{b-\text{jet}}^S$	$\geq 1$		-
$p_{T,b}^{0,S}$	$\geq 40$ GeV		-
$p_T^{4,S}$	$> 40$ GeV		-
$p_T^{\text{ISR}}$	$\geq 400$ GeV		-
$m_S$	$> 100$ GeV		-
$m_V/m_S$	$< 0.6$		-
$\Delta\phi(\text{ISR}, \mathbf{p}_T^{\text{miss}})$	$< 3.00$		-
$\Delta R(b, b)$	-	$> 0.8$	-
$m_T^{b,\max}$	-	$> 300$ GeV	-
jet $p_T^1$	-	$> 150$ GeV	-
jet $p_T^3$	-	$> 80$ GeV	-
b-jet $p_T^0 + p_T^1$	-	$> 300$ GeV	-
Jet multiplicity	$\geq 4$	$\geq 5$	$\geq 4$
$\tau$ -veto	-	yes	-
$m_{\text{jet}, R=0.8}^0$		-	$> 120$ GeV
$m_{\text{jet}, R=0.8}^1$		-	$> 80$ GeV

calculation. Instead, the photon is used to model the  $E_T^{\text{miss}}$  since the  $E_T^{\text{miss}}$  from  $t\bar{t} + Z$  in the SR originates mostly from the neutrino decay of the  $Z$ .

TABLE 7.13. Selection criteria for the common  $W + \text{jets}$ , single-top, and  $t\bar{t} + \gamma$  control-region definitions.

Selection	CRW	CRST	CRTTGamma
Trigger		$E_T^{\text{miss}}$	electron or muon
$N_\ell$		1	
$p_T^\ell$		$> 20 \text{ GeV}$	$> 28 \text{ GeV}$
$N_\gamma$		-	1
$p_T^\gamma$		-	$> 150 \text{ GeV}$
$N_{\text{jet}}$	$\geq 4$ (including electron or muon)		$\geq 4$
$p_T^0, p_T^1, p_T^2, p_T^3$		80, 80, 40, 40 GeV	
$N_{b-\text{jet}}$	1		$\geq 2$
$ \Delta\phi(\text{jet}^{0,1}, \mathbf{p}_T^{\text{miss}}) $		$> 0.4$	-
$m_T(\ell, E_T^{\text{miss}})$		[30, 100] GeV	-
$\Delta R(b, \ell)_{\min}$		$> 2.0$	-
$E_T^{\text{miss}}$		$> 250 \text{ GeV}$	-
$\Delta R(b, b)$	-	$> 1.5$	-
$m_{\text{jet}, R=1.2}^0$	$< 60 \text{ GeV}$	$> 120 \text{ GeV}$	-
$m_T^{b,\min}$	-	$> 200 \text{ GeV}$	-

#### 7.2.4. QCD multi-jet and all-hadronic $t\bar{t}$

The background from the production of multijet events and all-hadronic  $t\bar{t}$  events is estimated with the jet smearing method. The main assumption of the jet smearing method is that the QCD background is dominated by the mis-measurement of multiple jets. The term *mis-measurement* refers to cases in which the hadronization

of partons is not fully reconstructed by ATLAS and cases in which the hadronization (particularly for heavy-flavor quarks) produces real  $E_T^{\text{miss}}$  in the form of neutrinos.

The attributed sources of mis-measurement which are taken into account by the method are the following:

- Hadronic calorimeters are not perfect; there is some limit to granularity of calorimeters therefore they are not able to perfectly measure the energy of all particles.
- Since jets are clusters of showering particles it is possible that not all of these particles can be contained within the jet radius. Some of the showering particles may be lost due to interacting with non-detector material. Additionally background particles from various different sources may enter into a jet cone, although this effect is reduced by cosmic background vetos and the overlap removal of other jets, photons, electrons and muons.
- Not all jets are fully contained within the calorimeter systems, if a jet has large amounts of energy it can punch through to the muon system and potentially large amounts of the energy can be lost. This is one such source of the non-Gaussian part of the jet response; this effect always gives lost energy rather than an overestimation of the energy.
- Jets that are close to areas of large amounts of dead material are vetoed, however there are still regions with small amounts of dead material in the calorimeters which can cause particles to deposit their energy. The sources of dead material include damaged or inactive parts of the detector, services for

running electronics to the detector and various non-instrumented region from the support structure of ATLAS.

- In decays of heavy flavor quarks, particularly those of  $b$ -quarks, real missing energy can be present from neutrinos. Typically:  $\sim 76\%$  of  $b$ -quark decays will be hadronic (including hadronic tau decays); leaving 12% of decays with muons and muon neutrinos; and 12% of decays with electrons and electron neutrinos. The decays involving neutrinos will carry a fraction of the jet energy with them, this gives a larger non-Gaussian tail in the case of b-tagged jets.

The recommended procedure is followed and both control regions and validation regions were designed.

### 7.3. Systematic Uncertainties

Systematic uncertainties are associated with the predictions of all background components and the expected signal yields. The systematic uncertainties can be categorized into two sources: experimental and theoretical uncertainties. These systematic uncertainties can impact the expected event yields in the control and signal region as well as the transfer factors used when extrapolating the background expectation from the control to the signal region.

Jet Energy Scale (JES) and Jet Energy Resolution (JER): The two main uncertainties for jets are uncertainties affecting the JES calibration and the JER. The final jet energy calibration generally referred as JES is a correction relating the calorimeter’s response to the true jet energy. The effect of the JES

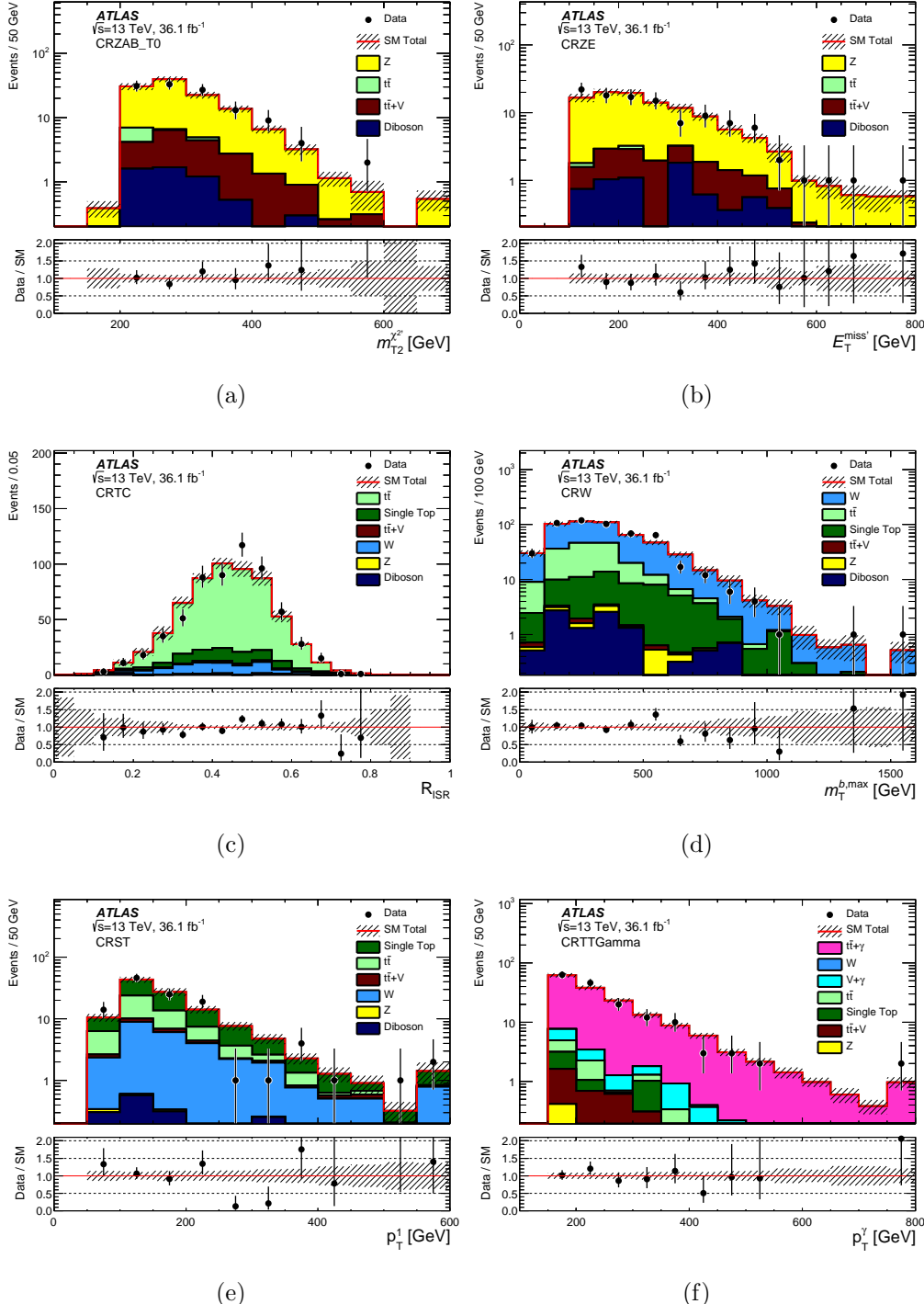


FIGURE 7.4. Distributions of (a)  $m_{\text{T}2}^{\chi^2'}$  in CRZAB-T0, (b)  $E_{\text{T}}^{\text{miss}'}$  in CRZE, (c)  $R_{\text{ISR}}$  in CRTC, (d)  $m_{\text{T}}^{b,\text{max}}$  in CRW, (e) the transverse momentum of the second-leading- $p_{\text{T}}$  jet in CRST, and (f) the photon  $p_{\text{T}}$  in CRTTGamma. The stacked histograms show the SM prediction, normalized using scale factors derived from the simultaneous fit to all backgrounds. The “Data/SM” plots show the ratio of data events to the total SM prediction. The hatched uncertainty band around the SM prediction and in the ratio plot illustrates the combination of MC statistical and detector-related systematic uncertainties. The rightmost bin includes overflow events.

and JER uncertainties on the background estimates in the signal regions can reach 17%. In signal the JER uncertainty ranges from 3% to 6%, and the JES uncertainty ranges from 2% to 5.7%.

*b*-tagging: The *b*-tagging uncertainty has large contribution to both signal and backgrounds because of the two *b*-tagged jets requirement. The uncertainty in the *b*-tagging efficiency is not more than 9%.

$E_T^{\text{miss}}$  Soft-term Resolution and Scale: The uncertainty in the soft term of the  $E_T^{\text{miss}}$  is most significant in SRC5 at 15%.

Lepton efficiencies: Lepton reconstruction and identification efficiencies have contributions to the backgrounds. For electrons, the uncertainties originate from the e/gamma resolution and scale and from the electron reconstruction efficiency. Similarly, for muons the uncertainties originate from the muon resolution and reconstruction efficiency, the isolation and the momentum scale. The lepton trigger scale factors are also taken into consideration. These have a small impact.

Pileup: The uncertainty due to pileup re-weighting is considered as two-sided variation in the event weights. This contributes up to 14%.

Luminosity: The uncertainty in the combined 2015+2016 integrated luminosity is 3.2%.

Theory uncertainties affecting the background normalization and kinematic distribution shapes largely impact the background prediction in the signal regions, as they directly affect the background normalization and acceptance times efficiency. If a background normalization is determined by making use of dedicated control regions,

then only systematics affecting the analysis acceptance are relevant. Statistical uncertainties in the evaluation of systematics are neglected in general; where necessary, selection cuts are loosened to make the systematic comparison statistically meaningful.

The theoretical uncertainty in each signal region is evaluated by considering variations with respect to the default settings and choices for the event generation. For each of the variations considered, the systematic uncertainty is estimated as an uncertainty on the so-called transfer factor, that is, the ratio of the predicted yields between the signal region and the  $t\bar{t}$  control region(s).

Theoretical uncertainties in the modeling of the SM background are estimated. For the  $W/Z +$  jets background processes, the modeling uncertainties are estimated using SHERPA samples by varying the renormalization and factorization scales, and the merging and resummation scales (each varied up and down by a factor of two). PDF uncertainties were found to have a negligible impact. The resulting impact on the total background yields from the  $Z +$  jets theoretical uncertainties is up to 3% while the uncertainties from the  $W +$  jets sample variations are less than 3%.

Theoretical uncertainties in the modeling of the SM background are estimated. For the  $W/Z +$  jets background processes, the modeling uncertainties are estimated using SHERPA samples by varying the renormalization and factorization scales, and the merging and resummation scales (each varied up and down by a factor of two). PDF uncertainties were found to have a negligible impact. The resulting impact on the total background yields from the  $Z +$  jets theoretical uncertainties is up to

3% while the uncertainties from the  $W +$  jets sample variations are less than 3%. For the  $t\bar{t}$  background, uncertainties are estimated from the comparison of different matrix-element calculations, the choice of parton-showering model and the emission of additional partons in the initial and final states. The largest impact of the  $t\bar{t}$  theory systematic uncertainties on the total background yields arises for SRC and it varies from 11% to 71% by tightening the  $R_{\text{ISR}}$  requirement. For the  $t\bar{t}+W/Z$  background, the theoretical uncertainty is estimated through variations, in both  $t\bar{t}+W/Z$  and  $t\bar{t}\gamma$  MC simulation, including the choice of renormalization and factorization scales, the choice of PDF, as well as a comparison between generators, resulting in a maximum uncertainty of 2% in SRA-TT. The single-top background is dominated by the  $Wt$  subprocess. Uncertainties are estimated for the choice of parton-showering model (PYTHIA vs HERWIG++) and for the emission of additional partons in the initial- and final-state radiation. A 30% uncertainty is assigned to the single-top background estimate to account for the effect of interference between single-top-quark and  $t\bar{t}$  production. This uncertainty is estimated by comparing yields in the signal and control regions for a sample that includes resonant and non-resonant  $WW+bb$  production with the sum of the yields of resonant  $t\bar{t}$  and single-top+ $b$  production. The final single-top uncertainty relative to the total background estimate is up to 12%.

#### 7.4. Fitting Procedure

The SM backgrounds in each SR are estimated with a profile likelihood fit using the observed number of events in the CRs. The correlations in the systematic uncertainties that are common between SRs and CRs are treated as nuisance parameters in the fit and are modeled by Gaussian probability density functions. A

MC sample	Fitted scale factor
$t\bar{t}$ (SRA\_TT)	$1.173 \pm 0.146$
$t\bar{t}$ (SRA\_TW)	$1.138 \pm 0.112$
$t\bar{t}$ (SRA\_T0)	$0.898 \pm 0.121$
$t\bar{t}$ (SRB\_TT)	$1.202 \pm 0.156$
$t\bar{t}$ (SRB\_TW)	$0.969 \pm 0.0681$
$t\bar{t}$ (SRB\_T0)	$0.924 \pm 0.0525$
$t\bar{t}$ (SRC)	$0.707 \pm 0.0498$
$t\bar{t}$ (SRD)	$0.945 \pm 0.103$
$t\bar{t}$ (SRE)	$1.012 \pm 0.180$
$W + \text{jets}$	$1.267 \pm 0.146$
$Z + \text{jets}$ (SRA,B TT and TW)	$1.170 \pm 0.238$
$Z + \text{jets}$ (SRA,B T0)	$1.131 \pm 0.144$
$Z + \text{jets}$ (SRD)	$1.035 \pm 0.146$
$Z + \text{jets}$ (SRE)	$1.185 \pm 0.152$
Single top	$1.166 \pm 0.390$
$t\bar{t}\gamma$	$1.290 \pm 0.204$

TABLE 7.14. Fitted scale factors for the MC background samples based on 36.07  $\text{fb}^{-1}$  of data.

normalization factor is then derived from the fit. For backgrounds without a defined CR, contributions are estimated using the cross section.

The fitted scale factors for the backgrounds are summarized in Table 7.14. Tables 7.15, 7.16, and 7.17 show the background and signal yields in simulation before and after the scale factors are applied for SRA, B, C, D, and E.

TABLE 7.15. Observed and expected yields, before and after the fit, for SRA and SRB. The uncertainties include MC statistical uncertainties, detector-related systematic uncertainties, and theoretical uncertainties in the extrapolation from CR to SR.

	SRA-TT	SRA-TW	SRA-T0	SRB-TT	SRB-TW	SRB-T0
Observed	11	9	18	38	53	206
Fitted background events						
Total SM	8.6 $\pm$ 2.1	9.3 $\pm$ 2.2	18.7 $\pm$ 2.7	39.3 $\pm$ 7.6	52.4 $\pm$ 7.4	179 $\pm$ 26
$t\bar{t}$	0.71 $^{+0.91}_{-0.71}$	0.51 $^{+0.55}_{-0.51}$	1.31 $\pm$ 0.64	7.3 $\pm$ 4.3	12.4 $\pm$ 5.9	43 $\pm$ 22
$W + \text{jets}$	0.82 $\pm$ 0.15	0.89 $\pm$ 0.56	2.00 $\pm$ 0.83	7.8 $\pm$ 2.8	4.8 $\pm$ 1.2	25.8 $\pm$ 8.8
$Z + \text{jets}$	2.5 $\pm$ 1.3	4.9 $\pm$ 1.9	9.8 $\pm$ 1.6	9.0 $\pm$ 2.8	16.8 $\pm$ 4.1	60.7 $\pm$ 9.6
$t\bar{t}+W/Z$	3.16 $\pm$ 0.66	1.84 $\pm$ 0.39	2.60 $\pm$ 0.53	9.3 $\pm$ 1.7	10.8 $\pm$ 1.6	20.5 $\pm$ 3.2
Single top	1.20 $\pm$ 0.81	0.70 $\pm$ 0.42	2.9 $\pm$ 1.5	4.2 $\pm$ 2.2	5.9 $\pm$ 2.8	26 $\pm$ 13
Dibosons	--	0.35 $\pm$ 0.26	--	0.13 $\pm$ 0.07	0.60 $\pm$ 0.43	1.04 $\pm$ 0.73
Multijets	0.21 $\pm$ 0.10	0.14 $\pm$ 0.09	0.12 $\pm$ 0.07	1.54 $\pm$ 0.64	1.01 $\pm$ 0.88	1.8 $\pm$ 1.5
Expected events before fit						
Total SM	7.1	7.9	16.3	32.4	46.1	162
$t\bar{t}$	0.60	0.45	1.45	6.1	12.8	47
$W + \text{jets}$	0.65	0.70	1.58	6.1	3.83	20.4
$Z + \text{jets}$	2.15	4.2	8.63	7.7	14.4	53.6
$t\bar{t}+W/Z$	2.46	1.43	2.02	7.3	8.4	15.9
Single top	1.03	0.60	2.5	3.6	5.1	22.4
Dibosons	--	0.35	--	0.13	0.60	1.03
Multijets	0.21	0.14	0.12	1.54	1.01	1.8

TABLE 7.16. Observed and expected yields, before and after the fit, for SRC. The uncertainties include MC statistical uncertainties, detector-related systematic uncertainties, and theoretical uncertainties in the extrapolation from CR to SR.

	SRC1	SRC2	SRC3	SRC4	SRC5
Observed	20	22	22	1	0
Fitted background events					
Total SM	20.6 $\pm$ 6.5	27.6 $\pm$ 4.9	18.9 $\pm$ 3.4	7.7 $\pm$ 1.2	0.91 $\pm$ 0.73
$t\bar{t}$	12.9 $\pm$ 5.9	22.1 $\pm$ 4.3	14.6 $\pm$ 3.2	4.91 $\pm$ 0.97	0.63 $^{+0.70}_{-0.63}$
$W + \text{jets}$	0.80 $\pm$ 0.37	1.93 $\pm$ 0.49	1.91 $\pm$ 0.62	1.93 $\pm$ 0.46	0.21 $\pm$ 0.12
$Z + \text{jets}$	--	--	--	--	--
$t\bar{t}+W/Z$	0.29 $\pm$ 0.16	0.59 $\pm$ 0.38	0.56 $\pm$ 0.31	0.08 $\pm$ 0.08	0.06 $\pm$ 0.02
Single top	1.7 $\pm$ 1.3	1.2 $^{+1.4}_{-1.2}$	1.22 $\pm$ 0.69	0.72 $\pm$ 0.37	--
Dibosons	0.39 $\pm$ 0.33	0.21 $^{+0.23}_{-0.21}$	0.28 $\pm$ 0.18	--	--
Multijets	4.6 $\pm$ 2.4	1.58 $\pm$ 0.77	0.32 $\pm$ 0.17	0.04 $\pm$ 0.02	--
Expected events before fit					
Total SM	25.4	36.0	24.2	9.2	1.1
$t\bar{t}$	18.2	31.2	20.6	7.0	0.89
$W + \text{jets}$	0.64	1.53	1.51	1.53	0.17
$Z + \text{jets}$	--	--	--	--	--
$t\bar{t}+W/Z$	0.22	0.46	0.44	0.07	0.05
Single top	1.44	1.0	1.04	0.62	--
Dibosons	0.39	0.21	0.28	--	--
Multijets	4.6	1.58	0.32	0.04	--

TABLE 7.17. Observed and expected yields, before and after the fit, for SRD and SRE. The uncertainties include MC statistical uncertainties, detector-related systematic uncertainties, and theoretical uncertainties in the extrapolation from CR to SR.

	SRD-low	SRD-high	SRE
Observed	27	11	3
Fitted background events			
Total SM	25.1 $\pm$ 6.2	8.5 $\pm$ 1.5	3.64 $\pm$ 0.79
$t\bar{t}$	3.3 $\pm$ 3.3	0.98 $\pm$ 0.88	0.21 $^{+0.39}_{-0.21}$
$W + \text{jets}$	6.1 $\pm$ 2.9	1.06 $\pm$ 0.34	0.52 $\pm$ 0.27
$Z + \text{jets}$	6.9 $\pm$ 1.5	3.21 $\pm$ 0.62	1.36 $\pm$ 0.25
$t\bar{t}+W/Z$	3.94 $\pm$ 0.85	1.37 $\pm$ 0.32	0.89 $\pm$ 0.19
Single top	3.8 $\pm$ 2.1	1.51 $\pm$ 0.74	0.66 $\pm$ 0.49
Dibosons	--	--	--
Multijets	1.12 $\pm$ 0.37	0.40 $\pm$ 0.15	--
Expected events before fit			
Total SM	22.4	7.7	3.02
$t\bar{t}$	3.4	1.04	0.21
$W + \text{jets}$	4.8	0.84	0.42
$Z + \text{jets}$	6.7	3.10	1.15
$t\bar{t}+W/Z$	3.06	1.07	0.69
Single top	3.3	1.30	0.56
Dibosons	--	--	--
Multijets	1.12	0.40	--

For discovery a p-value is calculated in each SR and subregion independently. For the exclusion fits, the orthogonal subregions of SRA, SRB, and SRC are statistically combined. Then SRA, B, C, D, and E are combined by taking the result with the best expected confidence level. In the case of overlapping signal regions the smallest 95% confidence level is chosen for each model.

## 7.5. Results

The observed yields compared to the background estimates (after applying the scale factors) for all SRs are shown in Tables 7.15, 7.16, and 7.17. No significant excess above the SM expectation is observed in any of the signal regions. As can be seen in Figure 7.5 the yields in the VRs and SRs match the background estimation well. Figures 7.6 shows the postfit, unblinded distribution of some of the most discriminating variables of SRA, SRB, SRC, SRD, and SRE at  $36.07\text{ fb}^{-1}$ . For SRA and SRB the distributions for individual categories are shown. Additionally, the error bands include both MC statistical and all detector systematical uncertainties.

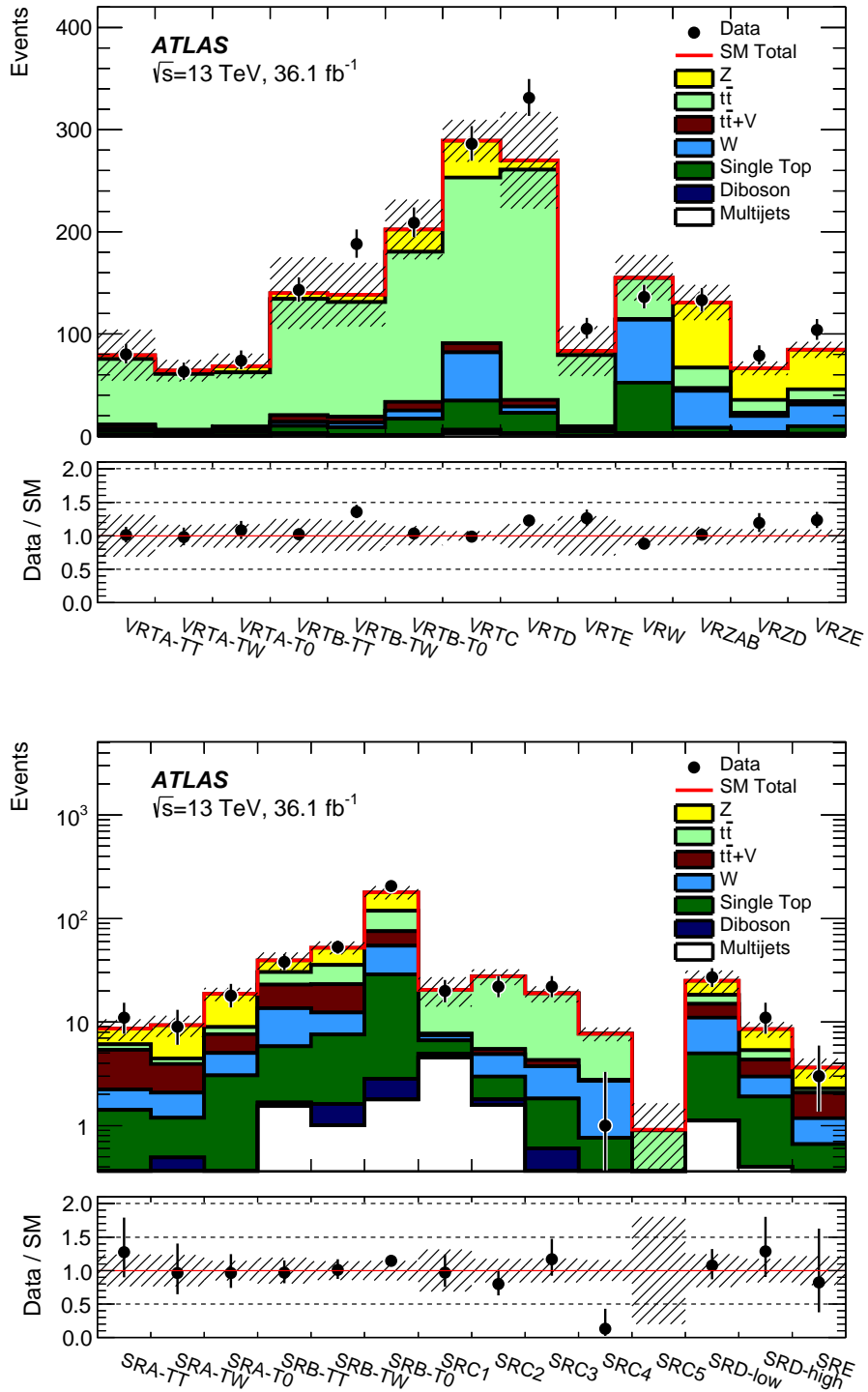


FIGURE 7.5. Final yields for all the validation and signal regions. The stacked histograms show the SM expectation and the hatched uncertainty band around the SM expectation shows the MC statistical and detector-related systematic uncertainties.

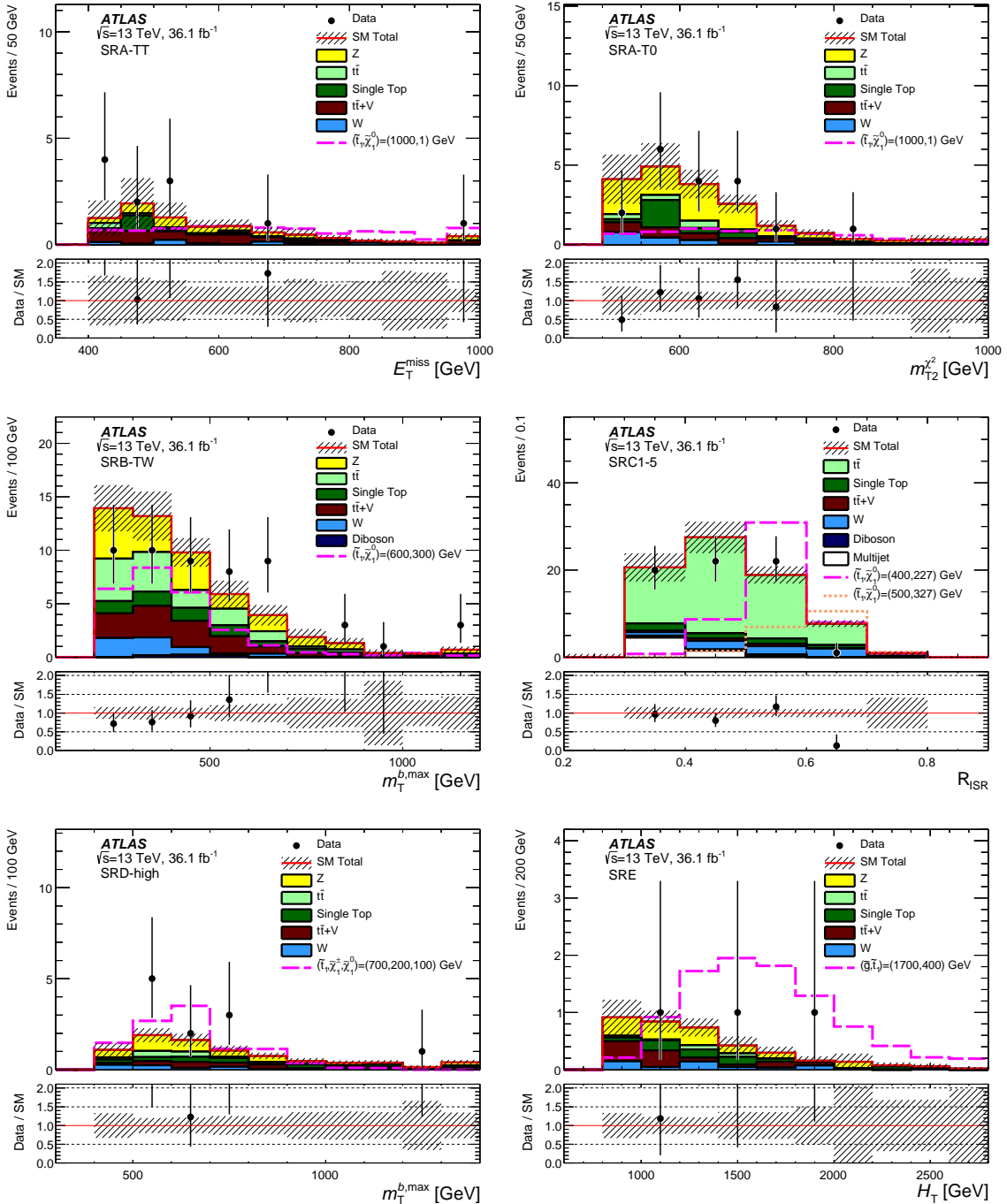


FIGURE 7.6. Distributions of  $E_T^{\text{miss}}$  for SRA-TT,  $m_{T2}^{\chi^2}$  for SRA-T0,  $m_T^{b,\text{max}}$  for SRB-TW,  $R_{\text{ISR}}$  for SRC1-5,  $m_T^{b,\text{max}}$  for SRD-high and  $H_T$  for SRE after the likelihood fit. The stacked histograms show the SM prediction and the hatched uncertainty band around the SM prediction shows the MC statistical and detector-related systematic uncertainties. For each variable, the distribution for a representative signal point is shown.

When no statistical excess is observed the cause may be the absence of signal, but can also be due to a downward fluctuation in the background. In the case of a downward fluctuation the limit may be much better than the actual experimental sensitivity. To account for this the CL<sub>S</sub> method[45, 46] along with the asymptotic formulae[43] can be employed, where the probability is normalized to background-only probability. In this case the limits are more conservative.

There are two types of limits that are evaluated:

- Expected limits: obtained by setting the nominal event yield in each SR to the background expectation. The  $\pm 1\sigma$  contours are evaluated using the  $\pm 1\sigma$  uncertainties of the background estimates.
- Observed limits: obtained by using the actual event yield and the  $\pm 1\sigma$  contours are evaluated by varying the signal cross section by the  $\pm 1\sigma$  of the theory uncertainties. If the actual event yield is larger than the expected yield then the limit is weaker.

The results of the discovery fit for 36.07 fb<sup>-1</sup> are summarized by the model-independent upper limits, as evaluated with asymptotics and shown in Table 7.18. In the asymptotic case, the calculator does not return a p0 value when the number of observed events is less than expected. The table shows the 95% confidence level upper limits on the visible cross section ( $\langle \epsilon\sigma \rangle$ , the detector acceptance multiplied by the efficiency), the number of signal events, the confidence level for the background-only hypothesis, and the discover p-values. The smaller the p-value the more likely for the background-only hypothesis to be incorrect. When the number of observed events are smaller than predicted a p-value of 0.50 is assigned. The smallest p-values

are 0.19, 0.24, 0.27, and 0.29 for SRB-T0, SRD-high, SRA-TT, and SRC3. These values are too large to reject the background-only theory<sup>2</sup>.

TABLE 7.18. Left to right: 95% CL upper limits on the average visible cross section ( $\langle\sigma A\epsilon\rangle_{\text{obs}}^{95}$ ) where the average comes from possibly multiple production channels and on the number of signal events ( $S_{\text{obs}}^{95}$ ). The third column ( $S_{\text{exp}}^{95}$ ) shows the 95% CL upper limit on the number of signal events, given the expected number (and  $\pm 1\sigma$  excursions of the expected number) of background events. The two last columns indicate the  $\text{CL}_B$  value, i.e. the confidence level observed for the background-only hypothesis, and the discovery  $p$ -value ( $p$ ) and the corresponding significance ( $z$ ).

Signal channel	$\langle\sigma A\epsilon\rangle_{\text{obs}}^{95}$ [fb]	$S_{\text{obs}}^{95}$	$S_{\text{exp}}^{95}$	$\text{CL}_B$	$p$ ( $z$ )
SRA-TT	0.30	11.0	$8.7^{+3.0}_{-1.4}$	0.78	0.23 (0.74)
SRA-TW	0.27	9.6	$9.6^{+2.8}_{-2.1}$	0.50	0.50 (0.00)
SRA-T0	0.31	11.2	$11.5^{+3.8}_{-2.0}$	0.46	0.50 (0.00)
SRB-TT	0.54	19.6	$20.0^{+6.5}_{-4.9}$	0.46	0.50 (0.00)
SRB-TW	0.60	21.7	$21.0^{+7.3}_{-4.3}$	0.54	0.37 (0.33)
SRB-T0	2.19	80	$58^{+23}_{-17}$	0.83	0.13 (1.15)
SRC1	0.42	15.1	$15.8^{+4.8}_{-3.5}$	0.48	0.50 (0.00)
SRC2	0.31	11.2	$13.9^{+5.9}_{-3.6}$	0.24	0.50 (0.00)
SRC3	0.42	15.3	$12.3^{+4.7}_{-3.4}$	0.73	0.27 (0.62)
SRC4	0.10	3.5	$6.7^{+2.8}_{-1.8}$	0.00	0.50 (0.00)
SRC5	0.09	3.2	$3.0^{+1.1}_{-0.1}$	0.23	0.23 (0.74)
SRD-low	0.50	17.9	$16.4^{+6.3}_{-4.0}$	0.62	0.36 (0.35)
SRD-high	0.30	10.9	$8.0^{+3.4}_{-1.3}$	0.79	0.21 (0.79)
SRE	0.17	6.1	$6.4^{+1.4}_{-2.4}$	0.42	0.50 (0.00)

<sup>2</sup> For excluding a signal hypothesis a  $p$ -value greater than 0.05, which corresponds to a 95% confidence level, is used. The standard of a  $5\sigma$  excess for a discovery has a  $p$ -value of  $2.87 \times 10^{-7}$ .

## 7.6. Interpretations

The results have been interpreted in terms of a simplified model and for several pMSSM interpretations.

### 7.6.1. Simplified Model

The exclusion curves for the 100%  $\tilde{t}_1 \rightarrow t\tilde{\chi}_1^0$  br is shown in Figure 7.7. Included in blue are the results from the 8 TeV analysis. The observed and expected limits are shown in red and blue respectively. Assuming a branching fraction of 100% to a top quark and neutralino, stop masses in the range 450-1000 GeV are excluded for neutralino masses below 160 GeV. In the case where the stop mass is close to the top mass plus the neutralino mass, masses between 235-590 GeV are excluded. For a Natural-SUSY inspired mixed grid scenario, where the  $\tilde{t}_1$  decays to a  $t\tilde{\chi}_1^0$  or  $b\tilde{\chi}_1^\pm$  with different branching ratios is shown in Figure 7.8. Finally the SRE results are interpreted for indirect top-squark production through gluino decays in terms of the  $\tilde{t}_1$  vs.  $\tilde{g}$  mass plane with  $\Delta m(\tilde{t}_1, \tilde{\chi}_1^0) = 5$  GeV. Gluino masses up to  $m_{\tilde{g}} = 1800$  GeV with  $m_{\tilde{t}_1} < 800$  GeV are excluded as shown in Fig. 7.9.

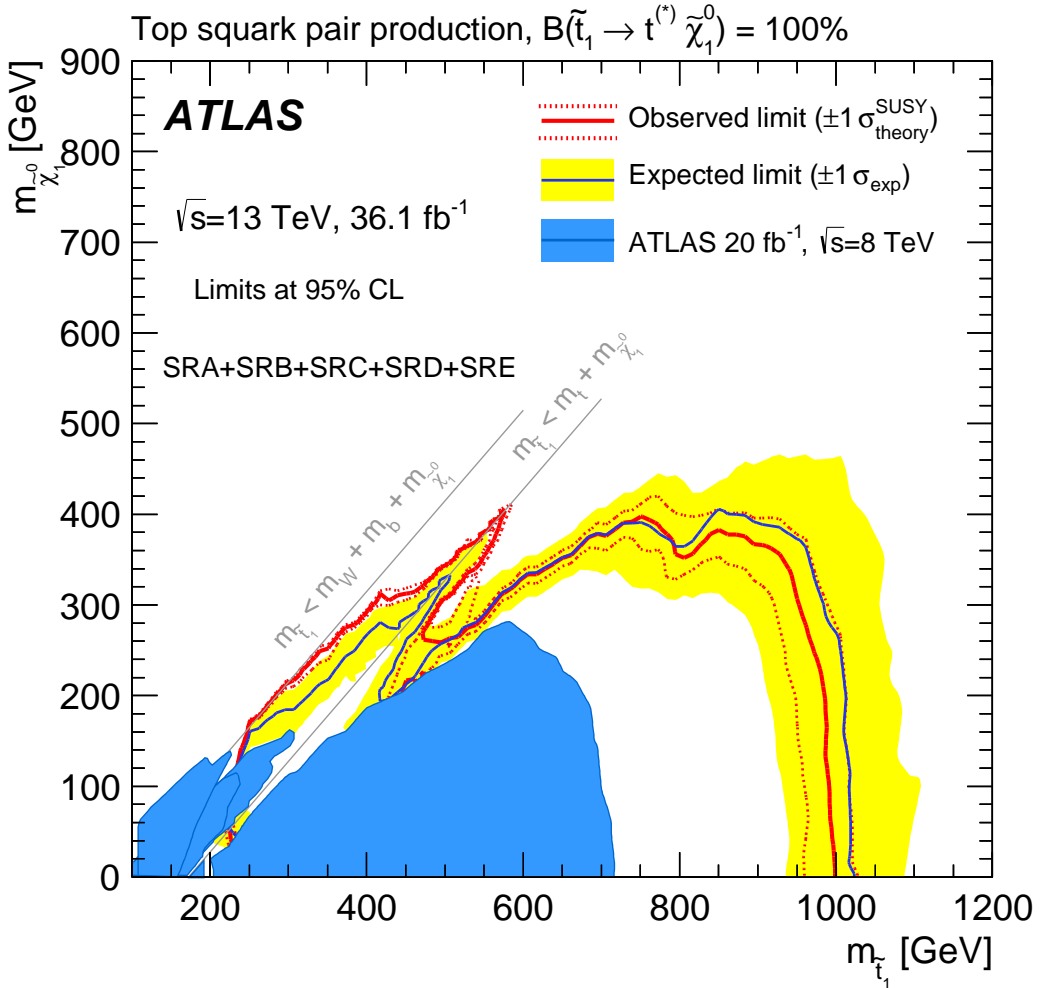


FIGURE 7.7. Observed (red solid line) and expected (blue solid line) exclusion contours at 95% CL as a function of  $\tilde{t}_1$  and  $\tilde{\chi}_1^0$  masses in the scenario where both top squarks decay via  $\tilde{t}_1 \rightarrow t^{(*)}\tilde{\chi}_1^0$ . Masses that are lower than the masses along the lines are excluded. Uncertainty bands corresponding to the  $\pm 1\sigma$  variation on the expected limit (yellow band) and the sensitivity of the observed limit to  $\pm 1\sigma$  variations of the signal theoretical uncertainties (red dotted lines) are also indicated. Observed limits from all third-generation Run-1 searches [47] at  $\sqrt{s} = 8$  TeV centre-of-mass energy are overlaid for comparison in blue.

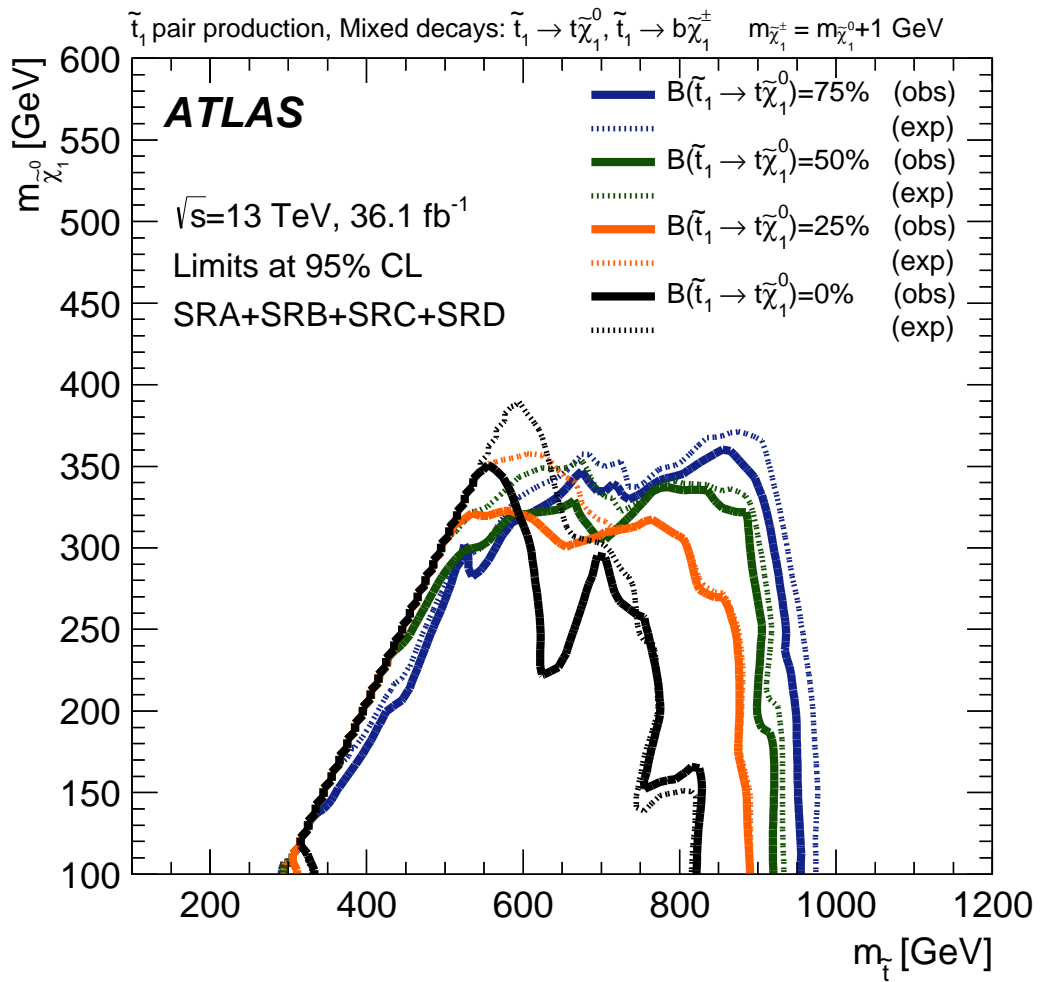


FIGURE 7.8. Observed (solid line) and expected (dashed line) exclusion contours at 95% CL as a function of  $\tilde{t}_1$  and  $\tilde{\chi}_1^0$  masses and branching ratio to  $\tilde{t}_1 \rightarrow t\tilde{\chi}_1^0$  in the Natural SUSY-inspired mixed grid scenario where  $m_{\tilde{\chi}_1^\pm} = m_{\tilde{\chi}_1^0} + 1$  GeV.

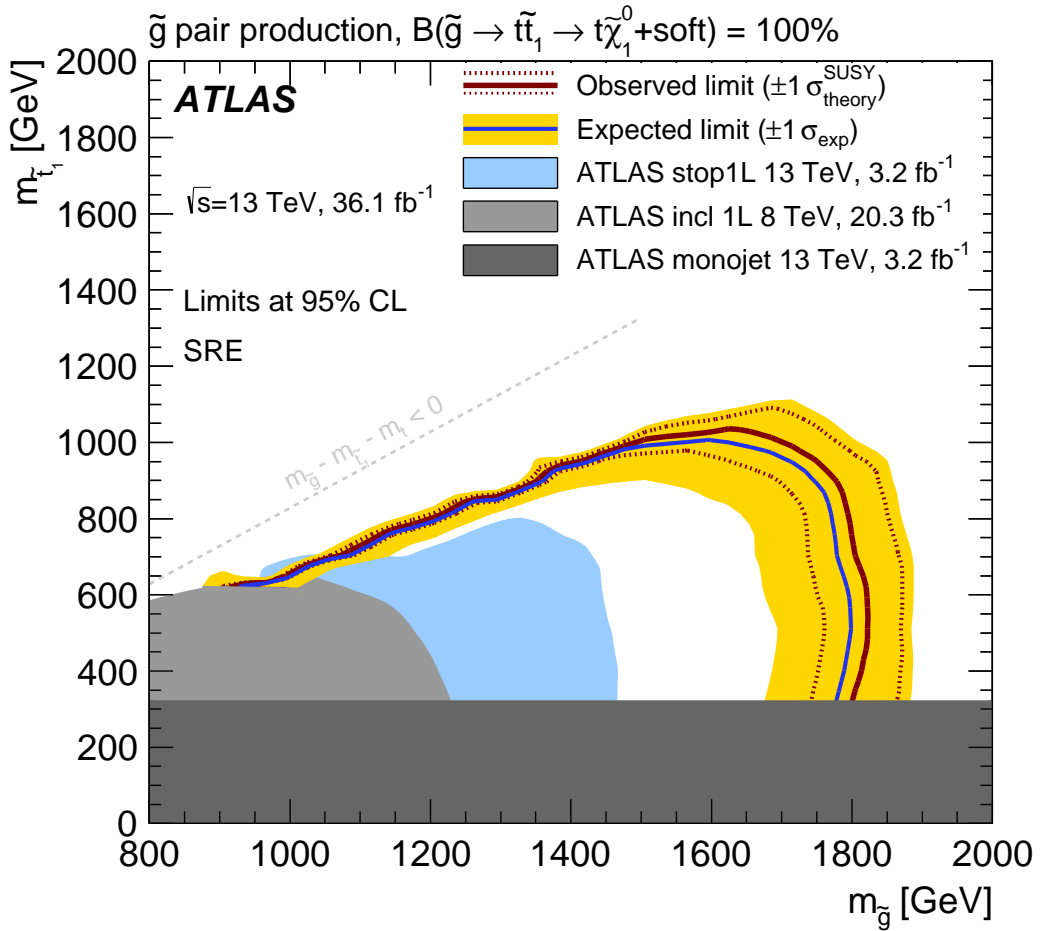


FIGURE 7.9. Observed (red solid line) and expected (blue solid line) exclusion contours at 95% CL as a function of  $\tilde{g}$  and  $\tilde{t}_1$  masses in the scenario where both gluinos decay via  $\tilde{g} \rightarrow t\tilde{t}_1 \rightarrow t\tilde{\chi}_1^0 + \text{soft}$  and  $\Delta m(\tilde{t}_1, \tilde{\chi}_1^0) = 5 \text{ GeV}$ . Uncertainty bands corresponding to the  $\pm 1\sigma$  variation on the expected limit (yellow band) and the sensitivity of the observed limit to  $\pm 1\sigma$  variations of the signal theoretical uncertainties (red dotted lines) are also indicated. Observed limits from previous searches with the ATLAS detector at  $\sqrt{s} = 8$  and  $\sqrt{s} = 13 \text{ TeV}$  are overlaid in grey and blue [70–72].

### 7.6.2. pMSSM

The results have also been interpreted in the context of pMSSM, which is described in 2.7. There are three specific models within pMSSM for which the results have been interpreted:

- Non-asymptotic higgsino: A simplified model motivated by naturalness with a higgsino LSP,  $m_{\tilde{\chi}_1^\pm} = m_{\tilde{\chi}_1^0} + 5$  GeV, and  $m_{\tilde{\chi}_2^0} = m_{\tilde{\chi}_1^0} + 10$  GeV, assumes three sets of branching ratios for the considered decays of  $\tilde{t}_1 \rightarrow t\tilde{\chi}_2^0$ ,  $\tilde{t}_1 \rightarrow t\tilde{\chi}_1^0$ ,  $\tilde{t}_1 \rightarrow b\tilde{\chi}_1^\pm$  [73]. A set of branching ratios with  $\text{BR}(\tilde{t}_1 \rightarrow t\tilde{\chi}_2^0, \tilde{t}_1 \rightarrow t\tilde{\chi}_1^0, \tilde{t}_1 \rightarrow b\tilde{\chi}_1^\pm) = 33\%, 33\%, 33\%$  is considered which is equivalent to a pMSSM model with a mostly left-handed top squark and  $\tan\beta = 60$  (ratio of vacuum expectation values of the two Higgs doublets). Additionally,  $\text{BR}(\tilde{t}_1 \rightarrow t\tilde{\chi}_2^0, \tilde{t}_1 \rightarrow t\tilde{\chi}_1^0, \tilde{t}_1 \rightarrow b\tilde{\chi}_1^\pm) = 45\%, 10\%, 45\%$  and  $\text{BR}(\tilde{t}_1 \rightarrow t\tilde{\chi}_2^0, \tilde{t}_1 \rightarrow t\tilde{\chi}_1^0, \tilde{t}_1 \rightarrow b\tilde{\chi}_1^\pm) = 25\%, 50\%, 25\%$  are assumed.
- Wino NLSP pMSSM: This model is motivated by models with gauge unification at the GUT scale. The LSP is bino-like and has mass  $M_1$  and where the NLSP is wino-like with mass  $M_2$ , while  $M_2 = 2M_1$  and  $m_{\tilde{t}_1} > M_1$  [73]. Limits are set for both positive and negative  $\mu$  (the higgsino mass parameter) as a function of the  $\tilde{t}_1$  and  $\tilde{\chi}_1^0$  masses which can be translated to different  $M_1$  and  $m_{\tilde{q}_{L3}}$ , and are shown in Fig. 7.11. Only bottom and top-squark production are considered in this interpretation. Allowed decays in the top-squark production scenario are  $\tilde{t}_1 \rightarrow t\tilde{\chi}_2^0 \rightarrow h/Z\tilde{\chi}_1^0$ , at a maximum branching ratio of 33%, and  $\tilde{t}_1 \rightarrow b\tilde{\chi}_1^\pm$ . Whether the  $\tilde{\chi}_2^0$  dominantly decays to a  $h$  or  $Z$  is determined by the sign of  $\mu$ . Along the diagonal region, the  $\tilde{t}_1 \rightarrow t\tilde{\chi}_1^0$  decay with 100% BR is also considered. The equivalent decays in bottom-squark production are  $\tilde{b} \rightarrow t\tilde{\chi}_1^\pm$  and  $\tilde{b} \rightarrow b\tilde{\chi}_2^0$ .

- Well-tempered neutralino pMSSM: A model that provides a viable dark matter candidate in which three light neutralinos and a light chargino, which are composed as a mixture of bino and higgsino states, are considered with masses within 50 GeV of the lightest state [74, 75]. The model is designed to satisfy the SM Higgs-boson mass and the dark matter relic density ( $0.10 < \Omega h^2 < 0.12$ , where  $\Omega$  is density parameter and  $h$  is the Planck constant [76]).

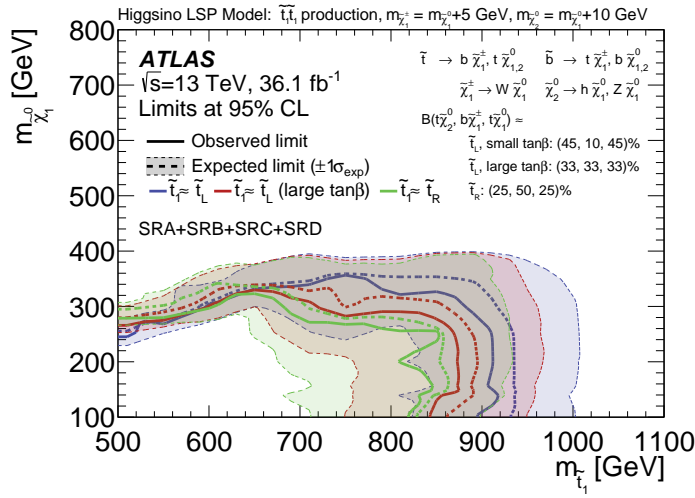


FIGURE 7.10. Observed (solid line) and expected (dashed line) exclusion contours at 95% CL as a function of  $m_{\tilde{t}_1}$  and  $m_{\tilde{\chi}_1^0}$  for the pMSSM-inspired non-asymptotic higgsino simplified model for a small  $\tan\beta$  with  $\text{BR}(\tilde{t}_1 \rightarrow t \tilde{\chi}_2^0, \tilde{t}_1 \rightarrow t \tilde{\chi}_1^0, \tilde{t}_1 \rightarrow b \tilde{\chi}_1^{\pm}) = 45\%, 10\%, 45\%$  (blue), a large  $\tan\beta$  with  $\text{BR}(\tilde{t}_1 \rightarrow t \tilde{\chi}_2^0, \tilde{t}_1 \rightarrow t \tilde{\chi}_1^0, \tilde{t}_1 \rightarrow b \tilde{\chi}_1^{\pm}) = 33\%, 33\%, 33\%$  (red), and a small right-handed top-squark mass parameter with  $\text{BR}(\tilde{t}_1 \rightarrow t \tilde{\chi}_2^0, \tilde{t}_1 \rightarrow t \tilde{\chi}_1^0, \tilde{t}_1 \rightarrow b \tilde{\chi}_1^{\pm}) = 25\%, 50\%, 25\%$  (green) assumption. Uncertainty bands correspond to the  $\pm 1\sigma$  variation on the expected limit.

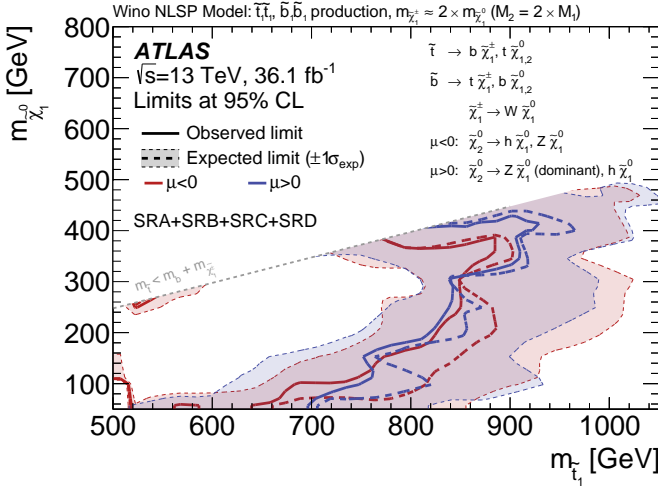


FIGURE 7.11. Observed (solid line) and expected (dashed line) exclusion contours at 95% CL as a function of  $\tilde{t}_1$  and  $\tilde{\chi}_1^0$  masses for the Wino NLSP pMSSM model for both positive (blue) and negative (red) values of  $\mu$ . Uncertainty bands correspond to the  $\pm 1\sigma$  variation on the expected limit.

## 7.7. Outlook

The amount of data that the LHC has produced in Run 2 has exceeded expectations. However, as can be seen in Section 7.13, the rate at which increasing luminosity increases the discovery potential slows with more data. This is due to the increase in background, and as the mass of the stop increases the cross section decreases. There is a need for much more data and the High-Luminosity LHC, as discussed in Section 3.6, will be invaluable for searches in the future and improvements to the trigger system, such as triggering on large-radius jets as the gFEX is designed to do, will also improve chances of discovery.

The CMS experiment also has conducted a search for the all-hadronic decay of the stop, though with some different approaches. For instance the method of

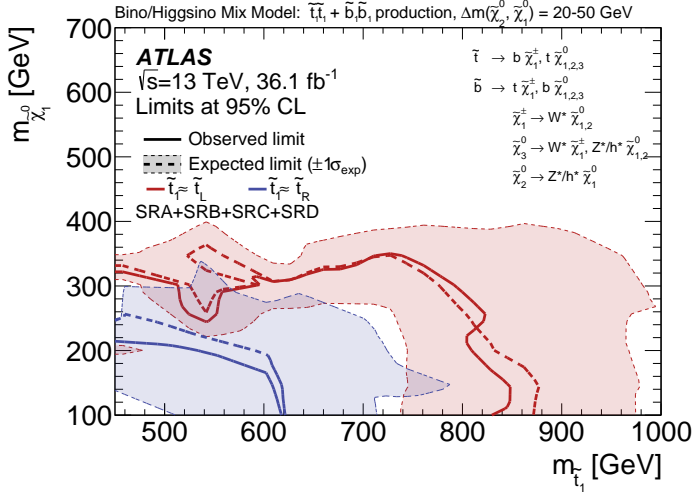


FIGURE 7.12. Observed (solid line) and expected (dashed line) exclusion contours at 95% CL as a function of  $\tilde{t}_1$  and  $\tilde{\chi}_1^0$  masses for the left-handed top-squark mass parameter scan (red) as well as in the right-handed top-squark mass parameter scan (blue) in the well-tempered pMSSM model. Uncertainty bands correspond to the  $\pm 1\sigma$  variation on the expected limit.

identifying top quarks; instead of using mass categories the approach is to identify based on  $p_T$ . For high  $p_T$  top, jets are reclustered with the anti- $k_t$  algorithm with a distance parameter of  $R=0.8$ . Substructure is also required and the tops, and kinematic variables are used for two separate BDTs, one for top quarks and one for  $W$  bosons, which discriminate between signal and background. Intermediate  $p_T$  candidates use the two highest  $b$ -tagged jets and then find a  $W$  boson candidate to form resolved top candidates. Various kinematic variables from these top-tagged jets are then input to a BDT to discriminate signal from background. Stop masses up to 1040 GeV and neutralino masses up to 500 GeV are excluded with this search. The multiple uses of BDTs improved the exclusion, but adds complications to the analysis.

There is also a need to find ways to remove background and improve the analysis, and there is ongoing R&D for the analysis. For example, at the time of this writing

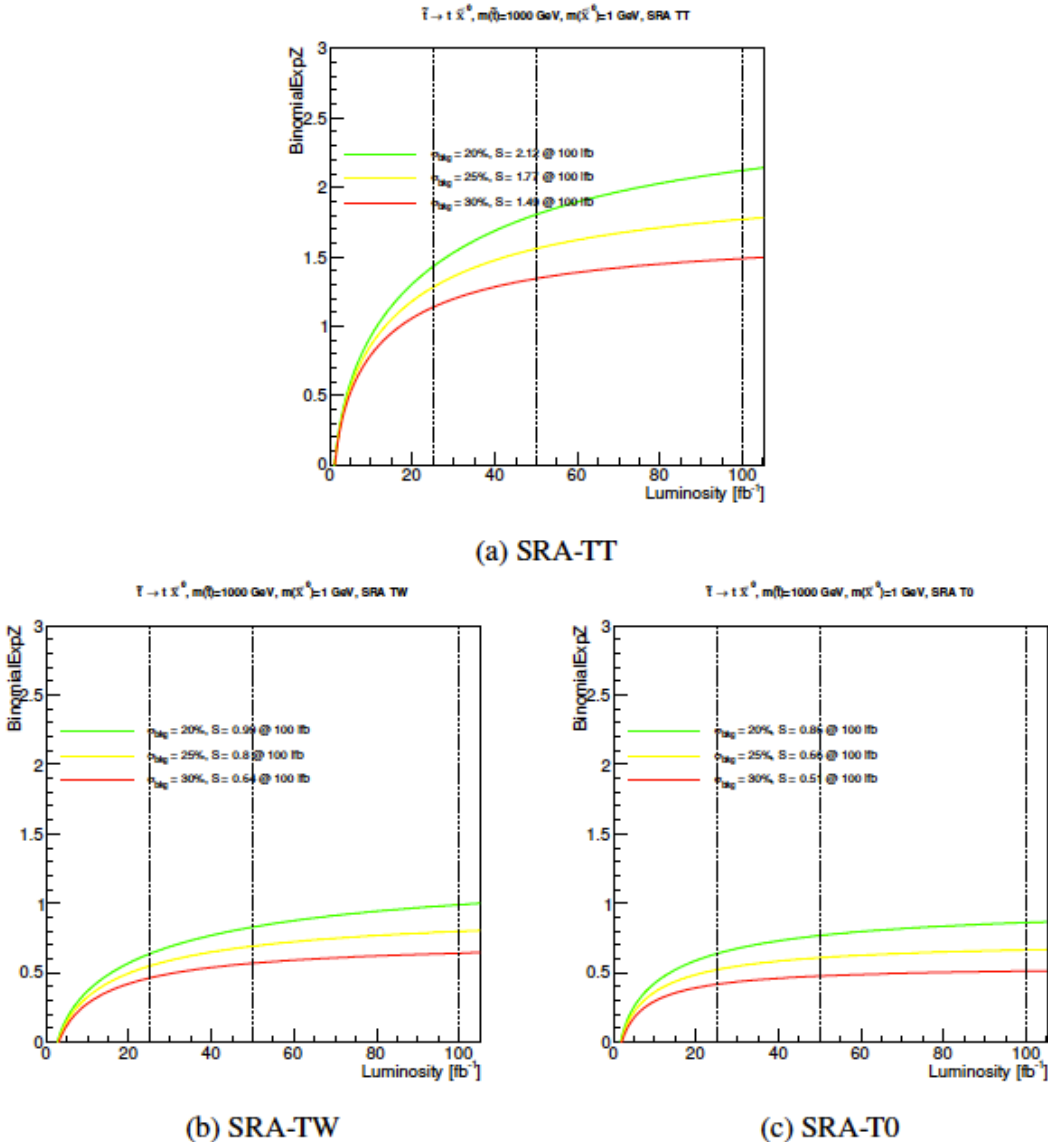


FIGURE 7.13. Signal significant as a function of integrated luminosity for simplified model with  $(m_{\tilde{t}_1}, m_{\tilde{\chi}_1^0}) = (1000, 1)$  GeV and 100%  $\tilde{t}_1 \rightarrow t\tilde{\chi}_1^0$  br for SRA subregions. The color lines represent different levels of background estimate uncertainty.

work to improve  $b$ -jet efficiency as well as calibrating smaller-radius jets, which can help resolve structure in larger radius jets, is being carried out. In addition, it's worthwhile to determine if some new machine learning algorithms can help in the search. For example, jets in the calorimeter can be thought of as an image, so Convolutional Neural Networks (CNNs), which are designed to, for example,

discriminate between specific images and similar ones, which can be useful to optimize signal regions. In this analysis, the cuts used for SRA and SRB were compared to a BDT, and it was found that the BDT used the top masses to improve performance. After the top mass subcategories were employed the cuts matched the performance of the BDT. More advanced algorithms can be used, but can be much more difficult or impossible to decipher what the algorithm is doing. This means that there is a risk of losing the physical interpretation of what the algorithms are doing, and reinterpreting the analysis is more difficult. However, it can at the least provide a metric to compare analysis cuts to what is possible.

## CHAPTER VIII

### CONCLUSIONS

Results from a search for stop production based on integrated luminosity of  $36.1 \text{ fb}^{-1}$  data of  $\sqrt{s} = 13 \text{ TeV}$   $pp$  collisions recorded by the ATLAS experiment at the LHC in 2015 and 2016 are presented. Top squarks are searched for in final states with high- $p_T$  jets and large missing transverse momentum. In this dissertation, the top squark is assumed to decay via  $\tilde{t}_1 \rightarrow t^{(*)}\tilde{\chi}_1^0$  with large or small mass differences between the top squark and the neutralino  $\Delta m(\tilde{t}_1, \tilde{\chi}_1^0)$  and via  $\tilde{t}_1 \rightarrow b\tilde{\chi}_1^\pm$ , where  $m_{\tilde{\chi}_1^\pm} = m_{\tilde{\chi}_1^0} + 1 \text{ GeV}$ . Gluino-mediated  $\tilde{t}_1$  production is studied, in which gluinos decay via  $\tilde{g} \rightarrow t\tilde{t}_1$ , with a small  $\Delta m(\tilde{t}_1, \tilde{\chi}_1^0)$ .

No significant excess above the expected SM background prediction is observed. Exclusion limits at 95% confidence level on the combination of top-squark and LSP mass are derived resulting in the exclusion of top-squark masses in the range 450-950 GeV for  $\tilde{\chi}_1^0$  masses below 160 GeV. For the case where  $m_{\tilde{t}_1} \sim m_t + m_{\tilde{\chi}_1^0}$ , top-squark masses between 235-590 GeV are excluded. In addition, model-independent limits and  $p$ -values for each signal region are reported. Limits that take into account an additional decay of  $\tilde{t}_1 \rightarrow b\tilde{\chi}_1^\pm$  are also set with an exclusion of top-squark masses between 450 and 850 GeV for  $m_{\tilde{\chi}_1^0} < 240 \text{ GeV}$  and  $\text{BR}(\tilde{t}_1 \rightarrow t\tilde{\chi}_1^0) = 50\%$  for  $m_{\tilde{\chi}_1^\pm} = m_{\tilde{\chi}_1^0} + 1 \text{ GeV}$ . Limits are also derived in several pMSSM models, where one model assumes a wino-like NLSP, one assumes a higgsino-like LSP, and the other model is constrained by the dark-matter relic density. Finally, exclusion contours are reported for gluino production where  $m_{\tilde{t}_1} = m_{\tilde{\chi}_1^0} + 5 \text{ GeV}$  resulting in gluino masses

being constraint to be above 1800 GeV for  $\tilde{t}_1$  masses below 800 GeV.

By the end of Run 2 the LHC will have delivered  $\sim 150 \text{ fb}^{-1}$  of data. This is nearly five times the amount of data used in this analysis, which will increase the sensitivity to higher mass stops. There is also ongoing R&D to improve the analysis. Although supersymmetry has not yet been detected, there is still a lot of phase space that will be opened with more data. Discovering supersymmetry would start a new era of particle physics, and if it is not discovered, explanations for the failings of the Standard Model will continue to be investigated.

## APPENDIX A

### STANDARD MC AND DATA CHECKS

The following sections describes basic checks on the MC and data.

#### A.0.1. Dependence of variables on pileup

The purpose of this is to check the analysis dependence on pileup. Ideally there is no dependence. The preselection is the same as in Section 7.1.

These plots demonstrate that the variables used in the analysis do not have a dependence on pileup.

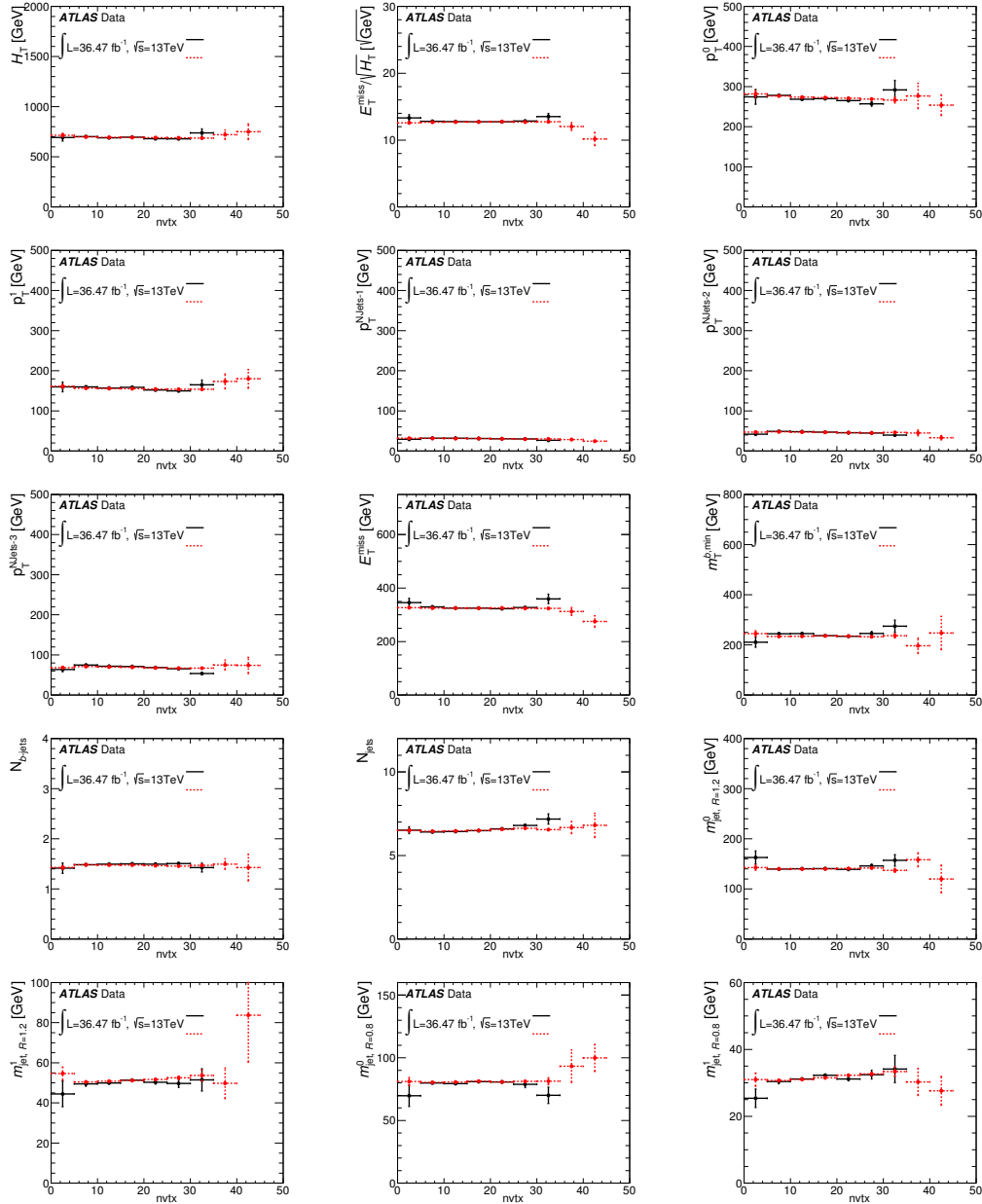


FIGURE A.1. Distribution of various variables in Data and Monte Carlo used as a function of number of vertices.

### A.0.2. Lumi-normalized yields

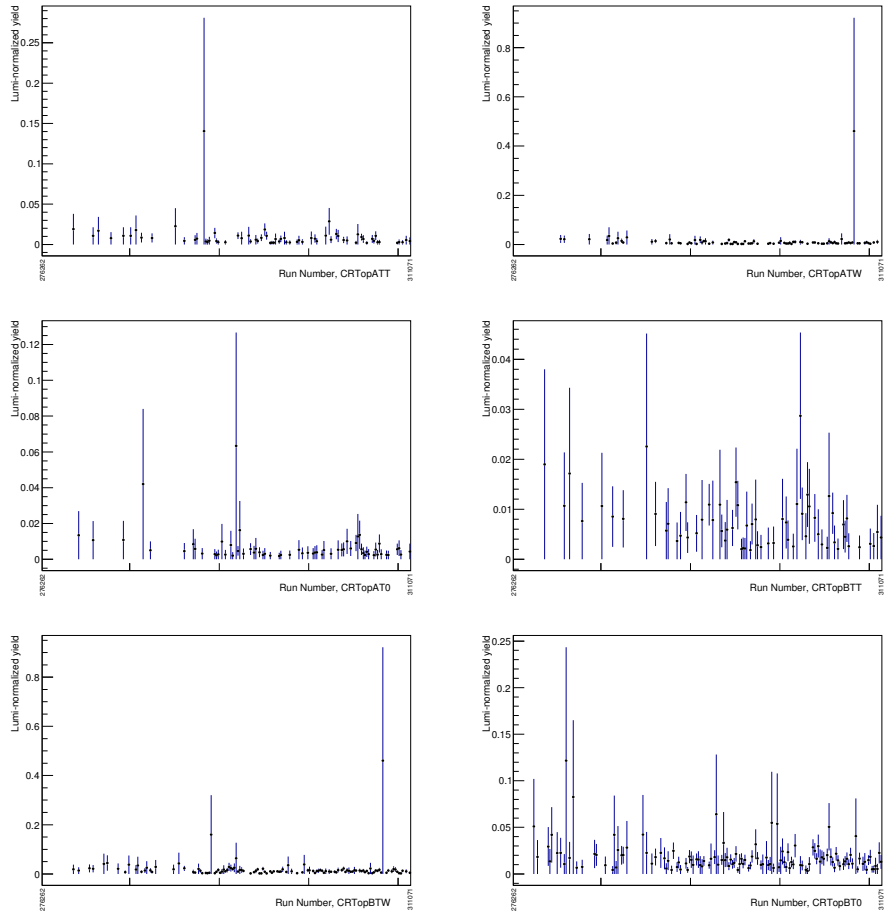


FIGURE A.2. Lumi-normalized distribution of run numbers in 2015 and 2016 in  $t\bar{t}$  control regions.

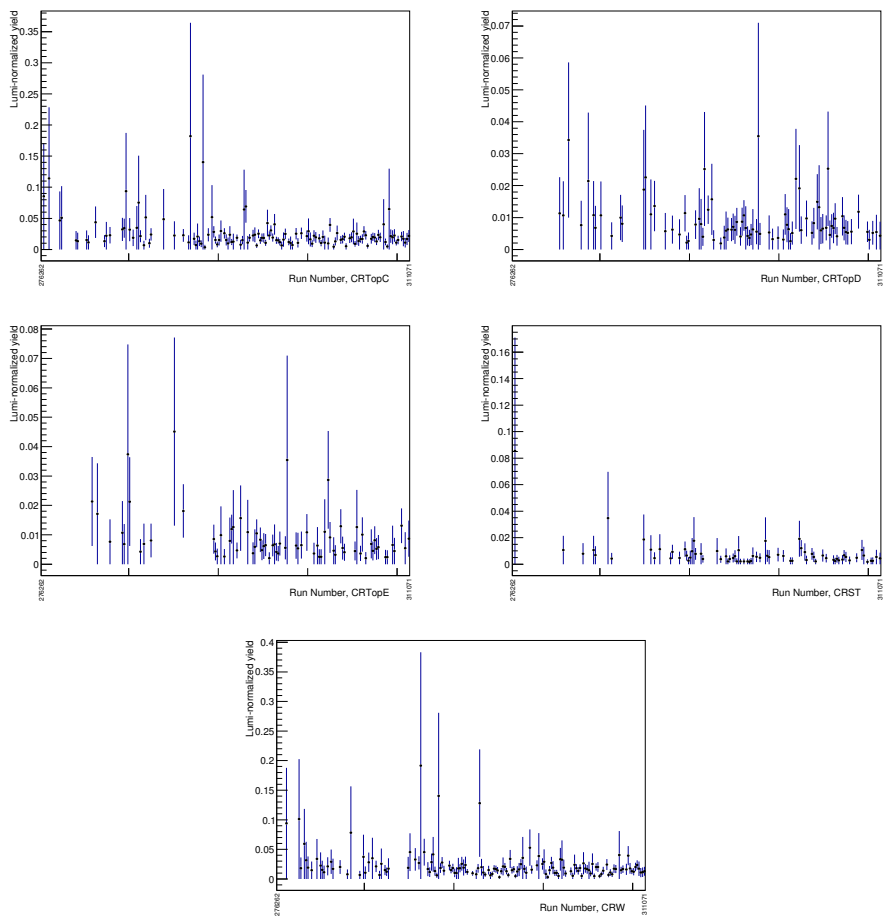


FIGURE A.3. Lumi-normalized distribution of run numbers in 2015 and 2016 in  $t\bar{t}$  control regions.

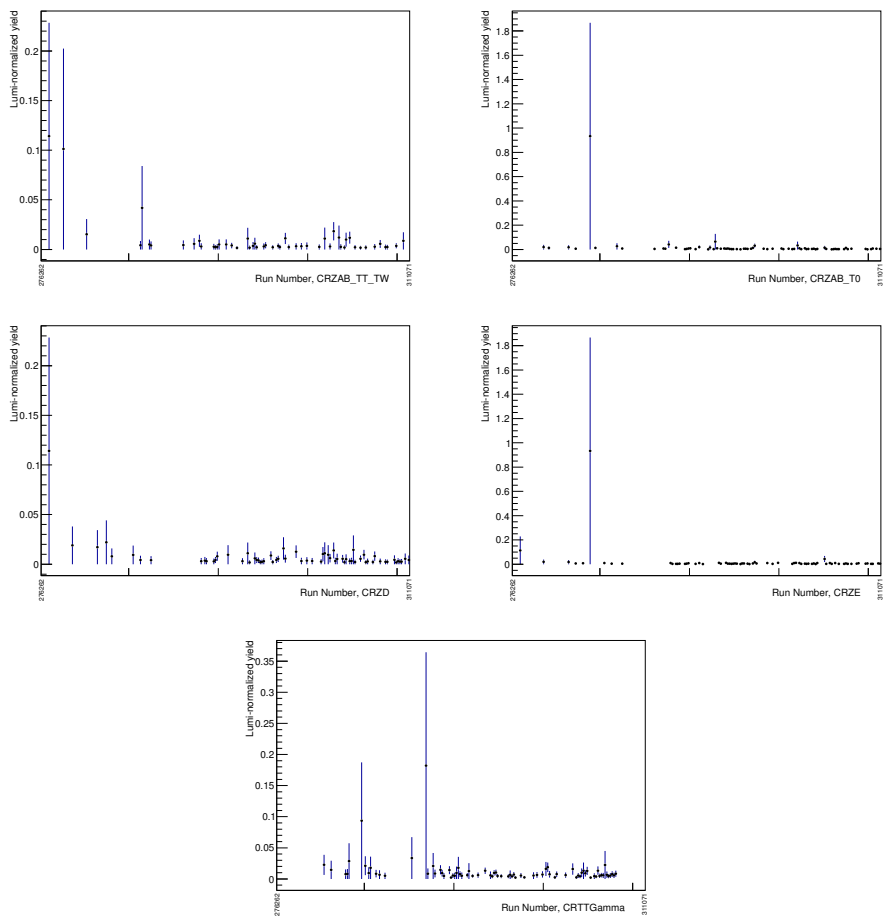


FIGURE A.4. Lumi-normalized distribution of run numbers in 2015 and 2016 in  $Z$  and  $t\bar{t} + \gamma$  control regions.

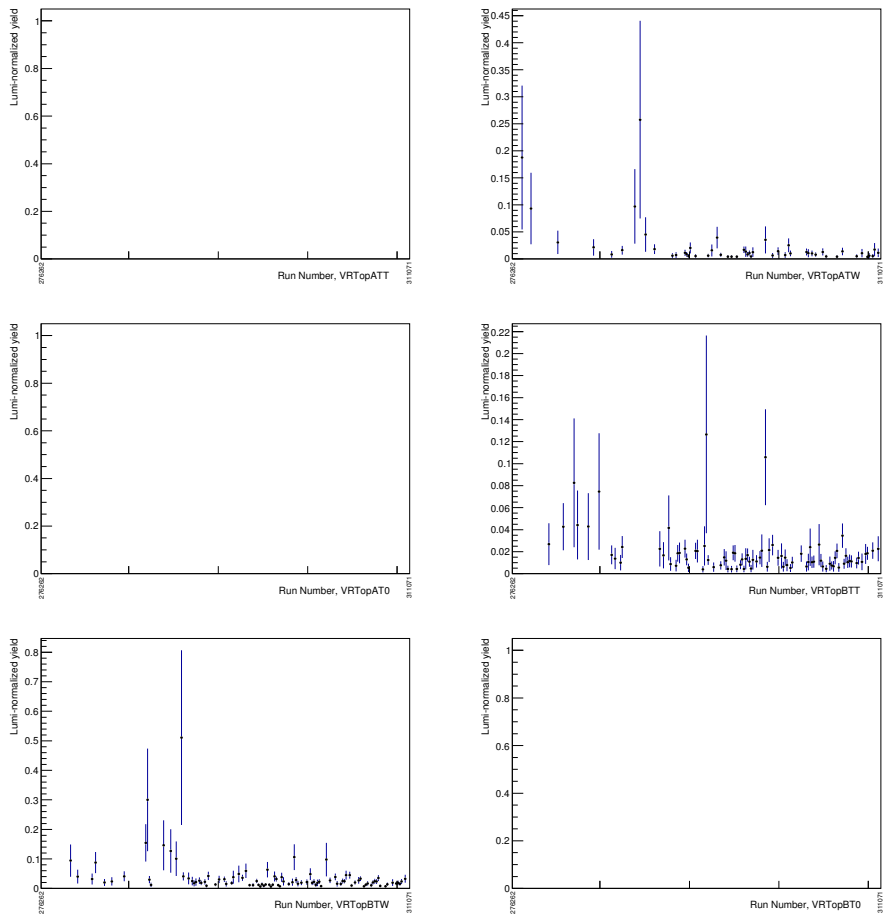


FIGURE A.5. Lumi-normalized distribution of run numbers in 2015 and 2016 in validation regions.

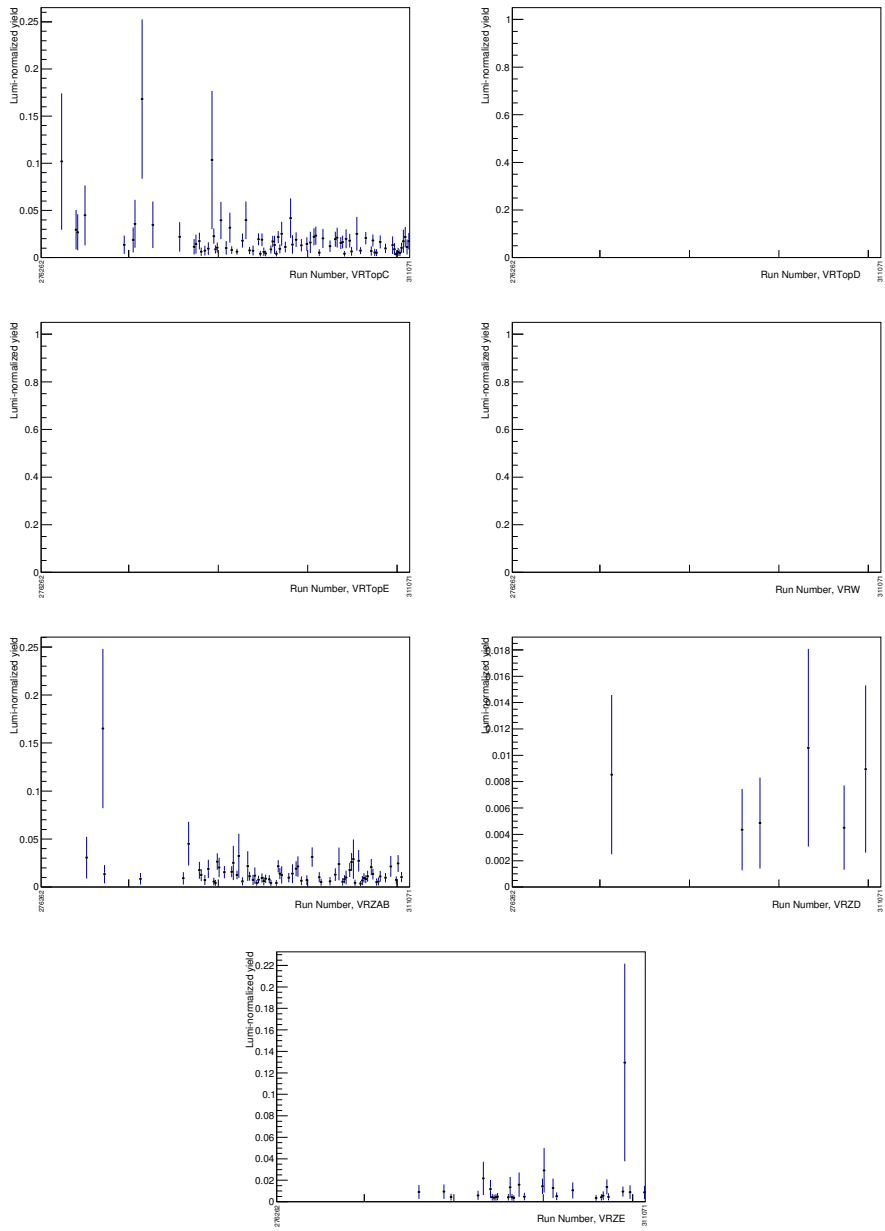


FIGURE A.6. Lumi-normalized distribution of run numbers in 2015 and 2016 in validation regions.

### A.0.3. n vtx distribution before and after pileup reweighting

The purpose of this check is to check the pileup reweighting. Ideally the Monte Carlo will match the data after reweighting. The preselection is the same as in Section 7.1.

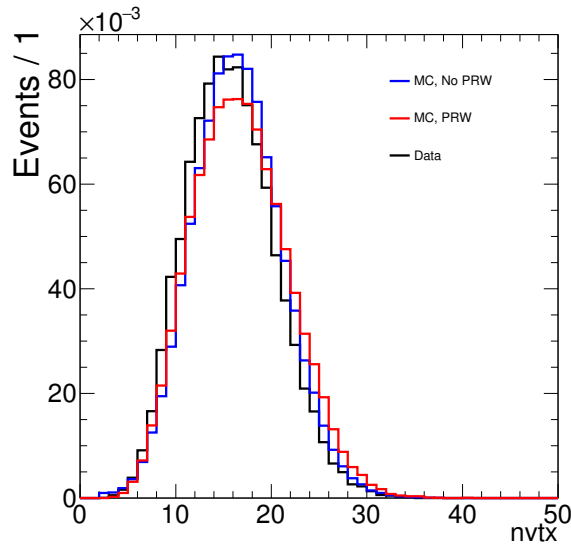


FIGURE A.7. Distribution of n vtx before reweighting (blue) and after reweighting (red) compared to data (black).

## APPENDIX B

### SIGNAL CONTAMINATION

The following section provides the signal contamination for control and validation regions.

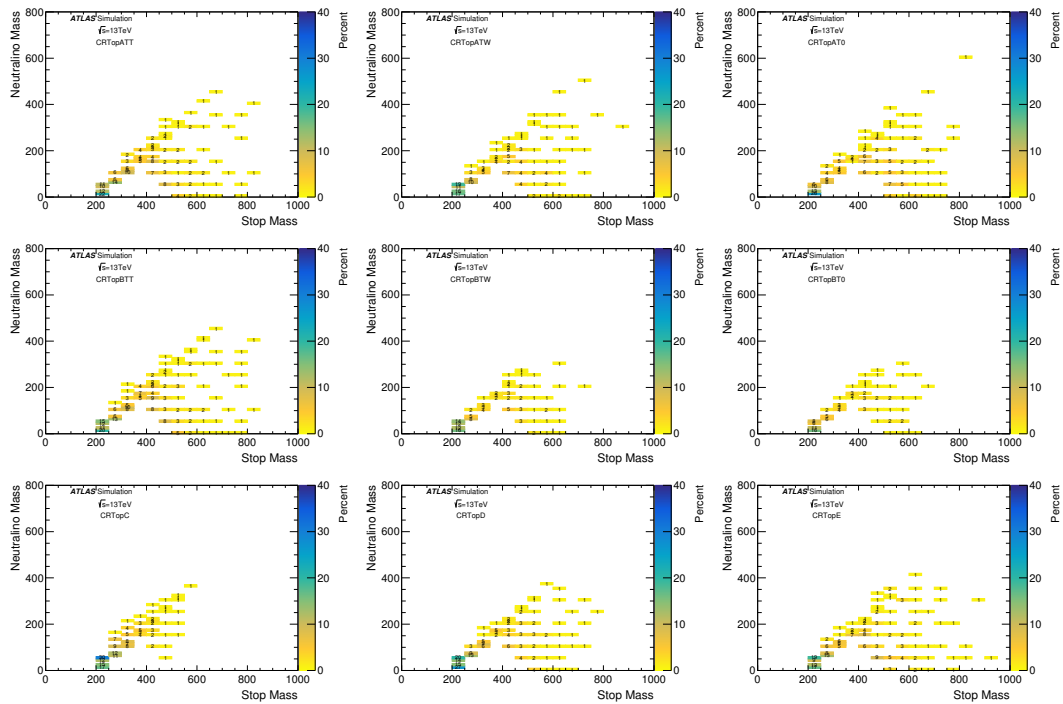


FIGURE B.1. Signal contamination for stop production as a function of stop and neutralino masses for CRTop.

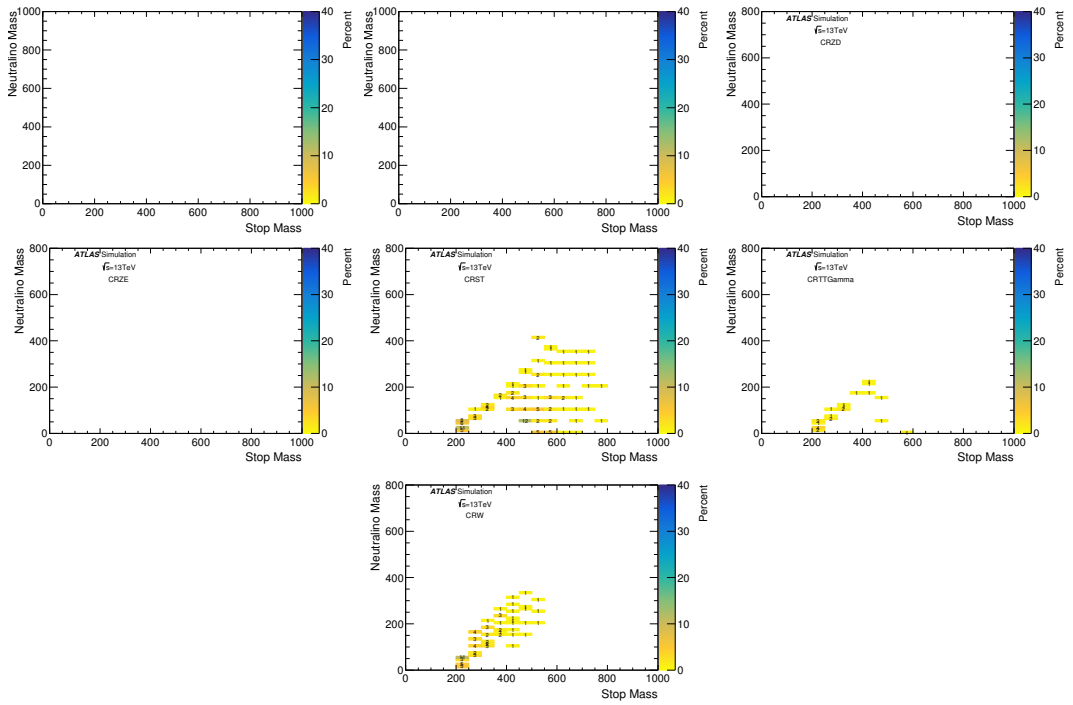


FIGURE B.2. Signal contamination for stop production as a function of stop and neutralino masses for CRZ, CRST, and CRW.

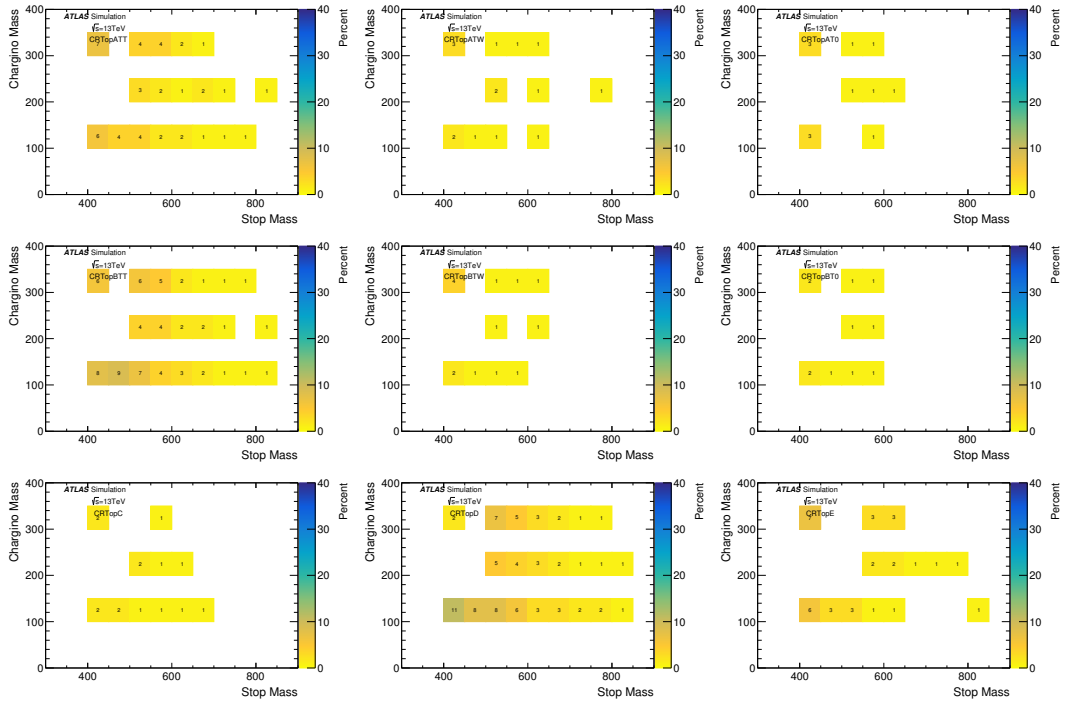


FIGURE B.3. Signal contamination for SRD for CRTop.

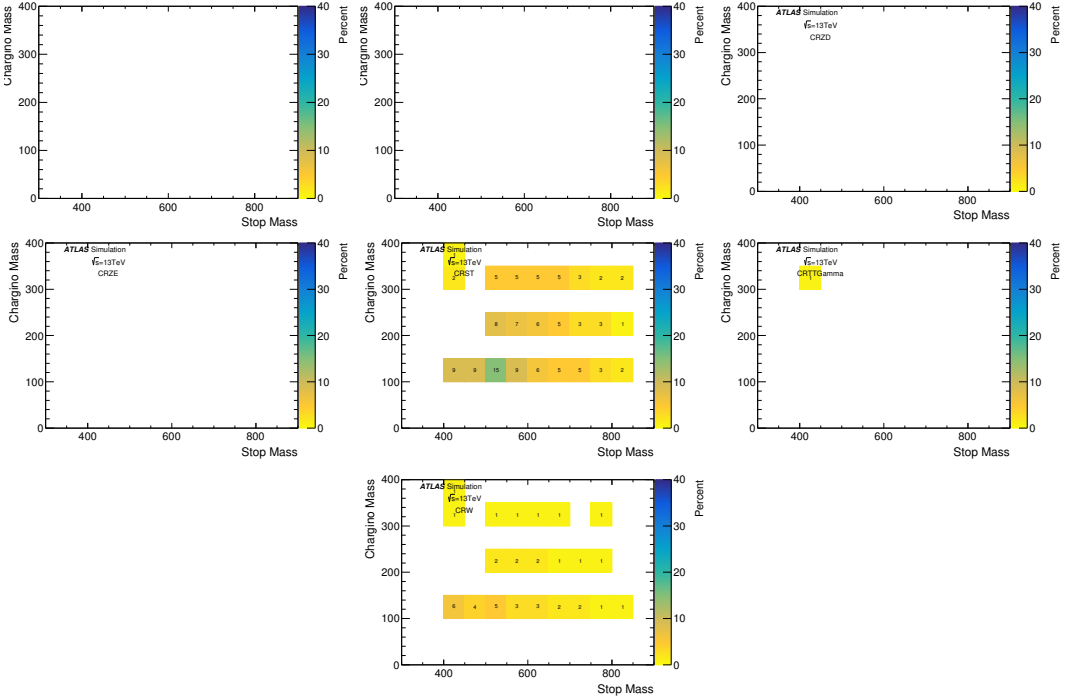


FIGURE B.4. Signal contamination for SRD for CRZ, CRST, and CRW.

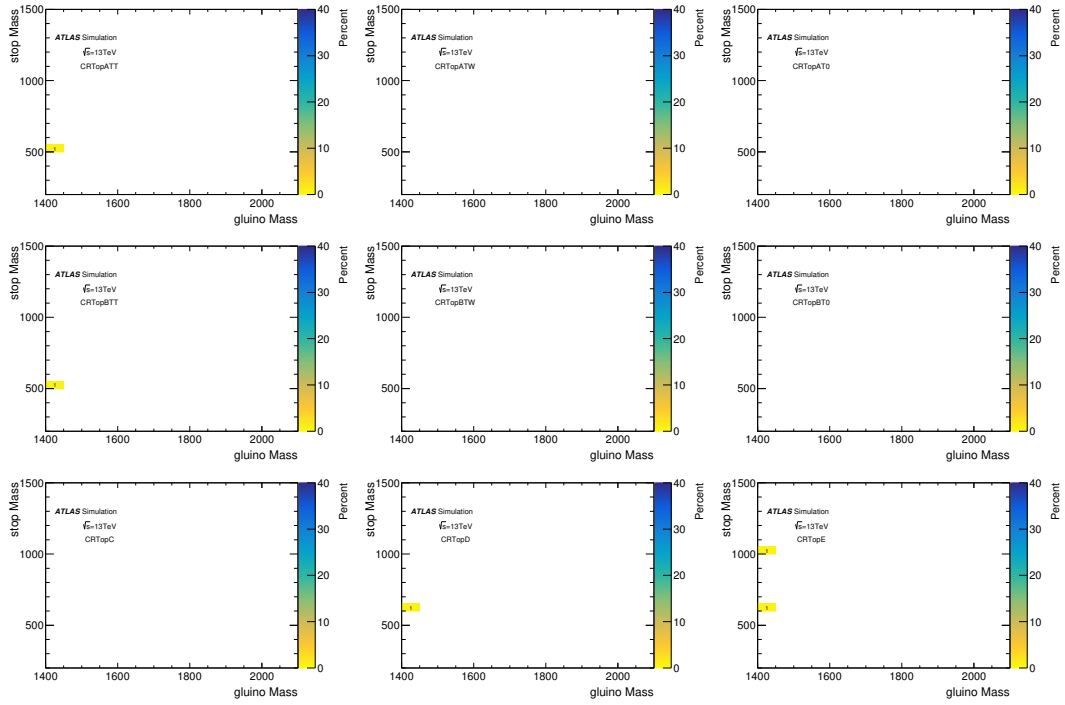


FIGURE B.5. Signal contamination for SRE for CRTop.

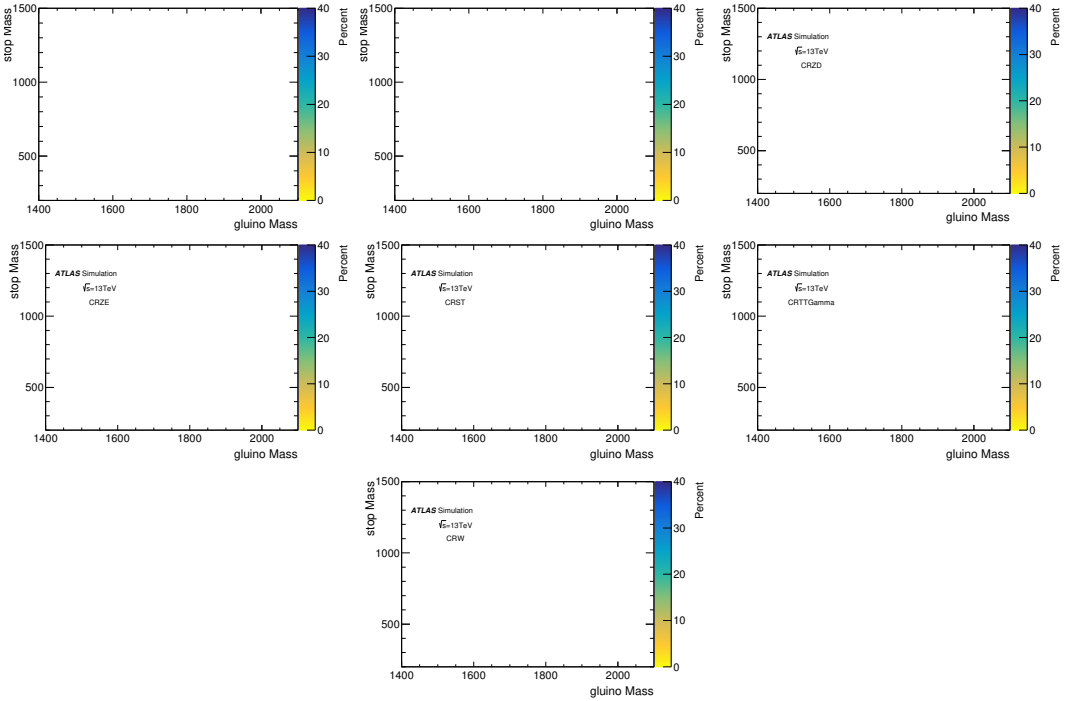


FIGURE B.6. Signal contamination for SRE for CRZ, CRST, and CRW.

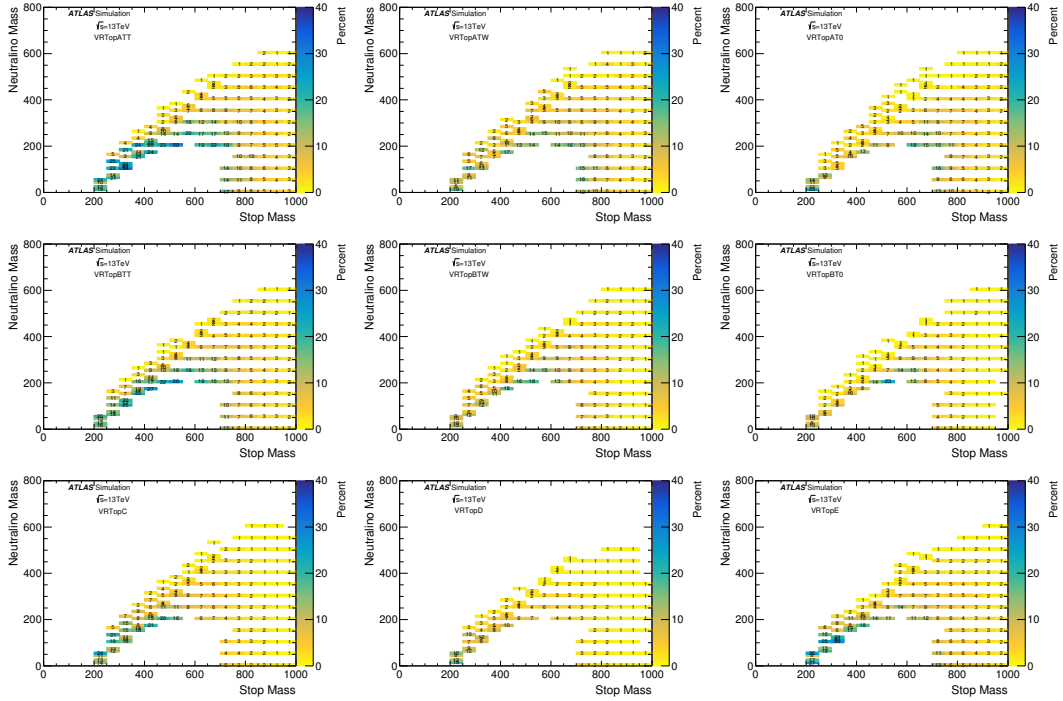


FIGURE B.7. Signal contamination for stop production as a function of stop and neutralino masses for VRTop.

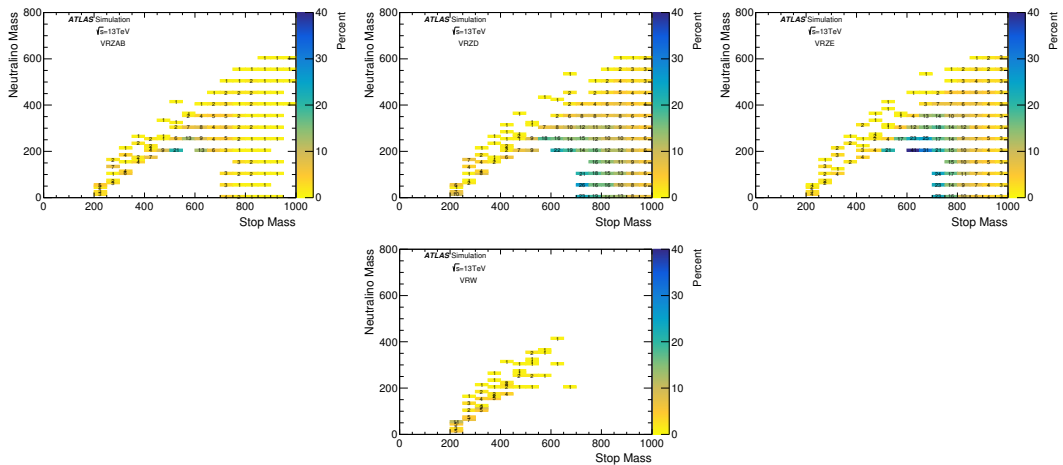


FIGURE B.8. Signal contamination for stop production as a function of stop and neutralino masses for VRZ, and VRW.

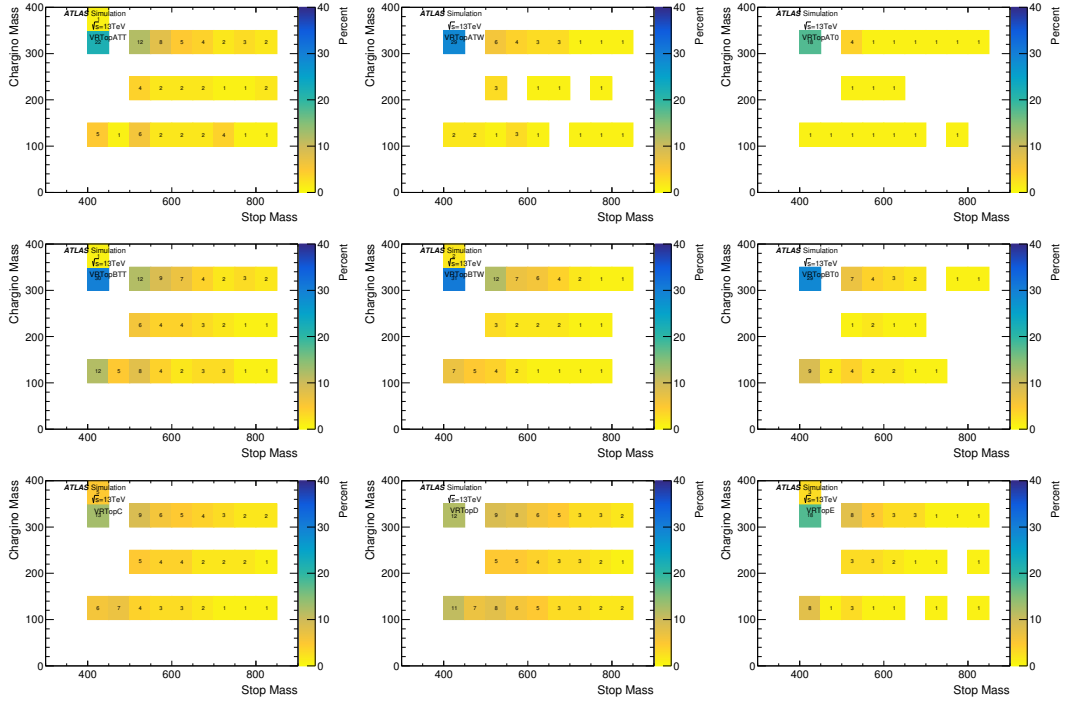


FIGURE B.9. Signal contamination for stop production as a function of stop and neutralino masses for VRTop.

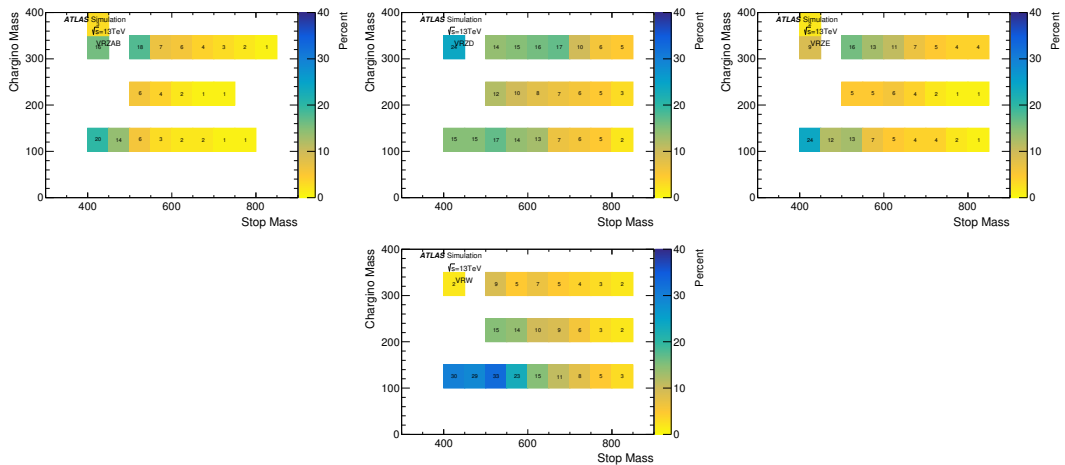


FIGURE B.10. Signal contamination for stop production as a function of stop and neutralino masses for VRZ, and VRW.

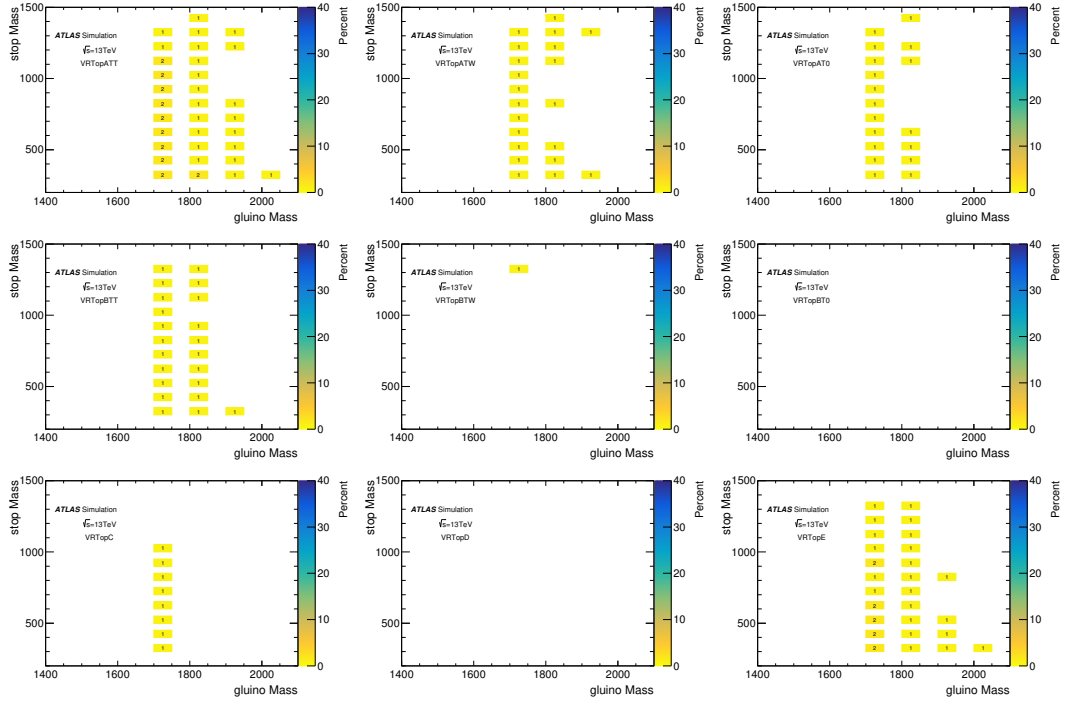


FIGURE B.11. Signal contamination for stop production as a function of stop and neutralino masses for VRTop.

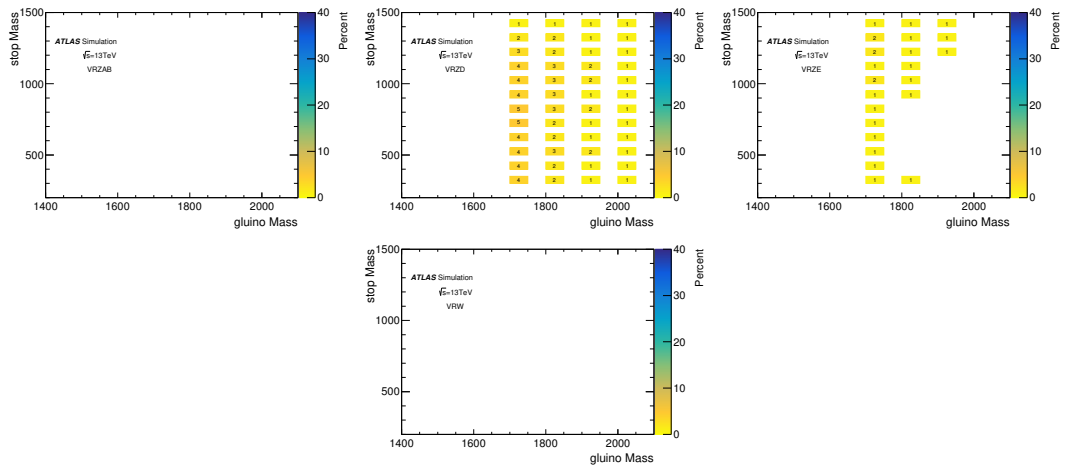


FIGURE B.12. Signal contamination for stop production as a function of stop and neutralino masses for VRZ, and VRW.

## REFERENCES CITED

- [1] ATLAS Collaboration. “Search for a scalar partner of the top quark in the jets plus missing transverse momentum final state at  $\sqrt{s}=13$  TeV with the ATLAS detector”. In: *JHEP* (2017), p. 57. DOI: 10.1007/JHEP12(2017)085. arXiv: 1709.04183 [hep-ex].
- [2] K. A. Olive et al. “Review of Particle Physics”. In: *Chin. Phys. C* 38 (2014), p. 090001. DOI: 10.1088/1674-1137/38/9/090001.
- [3] D0 Collaboration. “Observation of the Top Quark”. In: *Physic Review Letters* 74 (1995). DOI: 10.1103/PhysRevLett.74.2632. arXiv: 9503003 [hep-ex].
- [4] *Top quark decays*. <http://www.quantumdiaries.org/tag/top-quark/>. Accessed: 2018-04-15.
- [5] The ATLAS Collaboration. “Observation of a new particle in the search for the Standard Model Higgs boson with the ATLAS detector at the LHC”. In: *Phys. Lett. B* 716 (2012), pp. 1–29. DOI: 10.1016/j.physletb.2012.08.020. arXiv: 1207.7214 [hep-ex].
- [6] CMS Collaboration. “Observation of a new boson at a mass of 125 GeV with the CMS experiment at the LHC”. In: *Phys. Lett. B* 716 (2012), p. 30. DOI: 10.1016/j.physletb.2012.08.021. arXiv: 1207.7235 [hep-ex].
- [7] Super-Kamiokande Collaboration. “Evidence for oscillation of atmospheric neutrinos”. In: *Physical Review Letters* 81 (1998). DOI: 10.1103/PhysRevLett.81.1562. arXiv: hep-ex/9807003.
- [8] Planck collaboration. “Planck 2015 results. I. Overview of products and scientific results”. In: (2015). arXiv: 1502.01582 [astro-ph.CO].
- [9] J.C. Kapteyn. “First Attempt at a Theory of the Arrangement and Motion of the Sidereal System”. In: *Astrophysical Journal* 55 (1922), p. 302. DOI: 10.1086/142670.
- [10] F.Zwicky. “Die Rotverschiebung von extragalaktischen Nebeln”. In: *Helvetica Physica Acta* 6 (1933), p. 110.
- [11] H.Babcock. “The rotation of the Andromeda Nebula”. In: *Lick Observatory bulletin* 498 (1939).
- [12] N. Ford V. Rubin W.K. Thonnard. “Rotational Properties of 21 Sc Galaxies with a Large Range of Luminosities and Radii from NGC 4605 ( $R = 4\text{kpc}$ ) to UGC 2885 ( $R = 122\text{kpc}$ )”. In: *The Astrophysical Journal* 238 (1980). DOI: 10.1086/158003.
- [13] Douglas Clowe et al. “A direct empirical proof of the existence of dark matter”. In: *Astrophys. J.* 648 (2006). DOI: 10.1086/508162. arXiv: 0608407 [astro-ph].

- [14] D. I. Kazakov. “Beyond the standard model: In search of supersymmetry”. In: *2000 European School of high-energy physics, Caramulo, Portugal, 20 Aug-2 Sep 2000: Proceedings*. 2000, pp. 125–199. arXiv: hep-ph/0012288 [hep-ph]. URL: <http://alice.cern.ch/format/showfull?sysnb=2235897>.
- [15] Christoph Borschensky et al. “Squark and gluino production cross sections in pp collisions at  $\sqrt{s} = 13, 14, 33$  and  $100$  TeV”. In: *Eur. Phys. J.* C74.12 (2014), p. 3174. DOI: 10.1140/epjc/s10052-014-3174-y. arXiv: 1407.5066 [hep-ph].
- [16] Yu. A. Golfand and E. P. Likhtman. “Extension of the Algebra of Poincare Group Generators and Violation of p Invariance”. In: *JETP Lett.* 13 (1971). [*Pisma Zh. Eksp. Teor. Fiz.* 13,452(1971)], pp. 323–326.
- [17] D. V. Volkov and V. P. Akulov. “Is the Neutrino a Goldstone Particle?” In: *Phys. Lett. B* 46 (1973), pp. 109–110. DOI: 10.1016/0370-2693(73)90490-5.
- [18] J. Wess and B. Zumino. “Supergauge Transformations in Four-Dimensions”. In: *Nucl. Phys. B* 70 (1974), pp. 39–50. DOI: 10.1016/0550-3213(74)90355-1.
- [19] Abdus Salam and J. A. Strathdee. “Supersymmetry and Nonabelian Gauges”. In: *Phys. Lett. B* 51 (1974), pp. 353–355. DOI: 10.1016/0370-2693(74)90226-3.
- [20] Super-Kamiokande Collaboration. “Search for Proton Decay into Muon plus Neutral Kaon in Super-Kamiokande I, II, and III”. In: *Phys. Rev. D* 86 (2012). DOI: 10.1103/PhysRevD.86.012006. arXiv: 1205.6538.
- [21] Glennys R. Farrar and Pierre Fayet. “Phenomenology of the production, decay, and detection of new hadronic states associated with supersymmetry”. In: *Physics Letters B* 76.5 (1978), pp. 575–579. ISSN: 0370-2693. DOI: [http://dx.doi.org/10.1016/0370-2693\(78\)90858-4](http://dx.doi.org/10.1016/0370-2693(78)90858-4). URL: <http://www.sciencedirect.com/science/article/pii/0370269378908584>.
- [22] John Ellis et al. “Supersymmetric relics from the big bang”. In: *Nuclear Physics B* 238.2 (1984), pp. 453–476. ISSN: 0550-3213. DOI: [http://dx.doi.org/10.1016/0550-3213\(84\)90461-9](http://dx.doi.org/10.1016/0550-3213(84)90461-9). URL: <http://www.sciencedirect.com/science/article/pii/0550321384904619>.
- [23] Stephen P. Martin. “A Supersymmetry primer: Version 7”. In: (2016). [*Adv. Ser. Direct. High Energy Phys.* 18,1(1998)]. DOI: 10.1142/9789812839657\_0001, 10.1142/9789814307505\_0001. arXiv: hep-ph/9709356 [hep-ph].
- [24] A. Djouadi et al. “The Minimal supersymmetric standard model: Group summary report”. In: (1998). arXiv: hep-ph/9901246 [hep-ph]. URL: [https://inspirehep.net/record/481987/files/arXiv:hep-ph\\_9901246.pdf](https://inspirehep.net/record/481987/files/arXiv:hep-ph_9901246.pdf).
- [25] A. Djouadi et al. “The Minimal supersymmetric standard model: Group summary report”. In: (1998). arXiv: hep-ph/9901246 [hep-ph].

- [26] Thomas G. Rizzo. “The Zoo of BSM Physics at the LHC”. In: *The 40th SLAC Summer Institute*. Aug. 2012.
- [27] Lyndon Evans and Philip Bryant. “LHC Machine”. In: *JINST* 3 (2008). Ed. by Lyndon Evans, S08001. doi: 10.1088/1748-0221/3/08/S08001.
- [28] “The ATLAS Experiment at the CERN Large Hadron Collider”. In: *JINST* 3 (2008), S08003. doi: 10.1088/1748-0221/3/08/S08003.
- [29] ATLAS Collaboration. “ATLAS Insertable B-Layer Technical Design Report”. In: CERN-LHCC-2010-013. ATLAS-TDR-19 (Sept. 2010). URL: <https://cds.cern.ch/record/1291633>.
- [30] ATLAS Collaboration. “ATLAS Liquid Argon Calorimeter Technical Design Report”. In: CERN-LHCC-96-041. ATLAS-TDR-2 (1996). URL: [cds.cern.ch/record/331061](https://cds.cern.ch/record/331061).
- [31] ATLAS Collaboration. “Performance of the ATLAS Liquid Argon Calorimeter after three years of LHC operation and plans for a future upgrade”. In: (Sept. 2014). URL: <http://iopscience.iop.org/article/10.1088/1748-0221/9/09/C09007/pdf>.
- [32] The ATLAS collaboration. “Electron efficiency measurements with the ATLAS detector using the 2015 LHC proton-proton collision data”. In: (2016).
- [33] ATLAS Collaboration. “ATLAS Liquid Argon Calorimeter Phase-I Upgrade Technical Design Report”. In: CERN-LHCC-2013-017. ATLAS-TDR-022 (2013). URL: [cds.cern.ch/record/1602230](https://cds.cern.ch/record/1602230).
- [34] ATLAS Collaboration. “ATLAS TDAQ Phase-I Upgrade gFEX Final Design Report”. In: ATL-COM-DAQ-2016-184 (Nov. 2016). URL: [cds.cern.ch/record/2233958](https://cds.cern.ch/record/2233958).
- [35] ATLAS Collaboration. *ATLAS Trigger and Data Acquisition Phase-II Upgrade Technical Design Report*. Tech. rep. ATL-COM-DAQ-2017-185. This version represents the draft for EB approval and LHCC release. Geneva: CERN, Dec. 2017. URL: <https://cds.cern.ch/record/2296879>.
- [36] The ATLAS Collaboration. *ATLAS Liquid Argon Calorimeter Phase-II Upgrade Technical Design Report*. Tech. rep. ATL-COM-LARG-2017-030. Geneva: CERN, Aug. 2017. URL: <https://cds.cern.ch/record/2280232>.
- [37] The ATLAS Collaboration. “Measurement of the  $t\bar{t}W$  and  $t\bar{t}Z$  production cross sections in  $pp$  collisions at  $\sqrt{s} = 8$  TeV with the ATLAS detector”. In: *Journal of High Energy Physics* 2015.11 (Nov. 2015), p. 172. ISSN: 1029-8479. doi: 10.1007/JHEP11(2015)172. URL: [https://doi.org/10.1007/JHEP11\(2015\)172](https://doi.org/10.1007/JHEP11(2015)172).
- [38] ATLAS Collaboration. “Search for top-squark pair production in final states with one lepton, jets, and missing transverse momentum using  $36\text{ fb}^{-1}$  of  $\sqrt{s}=13$  TeV pp collision data with the ATLAS detector”. In: *JHEP* (2017), p. 95. arXiv: 1711.11520 [hep-ex].

- [39] ATLAS Collaboration. “Search for direct top squark pair production in final states with two leptons in  $\sqrt{s}=13$  TeV pp collisions with the ATLAS detector”. In: *Eur. Phys. J.* (2017), p. 47. DOI: 10.1140/epjc/s10052-017-5445-x. arXiv: 1708.03247 [hep-ex].
- [40] ATLAS Collaboration. “Search for direct pair production of the top squark in all-hadronic final states in proton-proton collisions at  $\sqrt{s}=8$  TeV with the ATLAS detector”. In: *JHEP* (2014), p. 34. DOI: 10.1007/JHEP09(2014)015. arXiv: 1406.1122 [hep-ex].
- [41] ATLAS Collaboration. *Summary plots from the ATLAS Standard Model physics group*. Aug. 2016. URL: [https://atlas.web.cern.ch/Atlas/GROUPS/PHYSICS/CombinedSummaryPlots/SM/index.html#ATLAS\\_b\\_SMSummary\\_FiducialXsect](https://atlas.web.cern.ch/Atlas/GROUPS/PHYSICS/CombinedSummaryPlots/SM/index.html#ATLAS_b_SMSummary_FiducialXsect).
- [42] ATLAS Collaboration. “Search for squarks and gluinos with the ATLAS detector in final states with jets and missing transverse momentum using 4.7  $\text{fb}^{-1}$  of  $\sqrt{s} = 7$  TeV proton-proton collision data”. In: *Phys. Rev.* D87.1 (2013), p. 012008. DOI: 10.1103/PhysRevD.87.012008. arXiv: 1208.0949 [hep-ex].
- [43] Glen Cowan et al. “Asymptotic formulae for likelihood-based tests of new physics”. In: *Eur. Phys. J.* C71 (2011). [Erratum: Eur. Phys. J.C73,2501(2013)], p. 1554. DOI: 10.1140/epjc/s10052-011-1554-0, 10.1140/epjc/s10052-013-2501-z. arXiv: 1007.1727 [physics.data-an].
- [44] M. Baak et al. “HistFitter software framework for statistical data analysis”. In: *Eur. Phys. J.* C75 (2015), p. 153. DOI: 10.1140/epjc/s10052-015-3327-7. arXiv: 1410.1280 [hep-ex].
- [45] Thomas Junk. “Confidence level computation for combining searches with small statistics”. In: *Nucl. Instrum. Meth.* A434 (1999), pp. 435–443. DOI: 10.1016/S0168-9002(99)00498-2. arXiv: hep-ex/9902006 [hep-ex].
- [46] Alexander L. Read. “Presentation of search results: the  $CL_s$  technique”. In: *J. Phys. G* 28 (2002), pp. 2693–2704. DOI: 10.1088/0954-3899/28/10/313.
- [47] ATLAS Collaboration. “ATLAS Run 1 searches for direct pair production of third-generation squarks at the Large Hadron Collider”. In: *Eur. Phys. J.* C75.10 (2015). [Erratum: Eur. Phys. J.C76,no.3,153(2016)], p. 510. DOI: 10.1140/epjc/s10052-015-3726-9, 10.1140/epjc/s10052-016-3935-x. arXiv: 1506.08616 [hep-ex].
- [48] ATLAS collaboration. *The Optimization of ATLAS Track Reconstruction in Dense Environments*. Tech. rep. ATL-PHYS-PUB-2015-006. Geneva: CERN, Mar. 2015. URL: <https://cds.cern.ch/record/2002609>.
- [49] ATLAS Collaboration. *Jet Calibration and Systematic Uncertainties for Jets Reconstructed in the ATLAS Detector at  $\sqrt{s} = 13$  TeV*. ATL-PHYS-PUB-2015-015. 2015. URL: <https://cds.cern.ch/record/2037613>.

- [50] W Lampl et al. *Calorimeter Clustering Algorithms: Description and Performance*. Tech. rep. ATL-LARG-PUB-2008-002. ATL-COM-LARG-2008-003. Geneva: CERN, Apr. 2008. URL: <https://cds.cern.ch/record/1099735>.
- [51] Bora Isildak. “Measurement of the differential dijet production cross section in proton-proton collisions at  $\sqrt{s} = 7$  tev”. PhD thesis. Bogazici U., 2011. arXiv: 1308.6064 [hep-ex]. URL: <http://inspirehep.net/record/1251416/files/arXiv:1308.6064.pdf>.
- [52] Matteo Cacciari, Gavin P. Salam, and Gregory Soyez. “The anti- $k_t$  jet clustering algorithm”. In: *JHEP* 04 (2008), p. 063. DOI: 10.1088/1126-6708/2008/04/063. arXiv: 0802.1189 [hep-ph].
- [53] M. Aaboud et al. “Jet energy scale measurements and their systematic uncertainties in proton-proton collisions at  $\sqrt{s} = 13$  TeV with the ATLAS detector”. In: *Phys. Rev.* D96.7 (2017), p. 072002. DOI: 10.1103/PhysRevD.96.072002. arXiv: 1703.09665 [hep-ex].
- [54] ATLAS Collaboration. *Selection of jets produced in 13TeV proton-proton collisions with the ATLAS detector*. ATLAS-CONF-2015-029. 2015. URL: <https://cds.cern.ch/record/2037702>.
- [55] ATLAS Collaboration. *Commissioning of the ATLAS b-tagging algorithms using  $t\bar{t}$  events in early Run-2 data*. ATL-PHYS-PUB-2015-039. 2015. URL: <https://cds.cern.ch/record/2047871>.
- [56] ATLAS collaboration. *Electron efficiency measurements with the ATLAS detector using the 2015 LHC proton-proton collision data*. Tech. rep. ATLAS-CONF-2016-024. Geneva: CERN, June 2016. URL: <http://cds.cern.ch/record/2157687>.
- [57] ATLAS Collaboration. *Photon identification in 2015 ATLAS data*. Tech. rep. ATL-PHYS-PUB-2016-014. Geneva: CERN, Aug. 2016. URL: <http://cds.cern.ch/record/2203125>.
- [58] ATLAS Collaboration. “Muon reconstruction performance of the ATLAS detector in proton–proton collision data at  $\sqrt{s} = 13$  TeV”. In: *Eur. Phys. J.* C76.5 (2016), p. 292. DOI: 10.1140/epjc/s10052-016-4120-y. arXiv: 1603.05598 [hep-ex].
- [59] ATLAS Collaboration. *Expected performance of missing transverse momentum reconstruction for the ATLAS detector at  $\sqrt{s} = 13$  TeV*. Tech. rep. ATL-PHYS-PUB-2015-023. Geneva: CERN, July 2015. URL: <http://cds.cern.ch/record/2037700>.
- [60] T. Gleisberg et al. “Event generation with SHERPA 1.1”. In: *JHEP* 02 (2009), p. 007. DOI: 10.1088/1126-6708/2009/02/007. arXiv: 0811.4622 [hep-ph].

- [61] Torbjorn Sjostrand, Stephen Mrenna, and Peter Z. Skands. “A brief introduction to PYTHIA 8.1”. In: *Comput. Phys. Commun.* 178 (2008), pp. 852–867. DOI: [10.1016/j.cpc.2008.01.036](https://doi.org/10.1016/j.cpc.2008.01.036). arXiv: 0710.3820 [hep-ph].
- [62] Simone Alioli et al. “A general framework for implementing NLO calculations in shower Monte Carlo programs: the POWHEG BOX”. In: *JHEP* 06 (2010), p. 043. DOI: [10.1007/JHEP06\(2010\)043](https://doi.org/10.1007/JHEP06(2010)043). arXiv: 1002.2581 [hep-ph].
- [63] J. Alwall et al. “The automated computation of tree-level and next-to-leading order differential cross sections, and their matching to parton shower simulations”. In: *JHEP* 07 (2014), p. 079. DOI: [10.1007/JHEP07\(2014\)079](https://doi.org/10.1007/JHEP07(2014)079). arXiv: 1405.0301 [hep-ph].
- [64] David J. Lange. “The EvtGen particle decay simulation package”. In: *Nucl. Instrum. Meth.* 462.1-2 (2001), pp. 152–155. DOI: [http://dx.doi.org/10.1016/S0168-9002\(01\)00089-4](http://dx.doi.org/10.1016/S0168-9002(01)00089-4).
- [65] S. Agostinelli et al. “GEANT4—a simulation toolkit”. In: *Nucl. Instrum. Meth.* A506 (2003), pp. 250–303. DOI: [10.1016/S0168-9002\(03\)01368-8](https://doi.org/10.1016/S0168-9002(03)01368-8).
- [66] Nazar Bartosik. *Event simulation in HEP experiments*. July 2016. URL: [http://bartosik.pp.ua/hep\\_sketches/event\\_simulation](http://bartosik.pp.ua/hep_sketches/event_simulation).
- [67] C.G. Lester and D.J. Summers. “Measuring masses of semiinvisibly decaying particles pair produced at hadron colliders”. In: *Phys. Lett.* B463 (1999), pp. 99–103. DOI: [10.1016/S0370-2693\(99\)00945-4](https://doi.org/10.1016/S0370-2693(99)00945-4). arXiv: hep-ph/9906349.
- [68] Alan Barr, Christopher Lester, and P. Stephens. “A variable for measuring masses at hadron colliders when missing energy is expected;  $m_{T2}$ : the truth behind the glamour”. In: *J. Phys.* G29 (2003), pp. 2343–2363. DOI: [10.1088/0954-3899/29/10/304](https://doi.org/10.1088/0954-3899/29/10/304). arXiv: hep-ph/0304226 [hep-ph].
- [69] Paul Jackson, Christopher Rogan, and Marco Santoni. “Sparticles in motion: Analyzing compressed SUSY scenarios with a new method of event reconstruction”. In: *Phys. Rev.* D95.3 (2017), p. 035031. DOI: [10.1103/PhysRevD.95.035031](https://doi.org/10.1103/PhysRevD.95.035031). arXiv: 1607.08307 [hep-ph].
- [70] ATLAS Collaboration. “Search for top squarks in final states with one isolated lepton, jets, and missing transverse momentum in  $\sqrt{s} = 13$  TeV  $pp$  collisions with the ATLAS detector”. In: *Phys. Rev.* D94.5 (2016), p. 052009. DOI: [10.1103/PhysRevD.94.052009](https://doi.org/10.1103/PhysRevD.94.052009). arXiv: 1606.03903 [hep-ex].
- [71] ATLAS Collaboration. “Search for squarks and gluinos in events with isolated leptons, jets and missing transverse momentum at  $\sqrt{s} = 8$  TeV with the ATLAS detector”. In: *JHEP* 04 (2015), p. 116. DOI: [10.1007/JHEP04\(2015\)116](https://doi.org/10.1007/JHEP04(2015)116). arXiv: 1501.03555 [hep-ex].

- [72] ATLAS Collaboration. “Search for new phenomena in final states with an energetic jet and large missing transverse momentum in  $pp$  collisions at  $\sqrt{s} = 13$  TeV using the ATLAS detector”. In: *Phys. Rev.* D94.3 (2016), p. 032005. DOI: 10.1103/PhysRevD.94.032005. arXiv: 1604.07773 [hep-ex].
- [73] Michele Papucci, Joshua T. Ruderman, and Andreas Weiler. “Natural SUSY endures”. In: *JHEP* 09 (2012), p. 035. DOI: 10.1007/JHEP09(2012)035. arXiv: 1110.6926 [hep-ph].
- [74] ATLAS Collaboration. “Dark matter interpretations of ATLAS searches for the electroweak production of supersymmetric particles in  $\sqrt{s} = 8$  TeV proton-proton collisions”. In: *JHEP* 09 (2016), p. 175. DOI: 10.1007/JHEP09(2016)175. arXiv: 1608.00872 [hep-ex].
- [75] N. Arkani-Hamed, A. Delgado, and G. F. Giudice. “The Well-tempered neutralino”. In: *Nucl. Phys.* B741 (2006), pp. 108–130. DOI: 10.1016/j.nuclphysb.2006.02.010. arXiv: hep-ph/0601041 [hep-ph].
- [76] Plank Collaboration. “Planck 2013 results. XVI. Cosmological parameters”. In: *Astron. Astrophys.* 571 (2014), A16. DOI: 10.1051/0004-6361/201321591. arXiv: 1303.5076 [astro-ph.CO].